UNIVERSITY OF CALIFORNIA, SAN DIEGO

Experimental and Computational Studies of the Combustion of Classical and Alternative Fuels

A dissertation submitted in partial satisfaction of the
requirements for the degree
Doctor of Philosophy

in

Engineering Sciences (Mechanical Engineering)

by

Ulrich Niemann

Committee in charge:

Professor Kalyanasundaram Seshadri, Chair
Professor Forman A. Williams, Co-Chair
Professor Robert J. Cattolica
Professor Richard K. Herz
Professor Marc A. Meyers

2013

The dissertation of Ulrich Niemann is approved, and it is acceptable in quality and form for publication on microfilm and electronically:

_____

_____

_____

_____
Co-Chair

_____
Chair

University of California, San Diego

2013

DEDICATION

To my sister and my parents

EPIGRAPH

Sapere aude!

"Berlinische Monatsschrift 4 (1784)"
by Immanuel Kant

TABLE OF CONTENTS

NOMENCLATURE

Symbols

a	strain rate (s^{-1})
A	pre-exponential factor
c_p	specific heat (J/kg/K)
D	diffusivity coefficient
E	activation energy
k	reaction rate
l	length (mm)
L	length (mm)
Le	Lewis number (-)
p	pressure (MPa)
R	gas constant (J/mol/K)
T	temperature (K)
V	velocity (m/s)
W	molecular weight (g/mol)
X	mole fraction (-)
x	spatial coordinate
Y	mass fraction (-)
Z	mixture fraction (-)

Greek Symbols

μ	stoichiometric mass ratio
ν	stoichiometric mass ratio
ρ	density

Subscripts

1	fuel side
2	oxidizer side
ad	adiabatic
E	extinction
F	fuel
I	auto-ignition
O	oxidizer
st	stoichiometric

ACKNOWLEDGEMENTS

First and foremost, I would like to thank my sister for her selfless support throughout this turbulent journey. Our bond is what helped me to maintain my sanity and preserve my identity. Time and time again it was her unconditional faith in me and words of encouragement that strengthened my resolve to pursue my goals, fight relentlessly to avoid mediocrity, and believe in a bright future.

Words of utmost gratitude go to my parents, whose example instilled the values in me that made my humble accomplishments possible and will guide me throughout the future. I am deeply thankful for having been raised with the freedom to think, to reason, to question, and to dissent. Their confidence in me never led them to question my decisions nor utter a word of skepticism. Their support has been invaluable to this undertaking.

Above all, I am greatly indebted to my thesis adivsor, Kal Seshadri, who made this once-in-a-lifetime opportunity possible. Under his tutelage I was able to create my own little research world; an unusual blend of engineering and science which perfectly suited my aspirations. Even through rough times he stuck with me, allowing me to continue on my path. He has provided guidance at key moments while allowing me to take responsibility for my projects and work independently most of the time. The resources he provided for me over the years, not only kept my financial burden to a minimum, but also allowed for an extraordinarily interesting and exciting work place. I have truly appreciated the environment of casual and open interaction that stems from his calm and humble personality.

I also want to express my deep-felt gratitude to Forman Williams for his support, guidance and advice. The opportunity to work with someone with such a keen intellect, humility, patience, and kindeness has been inspiring and motivating. His always open office door, which is the perfect metaphor, was not only a beacon of hope for me, but usually the gateway to a fresh perspective. It is hard to imagine how many scientific problems I would not have solved, if it had not been for him pushing me in the right direction.

I am also grateful to the support that was given to me by Bob Cattolica, who has always been generously looking out for me, who included me in many of his interesting projects, and who always, despite his busy schedule, found time for many entertaining conversations.

My longest and closest friend Arno who despite living half way across the globe, I would like to thank for making our friendship a priority and for being so understanding when our valued weekend phone calls were cut short or canceled due to my workload.

Those who have helped me with my research or allowed a fruitful exchange of ideas also deserve credit for my accomplishments. Michael Gollner, Ryan Gehmlich, Kevin Mandich, Tei Newman-Lehman, Xinyan Huang, Priyank Saxena, and Reinhard Seiser have all significantly contributed to my work and became good friends. All of them have human qualities I truly admire and they all contributed enormously to my intellectual growth.

Chapter 2, in part, has been published in *Combustion Theory and Modelling* "Effect of addition of a nonequidiffusional reactant to an equidiffusional diffusion flame" by **Niemann, U.**, Seshadri, K., Wiliams, F. A., (in press). The thesis author is the primary investigator in this publication.

Section 3.1, in part, has been published in *Proceedings of the Combustion Institute* "Effect of pressure on structure and extinction of near-limit hydrogen counterflow diffusion flames" by **Niemann, U.**, Seshadri, K., Williams, F. A., Volume 34, Issue 1, 2012, pages 881-886. The thesis author is the primary investigator in this publication.

Section 3.2, in part, has been submitted for publication in *Combustion and Flame* "Methane, ethane, and ethylene laminar counterflow diffusion flames at elevated pressures: experimental and computational investigations up to 2.0 MPa" by **Niemann, U.**, Seshadri, K., Williams, F. A., (submitted for publication). The thesis author is the primary investigator in this publication.

Section 4.2, in part, has been published in *Combustion and Flame* "An experimental and kinetic modeling study of n-propanol and iso-propanol combustion", by A. Frassoldati, A. Cuoci, T. Faravelli, **Niemann, U.**, Ranzi, E., et al., Volume 157, Issue 1, 2010, Pages 2-16.

Section 4.3, in part, has been published in *Combustion and Flame* "An experimental and kinetic modeling study of combustion of isomers of butanol" by Grana, R., Frassoldati, A., Faravelli, T., **Niemann, U.**, Ranzi, E., et al., Volume 157, Issue 11, 2010, Pages 2137-2154

Chapter 5, in part, has been published in *Combustion Theory and Modelling* "Ignition and extinction of low molecular weight esters in nonpremixed flows" by **Niemann, U.**, Seiser, R., Seshadri, K. Volume 14, Issue 6, November 2010, pages 875-891, The thesis author is the primary investigator in this publication.

La Jolla, California. May 22, 2012.

2008	M. S. in Mechanical Engineering, University of Technology, Vienna
2013	Ph. D. in Engineering Sciences (Mechanical Engineering), University of California, San Diego

PUBLICATIONS

Niemann, U., Seshadri, K., Williams, F. A., Methane, ethane, and ethylene laminar counterflow diffusion flames at elevated pressures: experimental and computational investigations up to 2.0 MPa *Combustion and Flame* (submitted for publication)

Niemann, U., Seshadri, K., Wiliams, F. A., Effect of addition of a nonequidiffusional reactant to an equidiffusional diffusion flame *Combustion Theory and Modelling* (in press)

Sarathy,S.M., **Niemann, U.**, Yeung, C., Gehmlich, R., Westbrook, C.K., Plomer, M., Luo, Z., Mehl, M., Pitz, W.J., Seshadri, K., Thomson, M.J., Lu, T., A counterflow diffusion flame study of branched octane isomers, *Proceedings of the Combustion Institute* Volume 34, Issue 1, 2013, Pages 1015-1023

Niemann, U., Seshadri, K., Williams, F. A.,Effect of pressure on structure and extinction of near-limit hydrogen counterflow diffusion flames *Proceedings of the Combustion Institute* Volume 34, Issue 1, 2012, pages 881–886

Grana, R., Seshadri, K., Cuoci, A.,**Niemann, U.**, Faravelli, T., Ranzi, E., Kinetic modelling of extinction and autoignition of condensed hydrocarbon fuels in non-premixed flows with comparison to experiment. *Combustion and Flame* Volume 159, Issue 1, 2012, Pages 130-141

Seiser, R., **Niemann, U.**, Seshadri, K. Experimental study of combustion of n-decane and JP-10 in nonpremixed flows *Proceedings of the Combustion Institute* Volume 33, Issue 1, 2011, Pages 1045-1052

Sarathy, S.M., Westbrook, C. K., Mehl, M., Pitz, W. J., Togbe, C., Dagaut, P., Wang, H., Oehlschlaeger, M.A., **Niemann, U.**, Seshadri, K., Veloo, P.S., Ji, C., Egolfopoulos, F.N., Lu, T., Comprehensive chemical kinetic modeling of the oxidation of 2-methylalkanes from C7 to C20. *Combustion and Flame* Volume 158, Issue 12, 2011, Pages 2338-2357

Seshadri, K., Frassoldati, A., Cuoci, A., Faravelli, T., **Niemann, U.**, Weydert, P., Ranzi, E. Experimental and kinetic modeling study of combustion of JP-8, its surrogates and components in laminar premixed flows. *Combustion Theory and Modelling* Volume 15, Issue 4, 2011, pages 569-583

Niemann, U., Seiser, R., Seshadri, K. Ignition and extinction of low molecular weight esters in nonpremixed flows. *Combustion Theory and Modelling* Volume 14, Issue 6, 2010, pages 875-891

A. Frassoldati, A. Cuoci, T. Faravelli, **Niemann, U.**, Ranzi, E., et al. An experimental and kinetic modeling study of n-propanol and iso-propanol combustion. *Combustion and Flame* Volume 157, Issue 1, 2010, Pages 2-16.

Grana, R., Frassoldati, A., Faravelli, T., **Niemann, U.**, Ranzi, E., et al. An experimental and kinetic modeling study of combustion of isomers of butanol. *Combustion and Flame* Volume 157, Issue 11, November 2010, Pages 2137-2154

Seshadri, K., Lu, T., Herbinet, O., Humer, S., **Niemann, U.**, Pitz, W. J., Seiser, R., et al. Experimental and kinetic modeling study of extinction and ignition of methyl decanoate in laminar non-premixed flows. *Proceedings of the Combustion Institute* Volume 32, Issue 1, 2009, Pages 1067-1074

Honnet, S., Seshadri, K., **Niemann, U.**, Peters, N. A surrogate fuel for kerosene. *Proceedings of the Combustion Institute* Volume 32, Issue 1, 2009, Pages 485-492

Bieleveld, T., Frassoldati, A., Cuoci, A., Faravelli, T., Ranzi, E., **Niemann, U.**, Seshadri, K. (2009). Experimental and kinetic modeling study of combustion of gasoline, its surrogates and components in laminar non-premixed flows. *Proceedings of the Combustion Institute* Volume 32, Issue 1, 2009, Pages 493-500

Niemann, U. The influence of cetane improvers on autoignition and extinction of non-premixed flames burning high molecular weight hydrocarbon fuels and diesel, Master Thesis, Vienna University of Technology

FIELDS OF STUDY

Major Field: **Mechanical Engineering**

Studies in Combustion
Professors Forman A. Williams and Kalyanasundaram Seshadri.

Studies in Fluid Mechanics
Professors Kalyanasundaram Seshadri, Robert J. Cattolica, Daniel
Tartakovsky and Alison Marsden.

ABSTRACT OF THE DISSERTATION

**Experimental and Computational Studies of the Combustion of
Classical and Alternative Fuels**

by

Ulrich Niemann

Doctor of Philosophy in Engineering Sciences (Mechanical Engineering)

University of California, San Diego, 2013

Professor Kalyanasundaram Seshadri, Chair
Professor Forman A. Williams, Co-Chair

Well-controlled laboratory experiments in simplified reactors, such as counterflow burners, most easily and accurately test the ability of chemical-kinetic mechanisms and transport descriptions to predict combustion processes. Diffusion flame investigations at atmospheric and elevated pressures have been carried out to provide insights into the structure and combustion chemistry of hydrogen, low molecular weight hydrocarbons and oxygenated fuels. A newly designed high-pressure combustion facility was used to study the structures and extinction conditions of counterflow diffusion flames in air for nitrogen-diluted hydrogen, methane, ethane, and ethylene, from $0.1\,\mathrm{MPa}$ to $2.0\,\mathrm{MPa}$. In all cases, the strain rate at extinction was found to increase with pressure in the moderate pressure range until a peak value is attained, above which a decreasing trend begins.

In addition, a methane air diffusion flame was doped with hydrogen at atmospheric pressure. Irrespective of whether the hydrogen was added on the fuel or oxidizer side, the ratio of the extinction strain rate with hydrogen addition to that without was the same when the stoichiometric mixture fraction, the adiabatic flame temperature, and the proportion of oxygen that consumes the added fuel are fixed. Furthermore, an experimental investigation of the structure of large alcohols and critical conditions of methyl-esters provide new insights for the development and validation of chemical-kinetic mechanisms.

Chapter 1

Introduction

1.1 Motivation for Combustion Research

Combustion has no equal as the physical process historically most substantial to human existence and society's progress. Yet it is often underestimated for its complexity by the majority of mankind. From striking a match to a burning candle, its presence is so ubiquitous. For millenia the objective had been to control fire rather than to understand it. Only as late as the 18th century during the time of the first industrial revolution the desire arose to understand combustion through analytical studies of isolated combustion phenomena. Combustion science provided solutions to real-world problems which subsequently advanced human safety, manufacturing and transport. Since then the demand for an improved understanding of combustion phenomena and the importance of combustion science for industrial applications such as gas turbines, automotive engines, and industrial furnaces has only increased. Diversification of fuels, efficiency and pollution are concerns brought about by the scarceness of resources and better understanding of the effects of combustion products on the environment and human health . Not only carbon emissions and greenhouse gases, but carcinogenic or toxic substances like some forms of polycyclic aromatic hydrocarbons (PAHs) and aldehydes demonstrate the relevance for an improved understanding of combustion and pollutant formation processes. In many respects combustion is still the most viable and feasible option for transportation and electricity generation and hence impossible to replace sustainably. Yet the dangers and threats can not be ignored but must be addressed diligently. The black box approach as employed in the past in the development of engines is long gone. Detailed

computational approaches like Computational Fluid Dynamics (CFD) employing chemical kinetics is now the accepted standard in the industry. Over the decades the improved theoretical understanding as well as kinetics amplified by a surge in computational power have elevated this branch of science from providing qualitative insight to quantitative predictions. Past progress demonstrates the importance of combustion research, but the possible reward of a deeper understanding and integration of theory, experiments and computations is the motivation for the future.

1.2   Diffusion Flames

The complexity of practical combustion problems requires a detailed understanding of all underlying physical and chemical processes. Therefore it is of interest to test and verify theories and numerical descriptions against simplified experimental formulations, before applying these to engineering applications. Experimental configurations employing homogeneously premixed reactant mixtures are widely used to give insight into the chemical kinetics of combustion since characteristic quantities such as ignition delay time and flame speed are uniquely defined by the thermo-chemical parameters temperature, pressure and reactant concentrations. Many combustion processes are not only defined by their chemistry but involve molecular transport as the characterizing process. In nonpremixed combustion, where fuel and oxidizer are initially separated, reactants diffuse into each other forming a thermal mixing layer. Due to the spatial homogeneity experiments on premixed systems are sufficiently defined in terms of a time scale and can thus be simulated with low computational expense. In nonpremixed systems the complexity of the problem involves at least one spatial dimension since the diffusive nature of this process requires time and length scales (e.g. flow velocities, concentration gradients). The least complex form of diffusion flames is obtained in the counterflow configuration. Its origins lie in the exact solution to the Navier-Stokes equations for a flow impinging on a flat surface as it has been developed by von Karman [1] and which is equally valid for opposing flows. Considerations for chemically reacting flows have been provided by Seshadri and Williams [2]. The mathematical treatment employs a self-similarity transformation which reduces the two-dimensional flowfield such that velocities and subsequently all additional physical parameters are a function of the axial position only and do not vary in the radial direction. The characteristic quantity for diffusion flames is the Damköhler number, the nondimensional ratio of a characteristic flow

time to a characteristic chemical time. While a Damköhler number exists for all flame phenomena, it is a fixed ratio for premixed flames. Since the heat conduction towards the unburned mixture balances the reactive heat generation, the burning velocity, which is an eigenvalue of the problem, equals the flow time. In diffusion flames the reaction takes place where reactants are in stoichiometric proportions and the heat generated is conducted towards both streams, allowing a burning solution for a range of ratios as long as the resulting Damköhler number is above a critical value [3]. For one value of the Damköhler number multiple maximum reaction zone temperature solutions exist. As a consequence the graphical representation relating to these groups of solutions resemble and thus are referred to as the "S-shaped curve" [4, 5] The upper branch of the curve is the burning solution. When the flow time is decreased with respect to the chemical time in the burning regime the solution will approach the left apex of the S at which point the flame will extinguish and drop to the lower branch, or frozen flow regime. If the ratio is now increased the solution will stay on the lower branch approaching the right apex at which point the solution will jump to the upper branch, or burning regime. The points at which these instationary transitions occur, are called the critical conditions of extinction and ignition. The middle branch is physically unstable and thus irrelevant to experimental considerations. While these concepts can be applied to any type of burner combustion, they translate exceptionally well to a diffusion flame stabilized in a counterflow burner. In the counterflow configuration, the chemical time is determined by the composition and thermodynamic state of the streams, while the flow time is determined by the velocity of the streams, or more precisely the strain of the flowfield. It can be seen that from the statements above this configuration provides a degree of freedom that allows convenient determination of critical conditions of extinction and auto-ignition as well as the simplest form of flame structure investigation due to the one-dimensional form of the counterflow stabilized flame.

1.3   Outline of the Dissertation

The work resulting in this dissertation was motivated by two developments, namely the demand for fuels derived from biological sources and the quest for high efficiency and low pollution in the development of internal combustion engines requiring a detailed understanding of fundamental combustion processes. In the context of the studies presented here, hydrogen and hydrocarbons are categorized as classical fu-

els, since they are well-known as either direct fuels for power generation or important primary intermediate species in the oxidation of transportation fuels. Oxygenated fuels, here alcohols and methyl-esters, are categorized as alternative fuels, since the use is a recent development brought about by demands for carbon-neutral fuels from biological sources.

A key aspect of making biofuels a viable option as transportation fuels in the future is to understand their combustion characteristics, chemical pathways and the formation of intermediate species. While the combustion characteristics are mostly relevant to achieve optimal performance, human health and environment can be impacted by byproducts of oxygenated fuel combustion, even in small concentrations. These are often more hazardous (toxic, carcinogenic) than byproducts from fossil fuels because organic compounds are more readily absorbed by the human body. This motivated studies presented in Chapter 4 containing experimental data on flame structure of alcohols that are used to validate chemical-kinetic schemes and their predictions on species formation.

The logistics of supplying fuels to the armed forces across the globe is a crucial, complex and expensive mission. While some of the cost is unavoidable, using a single type of fuel is expected to reduce the expense significantly. The United States Army is currently developing technologies to facilitate diesel-powered equipment and equipment employing spark-ignition combustion to be powered by the aviation fuel, JP-8. This conversion is a complicated process and many fuel related issues have to be considered. Since the combustion chamber in an internal combustion engine is pressurized, special attention is given to combustion research in the elevated pressure regime. Funding by the U.S. Army was allocated under the objective to design and build a facility which would allow to conduct experimental studies of combustion phenomena under engine-like pressures. A detailed description of the facility is provided in Appendix B. The counterflow configuration was chosen to elucidate the behavior of diffusion flames at elevated pressure. Experimental investigations presented in Section 3.1 show the dependence of extinction of hydrogen diffusion flames with respect to pressure. A similar study for low molecular weight hydrocarbon fuels, namely methane, ethane, and ethylene is presented in Section 3.2. Temperature measurements provide additional information used in subsequent sections for the validation of chemical-kinetic mechanisms.

Experimental studies as performed here require an array of very specific equipment and apparatuses, some of which are unique. The demand for ever more detailed

information as science progresses must be matched with efforts to ensure engineering precision of the employed facilties. Boundary conditions exactly defined in computational models must be rigorously enforced during experiments. Removing the influence of human induced error and/or inaccuracies through automation and computer control is becoming increasingly important. Efforts to provide improvements to existing equipment and the design of new prototypes are covered in Appendix A and Section 4.1. Descriptions of a high pressure counterflow facility are provided in Appendix B.

1.4   Summary

In summary, laminar counterflow diffusion flames for two groups of fuels are addressed: classical and alternative fuels. These studies include gaseous, prevaporized and liquid fuels at atmospheric pressure and gaseous low molecular weight fuels in the atmospheric and elevated pressure regime. Contributions to the understanding of non-premixed combustion with implications for computational modelling, through improved chemical-kinetic descriptions, are presented.

References

[1] H. Schlichting. *Boundary-Layer Theory*. Mc Graw Hill, Inc, 1968.

[2] K. Seshadri and F. A. Williams. Laminar flow between parallel plates with injection of a reactant at high Reynolds number. *International Journal of Heat and Mass Transfer*, 21(2):251–253, 1978.

[3] A. Liñán. The asymptotic structure of counterflow diffusion flames for large activation energies. *Acta Astronautica*, 1:1007–1039, July 1974.

[4] F. E. Fendell. Ignition and extinction in combustion of initially unmixed reactants. *Journal of Fluid Mechanics*, 21(2):281–303, 1965.

[5] L. Krishnamurthy, F. A. Williams, and K. Seshadri. Asymptotic theory of diffusion-flame extinction in the stagnation-point boundary layer. *Combustion and Flame*, 26:363–377, 1976.

Chapter 2

Influence of Hydrogen on the Structure of Methane Flames

2.1 Overview

There is considerable current interest in the combustion of mixtures of methane and hydrogen, for example in connection with gas-turbine and other applications [1, 2]. Among the related questions that arise is whether it is more advantageous to introduce the hydrogen in the fuel or air stream. While autoignition and flashback are of major concern in such decisions, possibilities of flamelet extinction also need to be addressed. A fundamental understanding of the differences in flamelet-extinction behavior for fuel-side and air-side hydrogen addition is, however, lacking. The present work is intended to improve our basic knowledge of the associated trade-offs between fuel-side and oxidizer-side addition of a reactant different from those participating in the original diffusion flame. Hydrogen is not the only additional reactant that may be considered for injection into one or the other stream. Carbon monoxide, for example, another constituent of syngas, also may be of interest as an added reactant. For this reason, a general formulation is presented here that is applicable for the addition of any reactant to either or both streams. While the development is given for only one added reactant, it can easily be generalized to more than one, and although the stoichiometry is selected to be that of H_2 and CO with O_2, the formulation readily admits arbitrary stoichiometry. It is possible that, especially with a reactant added to the oxidizing stream, two reaction zones may develop, separated by a convective-diffusive zone, as has recently

been inferred in one case far from extinction with nitrogen chemistry [3]. That type of behavior is excluded here, it being assumed that there is just one reaction zone where the fuel, oxidizer, and added reactant are all consumed, as observed in the experiments reported here. The experiments, which are described after the general formulation is presented, involve counterflow diffusion flames at 1 atm between a fuel stream consisting of a mixture of CH_4 and N_2 and an oxidizer stream consisting of a mixture of O_2 and N_2, with H_2 added either to the fuel stream or to the oxidizer stream. While Lewis numbers of unity are good approximations for these reactants as well as for the diluent prior to H_2 addition, the high diffusivity of H_2 makes it important to account for the fact that its Lewis number differs from unity. This is the reason that the following formulation addresses the addition of a nonequidiffusional reactant. It will be seen how the necessary modifications that this requires can be introduced without excessive difficulty. The approach follows the mixture-fraction formulation of Peters [4, 5]. Although formulations have been developed for diffusion flames in which the fuel and oxidizer have different Lewis numbers [6–10], equidiffusional diffusion flames with an added reactant having a different Lewis number have not been addressed before in a similar manner.

2.2 Formulation for the Convective-Diffusive Regions

Consider a hydrocarbon fuel C_nH_{2m}, denoted by F, and a nonequidiffusional reactant, denoted by R, two molecules of which react with O_2 to form products. Examples of R would be H_2 or CO. Although generalization of these specific choices is straightforward, the choices apply to many applications, such as that considered here, and they facilitate concrete comprehension. Lewis numbers are assumed to be unity for all species except R, and the complete chemistry is assumed to occur at a particular spatial (x) position denoted by x_{st}. The fuel stream may contain R and N_2, in addition to F, and the oxidizer stream is a mixture of O_2, N_2, and possibly R as well. Let a_{RF} denote the number of moles of R per mole of fuel in the fuel stream and a_{RO} the number of moles of R per mole of O_2 in the oxidizer stream. The overall reaction that occurs at $x = x_{st}$ is then

$$F + (1/2)(2n + m + a_{RF} + a_{RO})O_2 + (a_{RF} + a_{RO})R \rightarrow nCO_2 + mH_2O + (a_{RF} + a_{RO})RO, \quad I$$

where RO stands for H_2O or CO_2, depending on what R is. It is convenient to let $s = (2n + m)/2$ denote the stoichiometric number of moles of O_2 required to burn one

mole of F and $r = (a_{RF} + a_{RO})/(2s)$ be the ratio of the number of moles of O_2 needed to burn $a_{RF} + a_{RO}$ moles of R to the number required to burn one mole of F. This last parameter r will play a central role in the following development.

Let F enter the reaction region from $x < x_{st}$ and O_2 enter from $x > x_{st}$. The diffusive fluxes into the reaction region must obey jump conditions consistent with the overall reaction I, as well as obeying the diffusion-flame conditions that the mass fractions $Y_F = 0$ for $x > x_{st}$, and $Y_{O_2} = 0$ for $x < x_{st}$. Thus, with W_i denoting the molecular weight of species i, so that the stoichiometric mass ratios, oxidizer-to-fuel and oxidizer-to-additive, respectively, are $\nu = sW_{O_2}/W_F$ and $\mu = W_{O_2}/(2W_R)$, the relationships

$$
\begin{aligned}
\nu(1+r)\,(dY_F/dx)_- &= -\,(dY_{O_2}/dx)_+\,, \\
\mu(1+r)[(dY_R/dx)_+ - (dY_R/dx)_-] &= rLe\,(dY_{O_2}/dx)_+\,, \\
(dY_{N_2}/dx)_- &= (dY_{N_2}/dx)_+\,,
\end{aligned}
\tag{2.1}
$$

must apply, where the subscripts $+$ and $-$ identify conditions at $x = x_{st}$ on the side $x > x_{st}$, and $x < x_{st}$ respectively. Here Le denotes the Lewis number of R, which equals the ratio of the diffusion coefficients of other species to that of R. These balances arise from the fact that $1/(1+r)$ is the fraction of the O_2 molar flux that reacts with F, and $r/(1+r)$ is the fraction that reacts with R.

It is useful to introduce two different mixture fractions, Z and Z_R, both defined to be unity in the fuel stream, and zero in the oxidizer stream. Then, for example, in the counterflow configuration, with u denoting the velocity in the x direction, ρ the density and D the diffusion coefficient of all species except R, these two mixture fractions are defined to obey the differential equations

$$
\rho u \frac{dZ}{dx} = \frac{d}{dx}\left(\rho D \frac{dZ}{dx}\right)
\tag{2.2}
$$

and

$$
\rho u \frac{dZ_R}{dx} = \frac{d}{dx}\left(\frac{\rho D}{Le}\frac{dZ_R}{dx}\right).
\tag{2.3}
$$

Similar equations can be derived for other nonpremixed systems, such as stagnant diffusion layers or fuel-droplet burning.

The advantage of introducing these definitions is that, since away from the reaction region the mass fractions of all species except R obey Equation 2.2, while that of R obeys Equation 2.3,

$$
\begin{aligned}
Y_i &= A_{i,\pm} + B_{i,\pm}Z,\quad i{\neq}R, \\
Y_R &= A_{R,\pm} + B_{R,\pm}Z_R,
\end{aligned}
\tag{2.4}
$$

where A's and B's are constants, the subscripts $+$ or $-$ indicating their values for $x > x_{\text{st}}$ or $x < x_{\text{st}}$, respectively. The solution to Equation 2.2 with the stated boundary conditions yields a function $Z(x)$, having the value $Z_{\text{st}} = Z(x_{\text{st}})$ at $x = x_{\text{st}}$, while the solution to Equation 2.3 similarly yields a function $Z_{\text{R}}(x)$, having the value $Z_{\text{R,st}} = Z_{\text{R}}(x_{\text{st}})$ at $x = x_{\text{st}}$. Since $Z(x)$ and $Z_{\text{R}}(x)$ are different functions, in general it will be found that $Z_{\text{st}} \neq Z_{\text{R,st}}$.

The constants in Equation 2.4 can be determined in terms of the values of Z_{st} and $Z_{\text{R,st}}$ from the composition of the two streams and the requirements that $Y_{\text{F}} = 0$, $Y_{\text{R}} = 0$, and $Y_{\text{O}_2} = 0$ at $x = x_{\text{st}}$. If $a_{\text{N}_2\text{F}}$ denote the number of moles of N_2 per mole of fuel in the fuel stream and $a_{\text{N}_2\text{O}}$ denotes the number of moles of N_2 per mole of O_2 in the oxidizer stream, then in the fuel stream the mass fraction of the constituents are

$$Y_{\text{FF}} = \frac{W_{\text{F}}}{W_{\text{F}} + a_{\text{N}_2\text{F}}W_{\text{N}_2} + a_{\text{RF}}W_{\text{R}}}$$

$$Y_{\text{RF}} = \frac{a_{\text{RF}}W_{\text{R}}}{W_{\text{F}} + a_{\text{N}_2\text{F}}W_{\text{N}_2} + a_{\text{RF}}W_{\text{R}}}, \tag{2.5}$$

and $Y_{\text{N}_2\text{F}} = 1 - Y_{\text{FF}} - Y_{\text{RF}}$. In the oxidizer stream the mass fractions are

$$Y_{\text{O}_2\text{O}} = \frac{W_{\text{O}_2}}{W_{\text{O}_2} + a_{\text{N}_2\text{O}}W_{\text{N}_2} + a_{\text{RO}}W_{\text{R}}}$$

$$Y_{\text{RO}} = \frac{a_{\text{RO}}W_{\text{R}}}{W_{\text{O}_2} + a_{\text{N}_2\text{O}}W_{\text{N}_2} + a_{\text{RO}}W_{\text{R}}}, \tag{2.6}$$

and $Y_{\text{N}_2\text{O}} = 1 - Y_{\text{O}_2\text{O}} - Y_{\text{RO}}$. In terms of these values,

$$A_{\text{F},-} = -\frac{Y_{\text{FF}}Z_{\text{st}}}{1 - Z_{\text{st}}}, \quad A_{\text{O}_2,-} = 0, \quad A_{\text{R},-} = -\frac{Y_{\text{RF}}Z_{\text{R,st}}}{1 - Z_{\text{R,st}}},$$

$$B_{\text{F},-} = \frac{Y_{\text{FF}}}{1 - Z_{\text{st}}}, \quad B_{\text{O}_2,-} = 0, \quad B_{\text{R},-} = \frac{Y_{\text{RF}}}{1 - Z_{\text{R,st}}}, \tag{2.7}$$

and

$$A_{\text{F},+} = 0, \quad A_{\text{O}_2,+} = Y_{\text{O}_2\text{O}}, \quad A_{\text{R},+} = Y_{\text{RO}},$$

$$B_{\text{F},+} = 0, \quad B_{\text{O}_2,+} = -Y_{\text{O}_2\text{O}}/Z_{\text{st}}, \quad B_{\text{R},+} = -Y_{\text{RO}}/Z_{\text{R,st}}, \tag{2.8}$$

while

$$A_{\text{N}_2,\pm} = Y_{\text{N}_2\text{O}}, \quad B_{\text{N}_2,\pm} = Y_{\text{N}_2\text{F}} - Y_{\text{N}_2\text{O}}. \tag{2.9}$$

for the inert diluent.

Use of these results in the first equality in Equation 2.1 determines Z_{st} as

$$Z_{\text{st}} = [1 + \nu(1 + r)(Y_{\text{FF}}/Y_{\text{O}_2\text{O}})]^{-1}. \tag{2.10}$$

While the third equality in Equation 2.1 is automatically satisfied by Equation 2.9, the second equality determines $Z_{\text{R,st}}$ by the formula

$$\frac{Y_{\text{RO}}}{Z_{\text{R,st}}} + \frac{Y_{\text{RF}}}{1 - Z_{\text{R,st}}} = \frac{LeY_{\text{O}_2\text{O}}r}{\mu Z_{\text{st}}(1 + r)}\left(\frac{dZ}{dx}\right)_{\text{st}} \bigg/ \left(\frac{dZ_{\text{R}}}{dx}\right)_{\text{st}}, \tag{2.11}$$

which is necessarily implicit because it depends on the derivative of the function $Z_R(x)$ at $x = x_{st}$. Nevertheless, once the functions $Z(x)$ and $Z_R(x)$ are obtained, Equation 2.11 would determine $Z_{R,st}$, consistent with employing Equation 2.10 in the solution to Equation 2.2 to find x_{st}, then simply evaluating the solution to Equation 2.3 at this value of x. The central parameters r and Le appear here, along with others.

With a Lewis number of unity for all species except R, energy conservation provides an equation like the first expression in Equation 2.4 for the thermal enthalpy, with jump conditions like the first expression in Equation 2.1. If the specific heat, c_p, is constant and T_1 and T_2 denote the temperatures of the fuel and oxidizer streams, respectively, then application of the jump condition shows that at $x = x_{st}$ the temperature is

$$T_{st} = T_2 + (T_1 - T_2)Z_{st} + \left(\frac{Q_F + 2rsQ_R}{c_p W_F} \right) \left(\frac{Y_{FF}Y_{O_2O}}{Y_{O_2O} + \nu(1+r)Y_{FF}} \right) \tag{2.12}$$

where Q_F denotes the heat released per mole of fuel consumed, and Q_R is the heat release per mole of R consumed. This is simply the adiabatic flame temperature of a stoichiometric mixture of the two streams. Because of the required stoichiometric relationship between fluxes of R and O_2, it is possible to express T_{st} in a form independent of $Z_{R,st}$ and therefore independent of Le, as is done here for convenience. This implies that the limit of vanishing fuel sometimes is singular because, in that limit, if, for example, $a_{RO} = 0$, so that there is a diffusion flame involving R and O_2, the value of T_{st} is known to depend on Le, in general.

It now only remains to determine the functions $Z(x)$ and $Z_R(x)$ from solutions to Equation 2.2 and Equation 2.3. These solutions, in general, depend on the variations of ρ, u, and D with x. In a classical counterflow problem, ρ and D are taken to be constant, and $u = ax$, where the strain rate a is constant, and x is the distance from the stagnation plane. In this case

$$Z = \frac{1}{2}\text{erfc}\left(\frac{x}{\sqrt{2D/a}} \right), \quad Z_R = \frac{1}{2}\text{erfc}\left(\frac{x\sqrt{Le}}{\sqrt{2D/a}} \right), \tag{2.13}$$

which results in

$$\left(\frac{dZ_R}{dx} \right)_{st} = \left(\frac{dZ}{dx} \right)_{st} \sqrt{Le} \exp\left[\frac{x_{st}^2(1 - Le)}{(2D/a)} \right], \tag{2.14}$$

a relation readily employed in Equation 2.11 and also obtainable from the analysis of Kim and Williams [11] for small Z_{st}, without the approximations of constant ρ and D.

2.3 Description of the Reaction Zone

Different levels of description of the structure of the reaction zone for use in the finite-rate chemical-kinetic analysis needed to address flame extinction range from empirical one-step activation-energy asymptotics to numerical computations with detailed chemistry. Studies by rate-ratio asymptotics of the structures of laminar premixed and nonpremixed flames indicate that the reaction zones of flames burning many hydrocarbon and alcohol fuels are made up of two layers—an inner layer where the fuel reacts with radicals to form the intermediate species CO and H_2 and an oxidation layer where these intermediate species are oxidized to CO_2 and H_2O, and O_2 is consumed [12–17]. The intermediate species CO and H_2 are found to play correspondingly important roles in detailed-chemistry computations, thereby supporting the understanding developed from rate-ratio asymptotics. As indicated in the introduction, these two intermediates also are examples of nonequidiffusional reactants that can be added to either one of the reactant streams, or to both of them. Because of the two-layer structure of the reaction zone, it is unclear in advance whether addition of the intermediate to one stream will have the same effect as its addition to the other. Indeed, even with one-step activation-energy asymptotics, the single-layer reaction-zone structure is different in detail depending on the stream to which a given reactant is added [18–20], as may already be surmised from the different reaction-zone concentration profiles of fuel and oxidizer in classical one-step activation-energy asymptotics [21]. Calculated conditions for extinction therefore may depend on the choice of the stream to which the reactant is added.

In comparing influences of reactant addition to different streams, choices must be made about what parameters to keep fixed. Because of the strong temperature dependencies of reaction rates, it is most important to make comparisons at fixed values of T_{st}. Otherwise differences associated with different reaction-zone temperatures are likely to dominate the results. After removal of effects of temperature variations, structures of reaction zones still vary with the stoichiometric mixture fraction [22, 23], for example exhibiting steeper oxygen profiles and shallower fuel profiles at small values of Z_{st} and the opposite for Z_{st} near unity. It is therefore also desirable to make comparisons at fixed values of Z_{st}. It is relevant to observe, for example from Equation 2.13, that with Z_{st} specified, the value of x_{st} and hence of $Z_{\mathrm{R,st}}$ also is determined. Fixing one stoichiometric mixture fraction therefore automatically fixed the other. That choice also fixes the two derivatives on the right-hand side of Equation 2.11, so that that equation provides a

relationship among Y_{RO}, Y_{RF}, and the ratio r of the fraction of oxidizer that reacts with R to the fraction that reacts with F. That last trade-off may be the dominant factor affecting the flame structure and extinction at fixed values of T_{st} and Z_{st}. The following experiments are designed to test the extent to which this hypothesis is true. Comparisons are made below only for the limiting values of zero (oxidizer-stream addition) and infinity (fuel-stream addition) for the ratio $Y_{\text{RF}}/Y_{\text{RO}}$, with the consequent influence on the reaction zone studied by measuring the counterflow extinction strain rate.

2.4 Experimental and Computational Studies

A schematic illustration of the counterflow configuration employed in the experimental and computational study is shown in Figure 2.1. The counterflow burner has
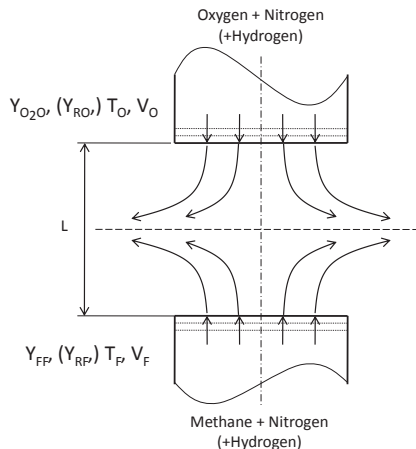
Figure 2.1: Schematic illustration of the counterflow configuration with the corresponding notation for the boundary parameters

.

two ducts with fine wire screens placed at their exits, allowing accurate enforcement of plug-flow boundary conditions in computational modelling. From the fuel duct, a fuel stream made up of methane and nitrogen is injected toward the mixing layer with an injection velocity V_1. From the oxidizer duct, an oxidizer stream made up of a mixture of oxygen and nitrogen is injected at an injection velocity V_2. A convenient parameter to characterize the residence time is the reciprocal of the oxygen-side strain rate, a_{O}, given by [24]

$$a_{\text{O}} = \frac{2|V_2|}{l}\left(1 + \frac{|V_1|\sqrt{\rho_{\text{F}}}}{|V_2|\sqrt{\rho_2}}\right). \tag{2.15}$$

Here ρ_F and ρ_2 are the densities of the reactant streams at the injection plane of the fuel duct and at the injection plane of the oxidizer duct, respectively. The separation distance between the ducts is $l = 10\,\text{mm}$ in these experiments. The experimental studies were conducted with the momenta of the counterflowing streams kept equal to each other, that is, with $\rho_F V_1{}^2 = \rho_2 V_2{}^2$.

In the experiments, the pressure is normal atmospheric and the temperatures at the boundaries are maintained at $T_1 = T_2 = 298\,\text{K}$. The molecular weights of the reactants are $W_F = W_{CH_4} = 0.016\,\text{kg/mol}$, $W_{O_2} = 0.032\,\text{kg/mol}$, and $W_R = W_{H_2} = 0.002\,\text{kg/mol}$. For the chemical system considered here, $s = 2$, $\nu = 4$ $\mu = 8$, $Q_F = 803\,\text{kJ/mol}$, and $Q_R = 242\,\text{kJ/mol}$. Previous studies have established that a reasonable value for the Lewis number for hydrogen is $Le = Le_{H_2} = 0.3$ [25]. The structure of the reactive flow field then depends on three independent parameters, given by the boundary values of mass fractions of reactants Y_{FF}, Y_{O_2O}, and either Y_{RF} or Y_{RO}, depending on the stream to which H_2 is added. These boundary values are chosen so that $Z_{st} = 0.055$. At this value of, Z_{st}, it follows from the first expression in Equation 2.13 that $x_{st}/\sqrt{2D/a} = 1.13$. Hence $x_{st}\sqrt{Le}/\sqrt{2D/a} = 0.62$. Using the last expression in Equation 2.13, it is then found that $Z_{R,st} = 0.19$, and the value of the factor multiplying $Y_{O_2O}r/(1 + r)$ on the right-hand side of Equation 2.11 is found to be 0.51. The experiments are conducted at fixed adiabatic flame temperatures of $T_{st} = 2000\,\text{K}$ and $T_{st} = 2100\,\text{K}$. Since Equations 2.10, 2.11, and 2.12 give three relations among the boundary values of the mass fractions of the reactants and r, varying Y_{RF} with $Y_{RO} = 0$ is equivalent to varying r, as is varying Y_{RO} with $Y_{RF} = 0$.

Critical conditions for extinction are measured in these experiments. With oxidizer-side addition, at a selected value of Y_{RO}, the values of r, Y_{FF}, and Y_{O_2O} are determined by Equations 2.10, (2.11), and (2.12), with T_{st} taken to be the adiabatic flame temperature calculated employing NASA thermodynamic data [26]. The experimental conditions are adjusted to reproduce the resulting values of Y_{FF}, and Y_{O_2O}. A flame is first stabilized at convenient values of V_1 and V_2, then the velocities are increased until extinction is observed. The velocities of the reactant streams at the boundaries are calculated as the ratio of their volumetric flow rates to the cross-section area of the ducts. All gaseous flow rates are set by computer-regulated mass flow controllers having calibrated accuracies within $\pm 1\%$. The oxidizer-side strain rate at extinction, $a_{2,E}$ is then calculated using Equation 2.15 and recorded as a function of Y_{RO} by repeating the

experiment for different values of Y_{RO}. A similar procedure is followed with hydrogen added to the fuel stream. Experimental uncertainty is primarily introduced through the inaccuracy of the volume flow rates of the highly reactive hydrogen. Extinction calculations employing the limits of possibly inaccurate hydrogen concentrations are conducted, thus determining the range of experimental uncertainty, indicating that the accuracy of extinction strain rates is within $\pm 5\%$. Figure 2.2 is a photograph of a methane flame
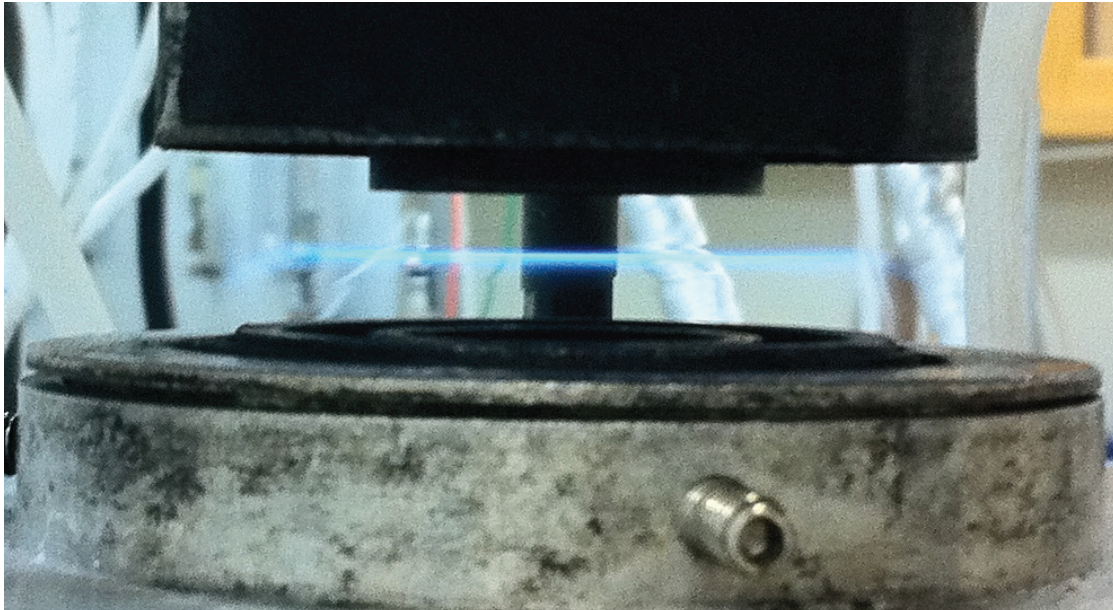
Figure 2.2:   Photograph of a flame that is stabilized in the counterflow burner. The mass fraction of fuel in the fuel stream is $Y_{FF} = 0.492$. The mass fraction of oxygen in the oxidizer stream is $Y_{O_2O} = 0.175$. The mass fraction of hydrogen that is added to the fuel stream is $Y_{RF} = 0.025$. The strain rate is $a_O = 300\,\mathrm{s}^{-1}$

.

stabilized in the counterflow burner. Hydrogen is added to the fuel stream. The oxidizer stream is a mixture of oxygen and nitrogen.

The chemical-kinetic scheme employed in the calculations [27, 28] involves 53 species with 470 elementary reactions when forward and backward steps are counted separately. This San Diego Mechanism has been tested by comparing predictions of aspects of combustion of hydrogen [29], carbon monoxide [29], methane [30, 31], ethane [32], acetylene [33], propane [34], methanol [35–37], and ethanol [38, 39] with experimental data. Computations were performed by the computer programs OpenSMOKE [40, 41] and CHEMKIN [42] with mixture-averaged diffusion coefficients for various species and including radiative heat loss and thermal (Soret) diffusion. Calculations employing multi-

component diffusion were performed as well with CHEMKIN (the only code with that option) and exhibited extinction strain rates generally lower but showed qualitatively similar results with respect to the addition of hydrogen. Dynamical adaptive meshing techniques were used to account for strong gradients within the computational domain with calculated extinction conditions, defined by convergence to non-reacting solutions, confirmed to be grid-insensitive.

2.5   Results and Comparisons

Figures 2.3 and 2.4 show critical conditions for extinction. In these figures the symbols represent experimental data, and the curves represent computational predictions. These curves are boundaries separating flammable regions below from non-flammable regions above. Figure 2.3 shows the oxygen-side strain rate at extinction,
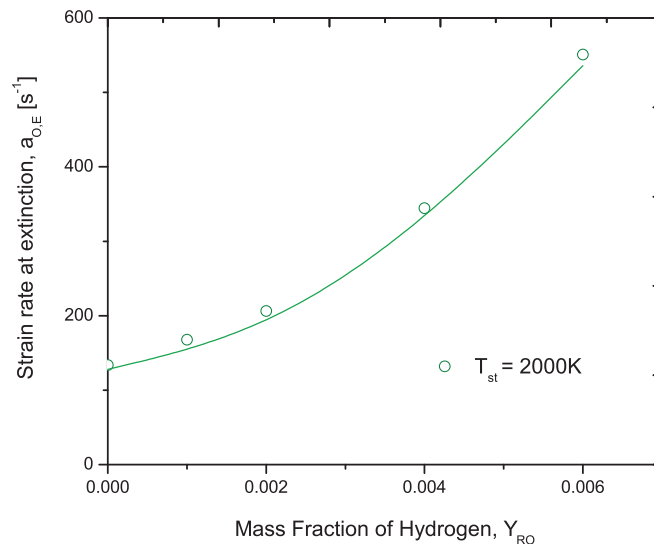
Figure 2.3: The strain rate at extinction, $a_{2,\mathrm{E}}$ as a function of mass fraction of hydrogen in the oxidizer stream, Y_{RO}, at fixed $Z_{\mathrm{st}} = 0.055$, and $T_{\mathrm{st}} = 2000\,\mathrm{K}$. The symbols represent experimental data and the curve represents predictions obtained using the San Diego Mechanism [27, 28].

$a_{2,\mathrm{E}}$, as a function of the mass fraction of hydrogen in the oxidizer stream, Y_{RO}, at fixed $Z_{\mathrm{st}} = 0.055$, and $T_{\mathrm{st}} = 2000\,\mathrm{K}$. Figure 2.4 shows critical conditions for extinction with hydrogen added to the fuel stream at fixed $Z_{\mathrm{st}} = 0.055$, for both $T_{\mathrm{st}} = 2100\,\mathrm{K}$ and $T_{\mathrm{st}} = 2000\,\mathrm{K}$. In both of these figures the experimental data and predictions show that the value of $a_{2,\mathrm{E}}$ increases with increasing amounts of hydrogen in the reactant streams.
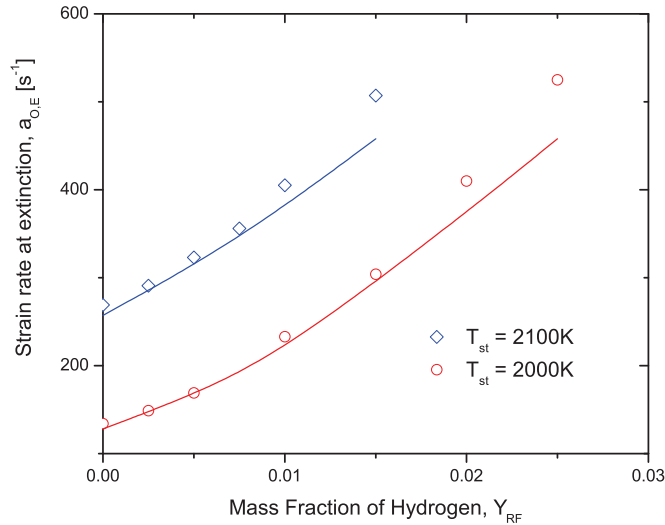
Figure 2.4: The strain rate at extinction, $a_{2,\mathrm{E}}$ as a function of mass fraction of hydrogen in the fuel stream, Y_{RF}, at fixed $Z_{\mathrm{st}} = 0.055$, and $T_{\mathrm{st}} = 2100\,\mathrm{K}$, and $T_{\mathrm{st}} = 2000\,\mathrm{K}$. The symbols represent experimental data and the curves represent predictions obtained using the San Diego Mechanism [27, 28].

Thus, addition of hydrogen either to the oxidizer stream or to the fuel stream delays extinction, as expected because of its high reactivity.

The predictions in Figure 2.3 agree well with experimental data. The predictions in Figure 2.4 also agree well with experimental data at low values of Y_{RF}, but at higher values of Y_{RF} the predicted values of $a_{2,\mathrm{E}}$ are below the measured values by amounts that approach 20 %. The computed difference for fuel-side addition thus eventually exceeds the 5 % experimental uncertainity. Moreover, the computational results are robust in that entirely different programs yield essentially the same results when the same options are selected. The fact that these differences do not appear for the oxidizer-side addition is likely due to the small value of the stoichiometric mixture fraction that was selected, resulting in smaller levels of oxidizer-side hydrogen addition needed to achieve the same variation in the extinction strain rate. In mixture-fraction space, there is a much greater amount of hydrogen diffusion with fuel-side addition, resulting in a greater sensitivity of predictions to the selected description of diffusion. For these reasons, it is most logical to attribute the discrepancies observed for fuel-side addition to inadequacies in the diffusion descriptions in the codes.

It is known that conventional diffusion approximations are inaccurate for mixtures containing hydrogen [43]. In particular, the mixture-average diffusion descriptions

that are common in the codes and that are employed here are known to become inaccurate when the hydrogen concentrations become appreciable. While multi-component diffusion descriptions should provide better agreement, the fact that they did not when that option was exercised in CHEMKIN suggests that improvements in that, too, should be considered. In view of these difficulties, the computational results for the higher fuel-side hydrogen addition are excluded in the following comparisons, use instead being made of the more accurate experimental results there. The data in Figures reffig:oxidizerside
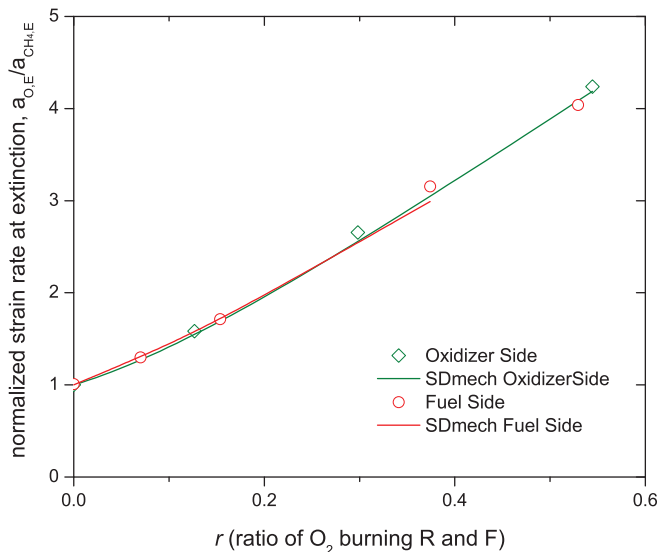
Figure 2.5: The normalized strain rate at extinction, $a_{2,E}/a_{CH_4,E}$ as a function of r at fixed $Z_{st} = 0.055$, and $T_{st} = 2000\,\mathrm{K}$. The symbols represent experimental data and the curves represent predictions obtained using the San Diego Mechanism [27, 28].

and 2.4 for $T_{st} = 2000\,\mathrm{K}$ can be plotted as a function of r to test the hypothesis posed in Section 2.3. This is done in Figure 2.5, which shows the extinction strain rate, normalized by the extinction strain rate without hydrogen addition, as a function of r, for both oxidizer-side and fuel-side addition, at the same values of Z_{st} and T_{st}. The computational results for fuel-side addition in this figure are extended only up to the value of r at which the predictions are trusted. This range, however, extends well into regimes of practical applications, for example with 16 mole percent hydrogen in the fuel mixture. The extremely close agreement seen in this figure, for both computation and experiment and for both fuel side and oxidizer side hydrogen addition, is truly remarkable. The results thus provide both experimental and computational support for the hypothesis.

2.6　Concluding Remarks

A Burke-Schumann (flame-sheet) formulation was developed for diffusion flames between a fuel and oxidizer with Lewis numbers of unity, subject to addition to the fuel and/or oxidizer stream of a different reactant for which the Lewis number differs from unity. This formulation was applied to laminar counterflow diffusion-flame experiments, in which hydrogen was added to either methane-nitrogen mixtures or oxygen-nitrogen mixtures at normal atmospheric pressure, with both feed streams at normal room temperature. The ratio of the fraction of the oxidizer flux that consumes hydrogen to the fraction that consumes fuel was calculated from the new Burke-Schumann formulation, and it was found that, within experimental uncertainty, the ratio of the extinction strain rate with hydrogen addition to that without was the same at any given value of this oxygen flux ratio, irrespective of whether the hydrogen was added on the fuel or oxidizer side. This experimental result was also in close agreement with computational predictions employing detailed chemistry. These results imply that differences in detailed hydrogen concentration profiles within the reaction zone have little or no influence on the chemical kinetics of extinction when the stoichiometric mixture fraction, the adiabatic flame temperature, and the proportion of oxygen that consumes the added fuel are fixed. This same correspondence may be expected to apply for other fuels and additives.

Acknowledgement

References

[1] R. W. Schefer. Combustion of hydrogen-enriched methane in a lean premixed swirl burner. Proceedings of the 2001 DOE Hydrogen Program Review NREL/CP-570-30535, 2001.

[2] T. Wallner, H. K. Ng, and R. W. Peters. The effects of blending hydrogen with methane on engine operation, efficiency, and emissions. Paper # 2007-01-0474, SAE International, 2007.

[3] T. Newmann-Lehman, R. Grana, K. Seshadri, and F. A. Williams. The structure and extinction of nonpremixed methane/nitrous oxide and ethane/nitrous oxide flames. *Proceedings of the Combustion Institute*, 34:2147–2153, 2012.

[4] N. Peters. Local quenching due to flame stretch and non-premixed turbulent combustion. *Combustion Science and Technology*, 30:1–17, 1983.

[5] N. Peters. Laminar diffusion flamelet models in non-premixed turbulent combustion. *Progress in Energy and Combustion Science*, 10:319–339, 1984.

[6] A. Liñán. The structure of diffusion flames. In M. Onofri and A. Tesci, editors, *Fluid Dynamical Aspects of Combustion*, pages 11–29. Longman Scientific and & Technical, Essex, England, 1991.

[7] A. Liñán and F. A. Williams. Volume 34 of *Oxford Engineering Science Series*. Oxford University Press, New York, 1993.

[8] K. Seshadri and C. Trevino. The influence of the lewis numbers of the reactants on the asymptotic structure of counterflow and stagnant diffusion flames. *Combustion Science and Technology*, 64:243–261, 1989.

[9] F. F. Fachini and K. Seshadri. Rate-ratio asymptotic analysis of nonpremixed n-heptane flames. *Combustion Science and Technology*, 175:125–155, 2003.

[10] S. H. Chung and C. K. Law. Structure and extinction of convective diffusion flames with general lewis numbers. *Combustion and Flame*, 52:59–79, 1983.

[11] J. S. Kim and F. A. Williams. Structures of flow and mixture-fraction fields for counterflow diffusion flames with small stoichiometric mixture fractions. *SIAM Journal on Applied Mathematics*, 53:1551–1566, 1993.

[12] N. Peters and F. A. Williams. The asymptotic structure of stoichiometric methane-air flames. *Combustion and Flame*, 68(2):185–207, 1987.

[13] K. Seshadri and N. Peters. Asymptotic structure and extinction of methane-air diffusion flames. *Combustion and Flame*, 73:23–44, 1988.

[14] K. Seshadri and F. A. Williams. Reduced chemical systems and their application in turbulent combustion. In P. A. Libby and F. A. Williams, editors, *Turbulent Reacting Flows*, pages 153–210. Academic Press, San Diego, California, 1994.

[15] K. Seshadri, N. Peters, and F. A. Williams. Asymptotic analyses of stoichiometric and lean hydrogen-air flames. *Combustion and Flame*, 96:407–427, 1994.

[16] K. Seshadri. Multistep asymptotic analyses of flame structures. *Proceedings of the Combustion Institute*, 26:831–846, 1996.

[17] X. S. Bai and K. Seshadri. Rate-ratio asymptotic analysis of non-premixed methane flames. *Combustion Theory and Modelling*, 3:51–75, 1999.

[18] N. Peters. Partially premixed diffusion flamelets in non-premixed turbulent combustion. *Proceedings of the Combustion Institute*, 20:353–360, 1984.

[19] K. Seshadri, I. Puri, and N. Peters. Experimental and theoretical investigation of partially premixed diffusion flames at extinction. *Combustion and Flame*, 61:237–249, 1985.

[20] K. Seshadri and X. S. Bai. Rate-ratio asymptotic analysis of the structure and extinction of partially premixed flames. *Proceedings of the Combustion Institute*, 31:1181–1188, 2006.

[21] A. Liñán. The asymptotic structure of counterflow diffusion flames for large activation energies. *Acta Astronautica*, 1:1007–1039, July 1974.

[22] A. Grudno and K. Seshadri. Characteristic residence times of laminar nonpremixed flames at extinction. *Combustion Science and Technology,*, 112:199–210, 1996.

[23] J. Du and R. L. Axelbaum. The effects of flame structure on extinction of CH_4-O_2-N_2 Diffusion Flames. *Proceedings of the Combustion Institute*, 26:1137–1142, 1996.

[24] K. Seshadri and F. A. Williams. Laminar flow between parallel plates with injection of a reactant at high Reynolds number. *International Journal of Heat and Mass Transfer*, 21(2):251–253, 1978.

[25] M. D. Smooke. Reduced kinetic mechanisms and asymptotic approximation for methane-air flames. Volume 384 of *Lecture Notes in Physics*. Springer Verlag, Heidelberg, 1991.

[26] NIST-JANAF Thermochemical Tables. http://kinetics.nist.gov/janaf/.

[27] P. Saxena. *Numerical and Experimental Studies of Ethanol Flames and Autoignition Theory for Higher Alkanes.* Ph.d thesis, University of California at San Diego, Department of Mechanical and Aerospace Engineering, 2007.

[28] The San Diego Mechanism. http://combustion.ucsd.edu/, 2009.

[29] P. Saxena and F. A. Williams. Testing a small detailed chemical-kinetic mechanism for the combustion of hydrogen and carbon monoxide. *Combustion and Flame*, 145:316–323, 2006.

[30] S. C. Li and F. A. Williams. NO_x formation in two-stage methane-air flames. *Combustion and Flame*, 118:399–411, 1999.

[31] T. Shimizu, F. A. Williams, and A. Frassoldati. Concentrations of nitric oxide in laminar counterflow methane/air diffusion flames. *Journal of Propulsion and Power*, 21:1019–1028, 2005.

[32] M. M. Y. Waly, S. C. Li, and F. A. Williams. Experimental and numerical studies of two-stage ethane-air flames. *Journal of Engineering for Gas Turbines and Power*, 122(4):651–658, 2000.

[33] M. M. Y. Waly, S. C. Li, and F. A. Williams. Structures of non-sooting counterflow diluted acetylene-air flames. *Proceedings of the Combustion Institute*, 28:2005–2012, 2000.

[34] M. V. Petrova and F. A. Williams. A small detailed chemical-kinetic mechanism for hydrocarbon combustion. *Combustion and Flame*, 144:526–544, 2006.

[35] S. C. Li and F. A. Williams. Experimental and numerical studies of two-stage methanol flames. *Proceedings of the Combustion Institute*, 26:1017–1024, 1996.

[36] S. C. Li and F. A. Williams. NO_x, CH_4, and c_2 species in laminar methanol flames. *Proceedings of the Combustion Institute*, 27:485–493, 1998.

[37] R. Seiser, K. Seshadri, and F. A. Williams. Detailed and reduced chemistry for methanol ignition. *Combustion and Flame*, 158:1167–1672, 2011.

[38] P. Saxena and F. A. Williams. Numerical and experimental studies of ethanol flames. *Proceedings of the Combustion Institute*, 31:1149–1156, 2007.

[39] P. Saxena. *Numerical and experimental studies of ethanol flames and autoignition theory for higher alkanes*. Ph.D thesis, University of California at San Diego, Department of Mechanical and Aerospace Engineering, La Jolla, CA 92093, 2007.

[40] A. Cuoci, A. Frassoldati, T. Faravelli, and E. Ranzi. Frequency response of counterflow diffusion flames to strain rate harmonic oscillations. *Combustion Science and Technology*, 180(5):767–784, 2008.

[41] A. Cuoci, A. Frassoldati, T. Faravelli, and E. Ranzi. Soot formation in unsteady counterflow diffusion flames. *Proceedings of the Combustion Institute*, 32:1335–1342, 2008.

[42] R. J. Kee, F. M. Rupley, J. A. Miller, M. E. Coltrin, J. F. Grcar, E. Meeks, H. K. Moffat, A. E. Lutz, G. Dixon-Lewis, M. D. Smooke, J. Warnatz, G. H. Evans, R. S. Larson, R. E. Mitchell, L. R. Petzold, W. C. Reynolds, M. Caracotsios, W. E. Stewart, P. Glarborg, C. Wang, O. Adigun, W. G. Houf, C. P. Chou, and S. F. Miller. Chemkin collection, release 3.7.1. Technical report, Reaction Design Inc., San Diego, CA, 2003.

[43] A. L. Sánchez, G. Balakrishnan, A. Liñán, and F. A. Williams. Relationships between bifurcation and numerical analysis for ignition of hydrogen-air diffusion flames. *Combustion and Flame*, 105:569–590, 1996.

Chapter 3

Counterflow Diffusion Flames at Elevated Pressures

3.1 Hydrogen

3.1.1 Overview

Hydrogen combustion is of interest, not only because burning it directly in engines is one attractive way to make use of hydrogen as an energy carrier, but also because of safety issues associated with the relative ease with which it can be ignited. Moreover, the oxidation chemistry of hydrogen is essential to the combustion chemistry of all practical fuels, from hydrocarbons through alcohols to carbon monoxide, and possibly more so in applications involving hydrogen addition. For these reasons, the associated chemical kinetics and transport properties have been studied extensively for hydrogen. Many different sources of chemical-kinetic and transport parameters for hydrogen combustion are now available. Experimental tests of predictions derived from these different sets of parameters for various kinds of combustion processes are important for distinguishing between the different predictions and for establishing ranges of uncertainty, thereby possibly ultimately leading to improved values of parameters. New experimental results are reported here that can be used to test predictions of hydrogen combustion.

In significant respects, autoignition and flames constitute two different types of combustion processes for testing predictions. Ignition experiments, as in shock tubes, strive for homogeneous mixtures, so that transport properties are irrelevant, and radicals are not present initially, so that radical generation chemistry strongly affect the results. This

applies also for detonations, as well as for initiation processes such as those in HCCI engines. Flames, on the other hand, are strongly influenced by molecular transport processes, but, since radicals are already present in the hot reaction zones of flames, radical production is less important, leading to differences in the dominant chemical-kinetic steps. In this context, flames include premixed, partially premixed and diffusion flames. The present study concerns diffusion flames, specifically in a counterflow configuration, but the results may be expected to have a bearing on other combustion processes in this second category.

At least 20 shock-tube studies of hydrogen-oxygen ignition processes have been reported, extending back more than 50 years [1]. These studies have spanned a wide range of experimental conditions, with pressures ranging from less than $0.02\,\mathrm{atm}$ [2] to more than $80\,\mathrm{atm}$ [3]. In contrast, the range of conditions of existing experiments with flames is much narrower. Most of the counterflow diffusion-flame experiments, for example, have been performed at $1\,\mathrm{atm}$, although some measurements have been made down to $0.5\,\mathrm{atm}$ [4]. No such measurements have been reported for pressures above 1atm, although hydrogen combustion at elevated pressures is of considerable interest, for example in connection with engine application. In this chapter, a newly developed high-pressure counterflow combustion facility, as descriped in Appendix B, is employed to investigate hydrogen flame structures and extinction conditions at pressures from $1\,\mathrm{atm}$ to $15\,\mathrm{atm}$. Figure B.2 is a schematic illustration of the experimental facility. The experimental results are compared with predictions of different chemical-kinetic mechanisms, to help to assess the uncertainties that may arise at elevated pressures.

3.1.2 Experimental Conditions

Figure A.1(a) is a schematic illustration of the flowfield established in the counterflow configuration for this experimental investigation and a description of the characteristics provided in Section A.1. Fuel mixed with nitrogen is injected from the fuel duct, and air is injected from the oxidizer duct. The distance between the fuel boundary and the oxidizer boundary is $10\,\mathrm{mm}$. Experiments were conducted with $X_{\mathrm{F},1} = 0.14$, $X_{\mathrm{O}_2,2} = 0.21$ and $T_1 = T_2 = 298\,\mathrm{K}$, resulting in a stoichiometric mixture fraction of $Z_{st} = 0.717$, given by Equation A.2. The experiment is designed to conform with self-similar axisymmteric channel flow with plug-flow boundary conditions [5]. In this flow, the value of the strain rate, defined as the normal gradient of the normal component

of the flow velocity, changes from the fuel boundary to the oxidizer boundary. In the absence of the boundary-layer displacement effect of the flame, the characteristic local strain rate on the fuel side of the stagnation plane, a_1, would be given by Equation A.1 is obtained from an asymptotic analysis in which the Reynolds numbers of the laminar flow at the boundaries are presumed to be large [5].

In the present experiments, these Reynolds numbers ranged from 200 to 2800. This equation, or, alternatively, the corresponding equation for the oxidizer-side strain rate, involves only known, experimentally adjustable quantities and therefore provides a convenient basis for comparison of experimental and computational results, irrespective of the strength of the boundary-layer effects, which are appreciable. With the momentum balance given by $\rho_1 V_1{}^2 = \rho_2 V_2{}^2$, the strain rate as given in Equation A.1 becomes $a_1 = 4V_1/L$. The accuracies of the measured values of the volumetric flow rates are expected to be better than $\pm 1\,\%$. The velocities of the reactants at the duct exits, V_1 and V_2, are calculated as the ratio of the measured volumetric flow rates of the reactants and the cross-sectional area of the ducts. A detailed description of the experimental facility employed in this study is provided in Chapter B and the burner configuration is similar to the one described in Section A.1.1. The thermocouple employed for temperature measurements is a R-type thermcouple with a wire diameter of 75 microns and a bead size of 150 microns. A hafnia coating was applied to the thermocouple to prevent catalytic surface reactions. Measured temperatures were corrected taking into consideration the radiative heat losses from the thermocouple surface.

3.1.3   Temperature Profiles

Figure 3.1 compares measured and predicted temperature profiles at four different elevated pressures. The computations employed the San Diego mechanism along with the associated thermodynamic and transport data that can be downloaded from the web [6]. They were performed using the computer program OpenSMOKE, developed in Milan [7, 8]. The code employs mixture-averaged diffusion coefficients for various species and includes radiative heat loss and thermal (Soret) diffusion. The Soret effect is especially important for calculations involving atomic and molecular hydrogen in highly diluted hydrogen flames. This effect enhances the diffusion of H and H_2 into the reaction zone, thus impacting predicted flame structures and extinction limits significantly. Discretization of differential equations is carried out using conventional finite-differencing
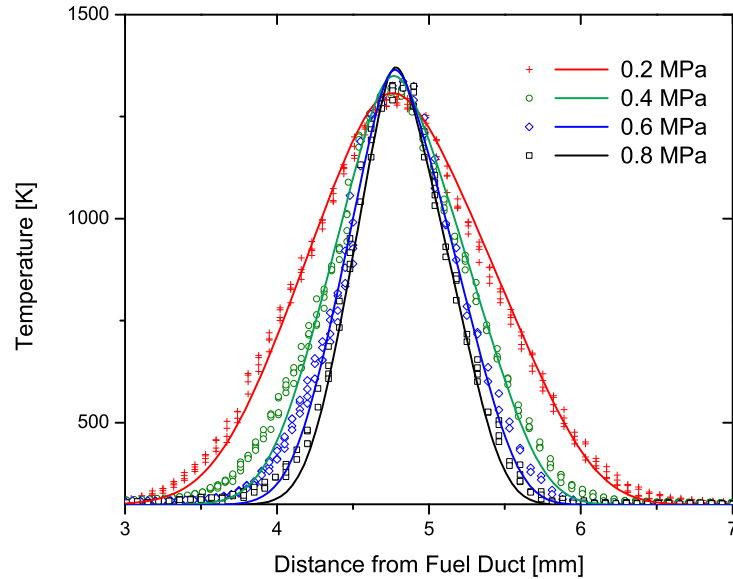
Figure 3.1: Profiles of temperature as a function of distance from the fuel boundary at pressures, p, of 0.2, 0.4, 0.6 and 0.8 MPa. The strain rate is $a_1 = 100\,1/s$, and the stoichiometric mixture fraction is $Z_{St} = 0.717$ The figure shows temperature profiles corrected for radiative heat losses. The symbols represent experimental data, and the solid curves represent predictions obtained using the San Diego mechanism.

techniques for non-uniform mesh spacing. Increasing pressure reduces the thickness of the thermal mixing layer of a strained diffusion flame. To account for the resulting strong gradients within the computational domain, dynamical adaptive meshing techniques are used. Standard calculations employ 300 grid points. Details of the computational procedure used to obtain the critical conditions of extinction have been described previously [9]. Figure 3.1 exhibits good general agreement between the measurements and predictions. As is expected from the value of the stoichiometric mixture fraction being greater than 0.5, the peak temperature occurs on the fuel side of the mid point between the two duct exits, at a distance less than 5 mm from the fuel boundary. The predictions and measurements are in excellent agreement in regions where the temperature profiles are nearly linear. In such regions, the finite size of the thermocouple has relatively little effect on the measurements because contributions from higher and lower temperatures tend to cancel. In regions of high curvature, however, those cancellations do not occur, and the experimental temperature profile tends to be smoothed. This effect can be seen
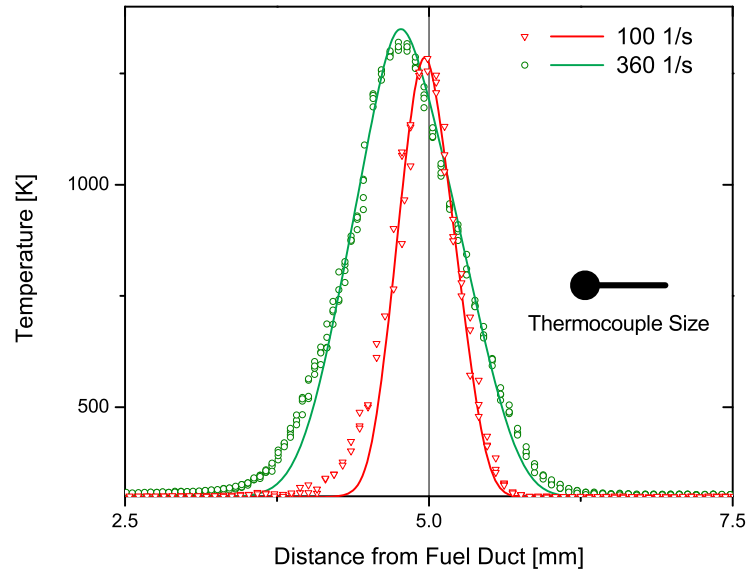
Figure 3.2: Profiles of temperature as a function of distance from the fuel boundary at a pressure, p, of $0.4\,\mathrm{MPa}$, for strain rates $a_1 = 100\ 1/s$ and $a_1 = 360\ 1/s$. The figure shows temperature profiles corrected for radiative heat losses. The symbols represent experimental data, and the solid curves represent predictions obtained using the San Diego mechanism.

near the peak temperature and on each side near the boundary temperature in the figure. It is thus concluded that, within the accuracy with which these temperature measurements can be made, experiment and computation are in agreement. This conclusion is further emphasized in Figure 3.2, which illustrates the wire and bead sizes and shows a comparison of flames at $0.4\,\mathrm{MPa}$, one for $a_1 = 100\ 1/s$ and one for $a_1 = 360\,1/s$, just below the value at extinction. The departures from predictions near the fuel boundary are clearly seen here to exceed those near the oxidizer boundary, the higher thermal conductivity of the gas there effectively enlarging the region of influence of the finite size of the thermocouple by enhancing heat-flow contributions farther from the center of the bead. This figure also demonstrates how increasing the strain rate decreases the peak temperature, thins the profile, and moves its location closer to the stagnation plane, as expected.

In Figure 3.3 the maximum temperature of the reaction zone just before extinction is shown for a pressure range from 0.2 to $0.8\,\mathrm{MPa}$. These measurements were
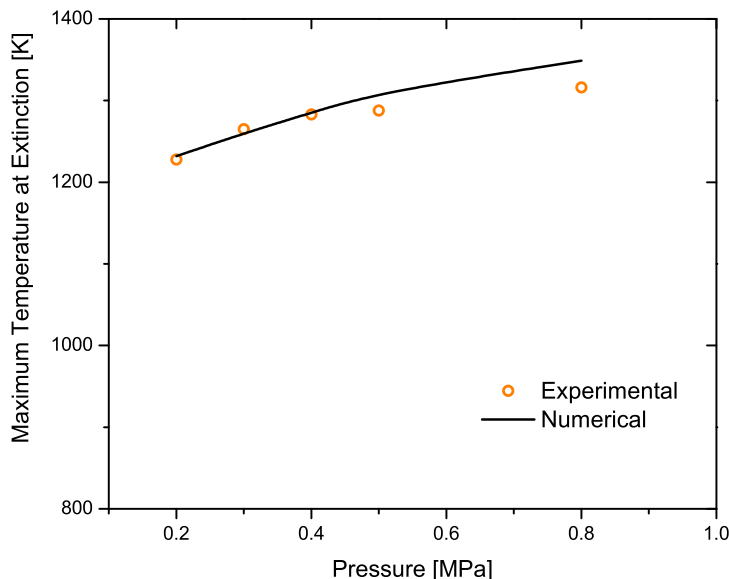
Figure 3.3: The maximum temperature just before extinction. The symbols represent experimental data and the solid curve represents predictions obtained using the San Diego mechanism.

made at a strain rate equal to 90% of the experimental strain rate at extinction. Experimental measurements (symbols) indicate an increase in peak temperature with an increase in pressure, as well as a flattening trend that is also predicted by the numerical computations. The quantitative agreement between experimental measurements and numerically derived values is excellent up to a pressure of $0.4\,\mathrm{MPa}$. Above $0.4\,\mathrm{MPa}$ the calculations predict higher flame temperatures at extinction than are measured, as may be expected from the thinning of the flame with increasing pressure, leading to increasing influences of the curvature of the temperature profile on the measurement, which will decrease the recorded temperature, as may be inferred from Figure 3.2. All of the observed differences between the measurement and the prediction can thus be attributed to measurement difficulties with thermocouples. Because of the significant influence of transport properties on temperature profiles, these results thus support the validity of the transport properties employed, within experimental error. Although temperature profiles are considerably less sensitive to detailed chemical-kinetic descriptions than are profiles of concentrations of chemical species, these results also suggest that there are no gross errors in the chemistry at these elevated pressures.

3.1.4   Extinction Conditions

In comparison with temperature profiles, diffusion-flame extinction conditions are much more sensitive to the chemical-kinetic descriptions. The general character of the pressure dependence of the counterflow diffusion-flame strain rate at extinction is known from earlier work. For example, as illustrated in Figure 3.4, as the pressure increases, the extinction strain rate at first increases, reaches a maximum, then decreases, reaches a minimum, then begins to increase again. The reason for this type of behavior is explained by Sohn and Chung [10]. The present experiments do not extend to high enough pressures to reach the minimum of the curve, which occurs at pressures so high that they are mainly of interest only in rocket-propulsion applications. To provide a general indication of the type of agreement of the present experimental results with such predictions, the data obtained in the present study also are plotted in this figure. While both results pertain to the oxidizer-side strain rate, the computation employed potential-flow boundary conditions, while the preceding plug-flow formula is employed for the experiments. Quantitative comparisons therefore should not be expected. It can be observed that both results exhibit a maximum in the curve, at roughly the same value of pressure for the same composition, and that their shapes are in general agreement. No conclusion beyond that, however, can be drawn from the comparison.

Figure 3.5 shows the measured strain rate at extinction, $a_{1,\mathrm{E}}$ as a function of pressure, p, at fixed $X_{\mathrm{F},1} = 0.14$, now on a linear rather than logarithmic pressure scale. The solid curve represents predictions obtained using the San Diego mechanism [6] and the dashed curve is obtained from the GRI mechanism [11]. Predictions of this last, well-known mechanism are shown only to illustrate that the general range of variation of predictions of different mechanisms is substantial for these extinction strain rates. The two curves shown approximately represent extremes; predictions of most other mechanisms lie between them, for the most part. See [12] for a recent re-evaluation of the hydrogen combustion chemistry.

A shaded area is provided around the experimental data to indicate the range of experimental uncertainty. The area is much wider than experimental uncertainties in measurements of pressure or of flow rates employed to calculate strain rates. The accuracy of the measured values of the volumetric flow rates, for example, is expected to be better than $\pm 1\,\%$. Instead, extremes in the compositions of the feed streams, subject to possible experimental errors, were employed in the San Diego mechanism to calculate
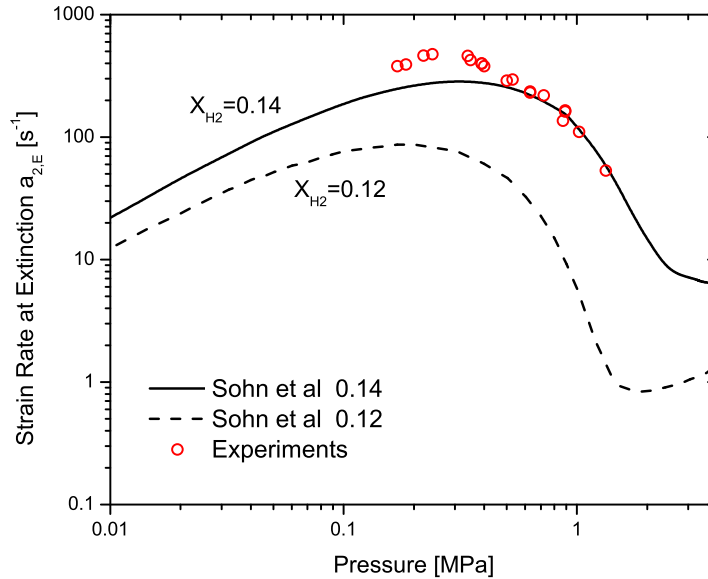
Figure 3.4: The strain rate at extinction, $a_{2,E}$, for hydrogen-air diffusion flames as a function of pressure, p, at $X_{F,1} = 0.14$ and at $X_{F,1} = 0.12$, as calculated by Sohn and Chung (2000). Also shown for comparison are symbols representing experimental data reproduced from Figure 3.5.

limiting strain-rate curves bounding the San Diego prediction, and those bounds were then lowered to bound the experimental data. In this way the shaded area provides an indication of the range of predictions that may be expected for any mechanism, subject to uncertainties in feed-stream compositions. The area narrows as the pressure increases because the uncertainties in the feed-stream compositions decrease. The boundaries of the area were calculated by adding the numerically derived limits to the averaged experimental data points.

It is worth pointing out that, for the conditions investigated here, the hydrogen flame is not visible, but the shadow established from its density gradients can be clearly seen. Extinction was considered to take place when this shadow suddenly disappeared. Further confirmation of extinction was provided by the observation that a rapid decrease in the exhaust-gas temperature followed immediately.

The figure shows excellent agreement between the measurements and the San Diego predictions from normal atmospheric pressure up to 0.25 MPa., well within the experimental uncertainty. This is understandable because of the previous tests of the
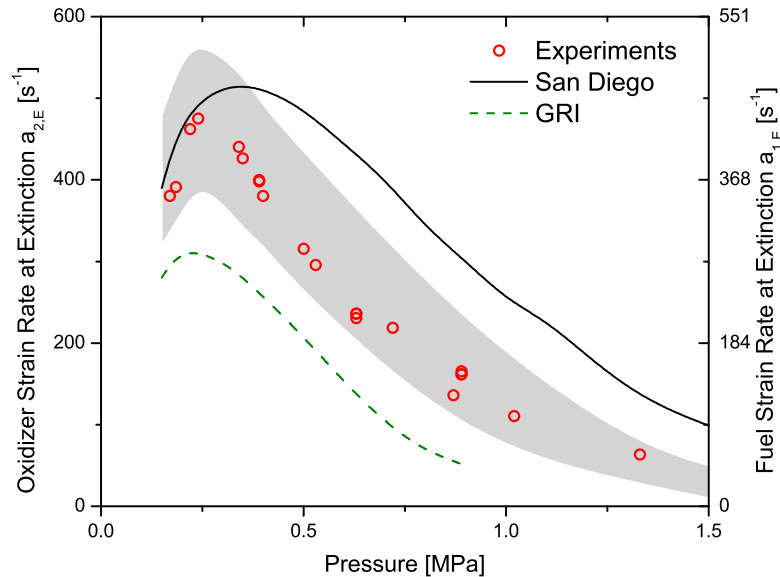
Figure 3.5: The strain rate at extinction, $a_{2,\mathrm{E}}$, for hydrogen flames as a function of pressure, p, at $X_{\mathrm{F},1} = 0.14$. The symbols represent experimental data, the solid curve represents predictions obtained using the San Diego mechanism [6], and the dashed curve represents predictions obtained from the GRI mechanism [11].

mechanism at $0.1\,\mathrm{MPa}$. At higher pressures, however, the predictions begin to fall well above the area of experimental uncertainty. The experimental data show that the highest value of $a_{1,\mathrm{E}}$ is attained around $0.3\,\mathrm{MPa}$, while the mechanism instead predicts the maximum around $0.4\,\mathrm{MPa}$. And differences increase beyond that pressure. The more recent mechanism of [12] predicts oxidizer strain rates at extinction which are lower than those of the San Diego mechanism by $20\,1/s$ to $50\,1/s$, with a maximum at a slightly higher pressure, but above $0.5\,\mathrm{MPa}$ these also lie above the shaded area.

Sensitivity analysis, for example, shows those elementary reactions that give the highest values for the sensitivity coefficient with respect to T, given by the maximum value of $\partial \ln T / \partial \ln A_k$, (where A_k is the frequency factor of reaction k), as expected, are those of the chain-branching reaction $H + O_2 \rightleftharpoons O + OH$, and of the recombination step $H + O_2 + M \rightleftharpoons HO_2 + M$. The lower prediction of the mechanism of [12] may arise from the fact that their rate for the first of these steps is somewhat lower in this temperature range. It was observed that, if the chaperon efficiency for nitrogen for the latter of these steps is doubled, then the predictions of the San Diego mechanism fall right on top of the

data, at all pressures tested. Such a change, however, significantly degrades agreement of predictions [1] of shock-tube ignition experiments at the lower temperatures. Therefore, at present, revisions to the mechanism are not recommended. Instead, it is simply cautioned that differences like those seen in the figure for extinction predictions should be anticipated at these elevated pressures.

3.2 Hydrocarbons

3.2.1 Overview

The ability of chemical-kinetic mechanisms and transport descriptions to predict combustion processes is tested most easily and accurately by well-controlled laboratory experiments performed at normal atmospheric pressures, where measurements of strain rates at extinction, in particular, provide relevant tests of chemical-kinetic descriptions. In many practical applications, however, the combustion occurs at elevated pressures. Since the combustion chemistry varies with pressure, often non-monotonically in certain respects, it is desirable to pursue correspondingly well-controlled laboratory combustion experiments at pressures above atmospheric, as further tests of predictions. But such experiments, unfortunately, are difficult and expensive to design and perform. A newly developed high-pressure counterflow combustion facility, as described in Appendix B, is employed to investigate laminar counterflow diffusion flames. Results of these experiments with hydrogen as the fuel have been published [13] and can be found in Section 3.1. In this chapter we report and discuss corresponding results for methane, ethane, and ethylene, as well as showing the effects of different reaction rates on comparisons between predictions and measurements for all of the fuels tested.

There have been a number of previous high-pressure counterflow experimental studies. Niemann et al [13] recently carried out experiments on hydrogen flames at pressures up to $1.5\,MPa$, measuring temperature profiles and providing experimental confirmation for the non-monotonic pressure dependence of extinction strain rates predicted computationally by Sohn and Chung [14]. In addition, Figura and Gomez [15] successfully stabilized nonpremixed methane flames at elevated pressures up to $3.0\,MPa$. Their experiments were conducted with the fuel and oxidizer streams diluted with either nitrogen or helium. Temperature profiles were measured and compared with predictions [15], but extinction strain rates were not addressed. On the other hand, Maruta et al. [16] earlier had measured critical conditions for extinction of nonpremixed methane flames with the fuel and oxidizer streams diluted with carbon dioxide (CO_2) and with nitrogen at pressure up to $0.8\,MPa$. They found that for flames diluted with CO_2, critical conditions for extinction were influenced by radiation re-absorption, but they did not specifically discuss variations of the extinction strain rates with pressure. Böhm and Lacas [17] also measured critical conditions for extinction of nonpremixed methane flames

up to pressures of 0.6 MPa. Their emphasis was on soot formation and destruction, but they did demonstrate experimentally that with increasing pressure, the measured strain rate at extinction first increased and then decreased. Their computations with detailed chemistry also showed an increase in the value of the strain rate at extinction with increasing pressure followed by a decrease, but the decrease was less pronounced than that measured [17].

Much earlier than these investigations, Sato [18] had measured critical conditions for extinction of nonpremixed methane and ethane flames at pressures up to 10 MPa. These measurements were made on flames stabilized over the surface of a porous cylinder (a Tsuji burner), and they showed that with increasing pressure, the strain rates at extinction for methane and ethane remained constant for pressures up to 2.0 MPa and 1.0 MPa, respectively, but with further increase in pressure, up to 10 MPa, the strain rate at extinction decreased [18]. This qualitatively different behavior at the lower pressures may be associated with the fact that the fuels in these experiments were not diluted, resulting in strain rates at extinction that were quite appreciably higher. There also have been experiments on liquid-fuel flame extinction in stagnation-point flows of alkanes, performed at about the same time, at pressures up to 2.0 MPa [19, 20] that show regions of increasing extinction strain rates, leading up to a plateauing peak region, followed by a downward-sloping region as pressure is increased, qualitatively similar to the results with diluted methane. In the present work critical conditions for extinction and flame-temperature profiles are determined for an appreciably wider range of gaseous-fuel parameters than is available in this literature.

3.2.2 Experimental Conditions

Figure A.1(a) is a schematic illustration of the counterflow configuration. Fuel (CH_4, C_2H_4, C_2H_6) mixed with an inert gas (N_2, He) is injected from the fuel duct and an oxygen-inert mixture is injected from the oxidizer duct. The reactant streams flow toward a stagnation plane. The momenta of the two streams are balanced to maintain the stagnation plane at the center of the two boundaries. The mass fraction of the fuel, the temperature, and the component of the flow velocity normal to the stagnation plane at the fuel boundary are denoted by $Y_{F,1}$, T_1 and V_1, respectively, this same notation with the subscript 2 being employed for quantities at the oxidzer boundary. The experiment is designed to conform with self-similar axisymmteric channel flow with

plug-flow boundary conditions [5]. In this flow, the value of the strain rate, defined as the normal gradient of the normal component of the flow velocity, changes from the fuel boundary to the oxidizer boundary. In the absence of the boundary-layer displacement effect of the flame, the characteristic local strain rate on the fuel side of the stagnation plane, a_1, would be given by Equation A.1 is obtained from an asymptotic analysis in which the Reynolds numbers of the laminar flow at the boundaries are presumed to be large [5]. The distance between the fuel boundary and the oxidizer boundary , denoted by L, is 10 mm in these experiments. The momentum balance imposed experimentally gives $\rho_1 V_1{}^2 = \rho_2 V_2{}^2$, which when substitued in Equation 2.15 results in $a_2 = 4V_2/L$.

Critical conditions for extinction in these experiments depend on the six quantities $Y_{F,1}$, T_1, $Y_{O_2,2}$, T_2, a_2, and pressure p. The strain rate, a_2, is determined by V_2 given the momentum balance. The main experiments were conducted with air as the oxidizer, $Y_{O_2,2}$=0.233, and inlets at room temperature $T_1 = T_2 = 298$ K. Therefore, at any given value of $Y_{F,1}$, a_2 will depend only on p. The fuel mass fractions selected in these experiments were $Y_{F,1}$=0.16 for methane, $Y_{F,1} = 0.12$ for ethane, and $Y_{F,1}= 0.09$ for ethylene. These conditions result in stoichiometric mixture fractions of Z_{st}=0.267 for methane, Z_{st}=0.342 for ethane and Z_{st}=0.428 for ethylene, given by Equation A.2, where ν is the stoichiometric oxygen-to-fuel mass ratio. The resulting values of the stoichiometric mixture fraction indicate that the flame will be located on the oxidizer side of the stagnation plane. In addition to measuring the extinction value $a_{2,E}$ as a function of p for fixed $Y_{F,1}$, for methane at two different pressures, $a_{2,E}$ was measured as a function $Y_{F,1}$. The reported temperature profiles were measured at a fixed value of the strain rate $a_2= 120$ s^{-1} and for various values of pressures. For flames of all fuels at the conditions investigated here, no visible soot formation was observed.

Figure B.2 is a schematic illustration of the experimental facility. It shows the pressure chamber, the gas-supply system, and the data-acquisition and control system. The counterflow burner is placed inside the chamber. Figure 3.6 shows a photograph of a diluted ethane-air counterflow diffusion flame stabilized in this new high-pressure experimental facility.

Temperature profiles are measured using two Pt-Pt 13%Rh thermocouples. One of the thermocouples employed had a wire diameter of 75 μm and a torch-welded spherical bead with a size of 180 μm, and a second one had a 25 μm spot-welded cylindrical junction. The results reported here were obtained with the smaller one, the larger one
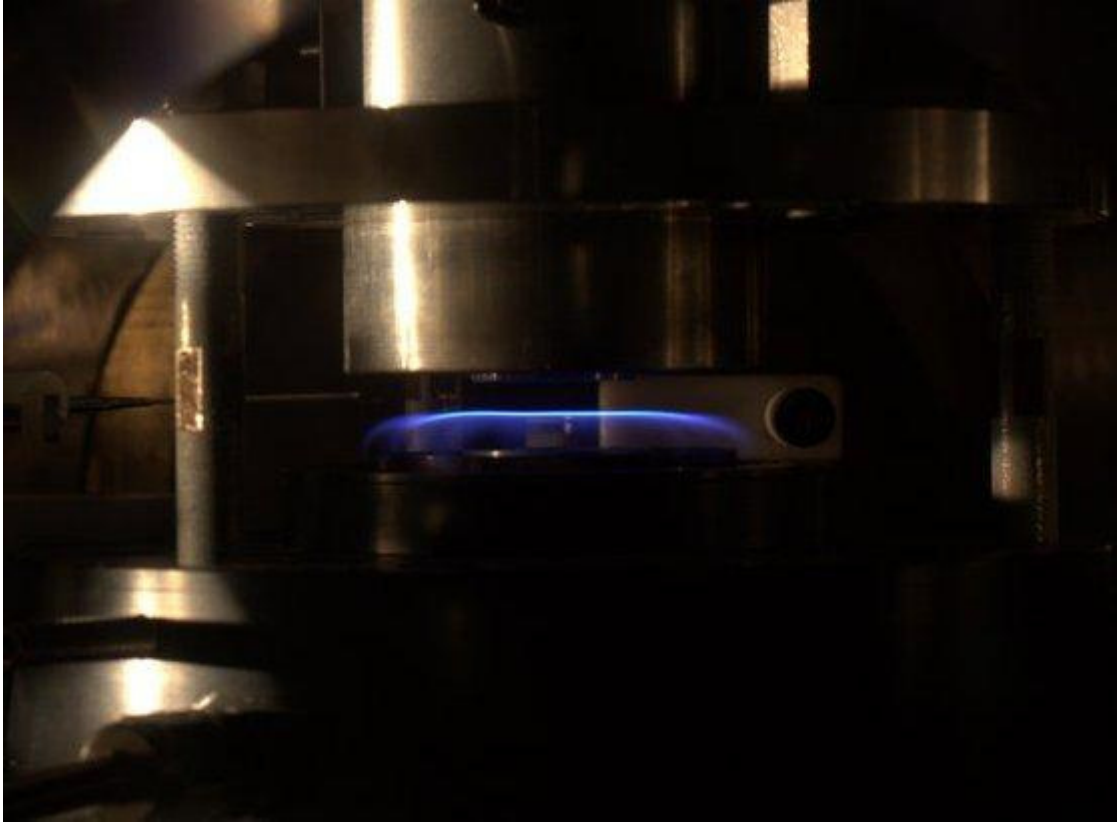
Figure 3.6: Photograph of an nonpremixed ethane-air flame with a fuel mass fraction $Y_{F,1} = 0.14$ at $0.8\,\text{MPa}$.

being used in estimating corrections. The thermocouple was mounted on an XY-stage that is controlled by stepper motors inside the pressure chamber. The probe is programmed to move vertically at a radial distance of $3\,\text{mm}$ from the axis of symmetry to minimize flow-field perturbations. The flame is approached from the bottom (fuel duct), covering a total traverse distance of $7\,\text{mm}$.

The experimental accuracies of the flow velocities, the reactant mass fractions and the pressure are $\pm\,1\,\%$, $\pm\,3\,\%$ and $\pm\,1\,\%$ of the recorded value, respectively. Experimental repeatability of the strain rate at extinction is within $\pm\,2\,\%$ of the recorded value. For the burner used in this study, the deviation of the established flowfield from pure plug flow, resulting in a lower strain rate, can be estimated to be within 10%.

3.2.3   Computational Approach

In investigating ranges of variations of predictions of different chemical-kinetic and transport descriptions for these experiments, the commercial computer code ChemkinPro [21] was excercised with the aforementioned plug-flow boundary conditions for two different schemes, the San Diego mechanism [6] and the USC II mechanism [22], hereafter identified simply as USC. The differences in these two sets of predictions are comparable with differences encountered in computations with other descriptions, as was verified by a few additional calculations. The USC mechanism was selected for further study along with the San Diego mechanism because of its excellent initial agreement with the present high-pressure methane extinction data. Differences in the description were maximized in that the USC mechanism was employed along with its relatively newly developed transport description, while the San Diego mechanism was used with the much older Chemkin mixture-averaged transport. Transport descriptions were observed to be relevant in that, for example, computations with the San Diego mechanism using the Chemkin multicomponent diffusion description introduced differences, always lowering the predicted extinction strain rates, comparable with differences of the predictions of the two chemical-kinetic mechanisms. All of the reported results included both Soret diffusion and radiant loss, the latter always found to be of lesser importance, but the former being non-negligible, although not to the extent of the differences between mixture-averaged and multicomponent transport. Interpretations of results and conclusions concerning effects of different values for chemical-kinetic rate parameters must thus be tempered by these underlying uncertainties in the transport description.

Some of the initial computations were made with the code OpenSMOKE [7, 8], but later only ChemkinPro was used because of its multicomponent-diffusion option. Results obtained with the two different codes were in agreement, supporting code-independence. Computational tests always were made to assure sufficient spatial resolution that predictions were independent of grid size. This is especially important at increased pressures because of the associated reduced thickness of the flame. To account for the resulting strong gradients within the computational domain, adaptive meshing techniques were used. The resulting non-uniformly spaced grids of up to 300 points were found to resolve the reaction zone sufficiently.
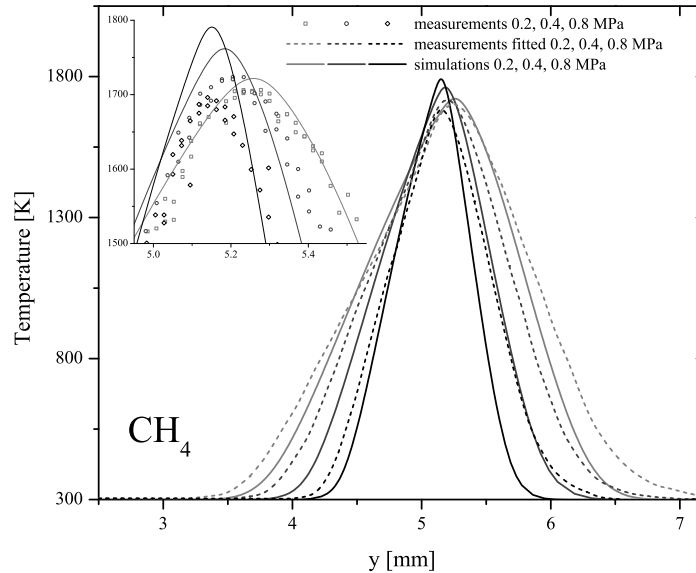
Figure 3.7: Profiles of temperature as a function of distance from the fuel boundary for methane diffusion flames at fixed $Y_{F,1} = 0.16$ at 0.2, 0.4, and 0.8 MPa. The strain rate is $a_2 = 120\,\mathrm{s}^{-1}$, and the stoichiometric mixture fraction is $Z_{st} = 0.267$. Solid [——]curves are obtained computationally using San Diego mechanism with mixture-averaged diffusion. In the main plot, experimental data are represented by dashed [- - -] curves as a best fit, and the actual data points around the temperature peak are shown in the subplot.

3.2.4 Temperature Profiles

Temperature profiles are shown in Figure 3.7 for methane flames and in Figure 3.8 for ethane flames at values of pressures of 0.2, 0.4 and 0.8 MPa and fixed $a_2 = 120\,\mathrm{s}^{-1}$. Standard radiation corrections [23] were employed, and catalytic effects were estimated to be negligible. Unlike extinction strain rates, the computational results in these papers are only weakly dependent upon the chemical-kinetic and transport descriptions, except very near the peak temperature. The profiles show that the gradients of temperature with respect to the spatial coordinate are zero at the oxidizer and fuel boundaries. The flames are therefore considered to be without heat loss to the nozzles. While exhibiting generally good agreement between measurements and predictions, measured temperature profiles are noticeably wider. For CH_4 the width is in average 12% higher and for C_2H_6 15%higher than the computed profiles, percentages that tend to increase with pressure.
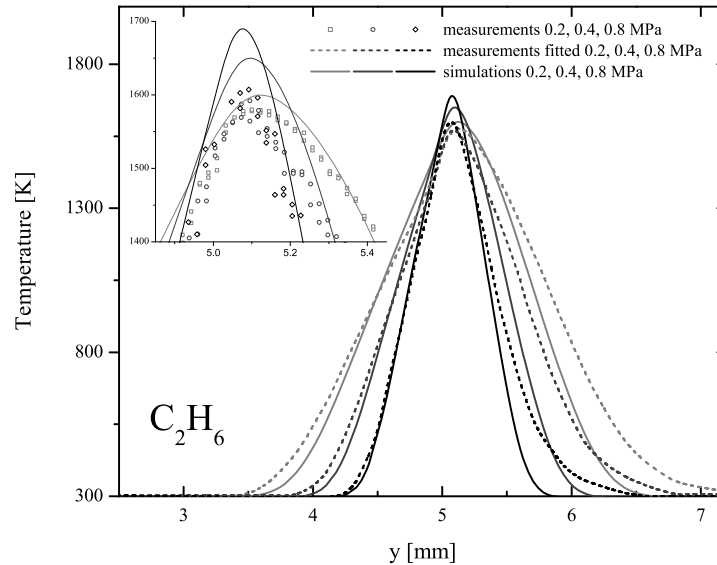
Figure 3.8: Profiles of temperature as a function of distance from the fuel boundary for ethane diffusion flames at fixed $Y_{F,1} = 0.14$ at at 0.2, 0.4 and 0.8 MPa. The strain rate is $a_2 = 120\,\mathrm{s}^{-1}$, and the stoichiometric mixture fraction is $Z_{st} = 0.302$. Solid [———] curves are obtained computationally using San Diego mechanism with multi-component diffusion. In the main plot, experimental data are represented by dashed [- - -] curves as a best fit, and the actual data points around the temperature peak are shown in the subplot.

The finite size of the thermocouple causes the profiles to be smoothed in regions of high curvature, such as at the peak and near the flame boundaries. This effect, however, is expected to cancel for points in regions of linear temperature gradients. Hence it does not provide a reasonable explanation for the widened profiles.

The possible effects of absorption of flame radiation by the thermocouple wires are not included in the standard radiation corrections and have not been discussed in the literature for measurements of the present kind in the counterflow configuration. Flame radiation absorbed by the wires can heat them above the local gas temperature, causing the thermocouple temperature reading to be too high. Equating the radiant heat input rate to the wire to the product of the temperature difference between the wire and the gas, the wire surface area and the convective/conductive heat-transfer coefficient of the surrounding gas provides an estimate of the temperature increase of the thermocouple measurement associated with this effect. The first step in making such estimates is to

calculate the radiant heat flux from the flame.

These counterflow-flame hot zones are quite accurately optically thin, and they radiate predominantely in CO_2 and H_2O bands. Planck-mean absorption coefficients for these bands, obtained from the ploynomial fits of RADCAL [24, 25], were employed along with the calculated profiles of partial pressures of CO_2 and H_2O and of temperature from the San Diego mechanism to obtain the radiant fluxes from three of our counterflow flames. The results are shown in Figure 3.9, where ethane lies below methane partially because of the greater degree of dilution of the fuel, and hydrogen lies well below the other two partially because of the absence of the CO_2 bands, consistent with measurements [13] not exhibiting significant widening for this fuel. These results are only estimates, but the values are of an order of magnitude that is consistent with the radiant-loss corrections available in Chemkin and OpenSmoke, which are somewhat lower, sometimes as much as a factor of two, but not more than that. The curves in Figure 3.9 increase with pressure approximately in proportion to $p^{\frac{2}{3}}$, which may be compared with the estimated [26] $p^{\frac{1}{2}}$ increase of the heat-release rates in counterflow flames, the difference likely associated with relative increases in temperature and CO_2 and H_2O mole fractions.

Heat-transfer coefficients are dominated largely by the thermal conductivity of the gas, which increases with temperature. If the results in Figure 3.9 are employed in the energy balance, with an emissivity (equal to absorptivity) of the platinum wire of 0.2 [27] then the heat-transfer coefficient in the flame is found to be high enough that the absorption of the flame radiation would increase the measured temperature by a few K at the most when the thermocouple is in the hot zone. When the thermocouple is outside the radiating region of the flame, its view factor is 0.5, and so it absorbs only about ten precent of the radiant flux, but the lower thermal conductivity of the gas at such locations results in an estimated thermocouple temperature increase by a substantial amount, which increases rapidly with increasing distance from the flame, approaching as much as 300 K in the cold flows at the inlet boundaries. In an order-of-magnitude sense, this is consistent with the measured widening of the profiles in Figures 3.7 and 3.8, but it certainly is not consistent with the observation that the measurements approach 300 K rather than 600 K at the vertical-distance values of 3 mm and 7 mm in these figures.

Although the uncertainties in these estimates are large, an inescapable conclusion is that if all of the flame radiation were incident upon the thermocouple wires in the colder regions of the flow, then the measured thermocouple temperature would be

quite appreciably higher than the local gas temperature. The flame radiation therefore must be reabsorbed by the gas before reaching the colder regions. The CO_2 and H_2O absorptivities do in fact increase substantially with decreasing temperature, so that re-absorption of the flame radiation by the gas can reduce the outward radiant flux to such an extent that its influence on the thermocouple readings becomes negligible. This reabsorption is estimated to occur mainly at temperatures below $800\,K$. The fuels CH_4 and C_2H_6 also have infrared absorption bands that can absorb flame radiation, and that is consistent with the observation in Figures 3.7 and 3.8 that the experimental widening is greater on the air side than on the fuel side. The widening thus is attributed here to influences of the flame radiation and its transport.

An implication of these observations is that it may be more accurate for some purposes to exercise flame codes without radiant loss included, although, as previously indicated, that effect is very small in the computations for the present flames. Accurate analyses of the thermocouple readings would be difficult to develop because they would require detailed computation of radiation transport, which are challenging and have many uncertainties. Such radiation-transport effects, however, besides influencing measurements with addition of carbon dioxide, as indicated by Maruta et al. [16] , also likely affect the thermocouple measurements of Figura and Gomez [15].

As indicated by the previously stated values of the stoichiometric mixture fractions, the peak temperatures are expected to lie on the oxidizer side of the stagnation plane, which is located at y=5 mm in Figures 3.7 and 3.8, corresponding to Z_{st}=0.5. This is indeed seen to be true in these figures, and, moreover, as pressure is increased, narrowing the flame, the peaks move closer to the stagnation plane. It is of interest to investigate whether a scaling can be identified that will collapse these temperature profiles. According to Burke-Schumann theory, counterflow diffusion-flame length scales are proportional to the square root of the ratio of a diffusivity to the strain rate [28], which is proportional to $1/\sqrt{pa}$. Hence if x denotes the distance from the obeserved position of peak temperature, scaled temperature profiles should collapse when plotted against $\xi = x \cdot \sqrt{\frac{p \cdot a}{p_{ref} \cdot a_{ref}}}$, where p_{ref} and a_{ref} are arbitrary reference values, and x is in mm. The selections p_{ref}=0.1 MPa and a_{ref}=120 s^{-1} are made here, and the nondimensional temperature is defined as $\theta = \frac{T - T_{min}}{T_{max} - T_{min}}$, where T_{max}, is the observed peak temperature and T_{min} is the feed temperature.

Figure 3.10 shows these plots, demonstrating good scalability for the flames in-
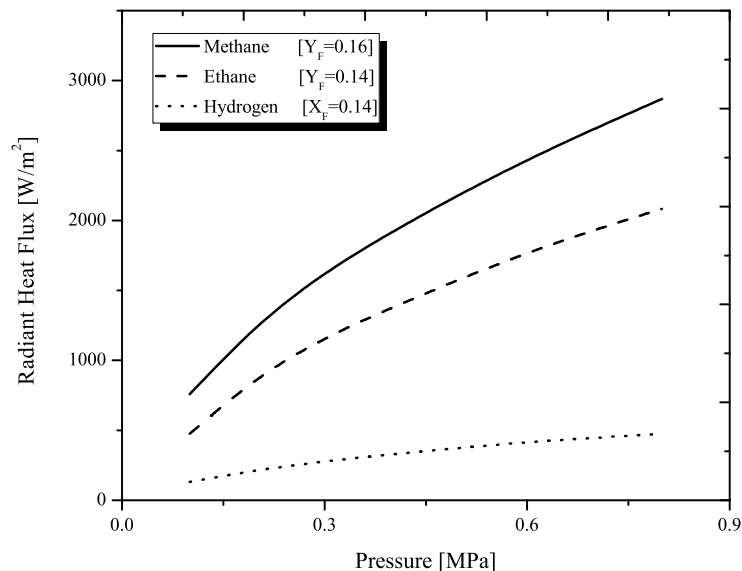
Figure 3.9: Calculated values of radiative heat flux from the flame as a function of pressure for three fuels in the counterflow experiments. [13].

vestigated. The variations, most evident on the oxidizer side, are associated with the fact that radiative heating of the thermocouple, discussed above, does not obey this scaling but rather becomes relatively more prominent with increasing pressure. The computational profiles (not shown) also obey this scaling very well.

The insets in Figures 3.7 and 3.8 show clearly that as pressure increases the measured maximum flame temperature increasingly falls below that calculated. This, of course, is due to the fixed thermocouple size and the thinning of the flame. Figure 3.11 uses the information obtained from temperature profiles measured with two differently sized thermocouples to obtain a better estimate of the actual peak flame temperature. The use of two thermocouples is necessary because even the smallest commercially available R-type thermocouple with a wire diameter of $25\,\mu$m is comparable in size to the reaction-zone width at the higher pressures. The recorded temperature was plotted against the thermocouple diameter on a linear scale and extrapolated to zero diameter. This should produce a slight overestimate of the temperature that could have been improved by a nonlinear extrapolation if measurements with thermocouples of three different sizes were available. R-type thermocouples are generally considered to be accurate
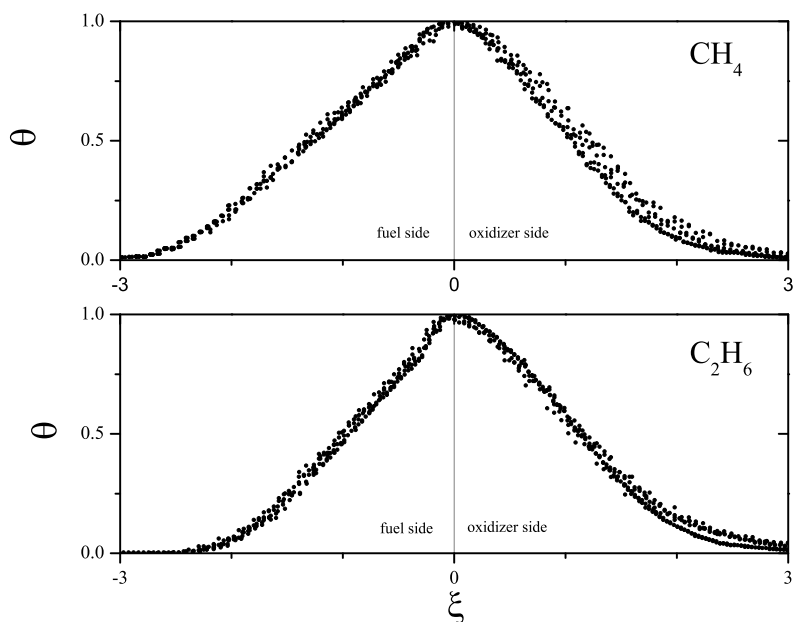
Figure 3.10: Flame temperature measurements are plotted with the reduced temperature, θ, as function of a non-dimensional spatial coordinate, ξ, with the location of the peak temperature as 0.

within $5\,\mathrm{K}$, and the maximum difference between the measured and radiation-corrected temperatures is $25\,\mathrm{K}$ for the smaller and $150\,\mathrm{K}$ for the larger thermocouple for the highest temperatures measured in this study. The repeatability of measurements of the maximum temperature is about $\pm 10\,\mathrm{K}$, better at greater flame thickness. Combining this information, it thus seems reasonable to estimate the accuracy of the temperature measurements conservatively to be within $\pm 15\,\mathrm{K}$ for the small thermocouple and $\pm 40\,\mathrm{K}$ for the large thermocouple in this high-temperature zone. Extrapolating these error margins provides error bars as shown in Figure 3.11. The curves in the figures are the predictions of the San Diego mechanism with mixture-averaged diffusion and of the USC mechanism with multicomponent diffusion. With multicomponent diffusion the prediction of San Diego mechanism are quite close to the other. There thus appears to be reasonable agreement between the predictions and measurements of the peak temperature for both the absolute values and the trends with pressure.
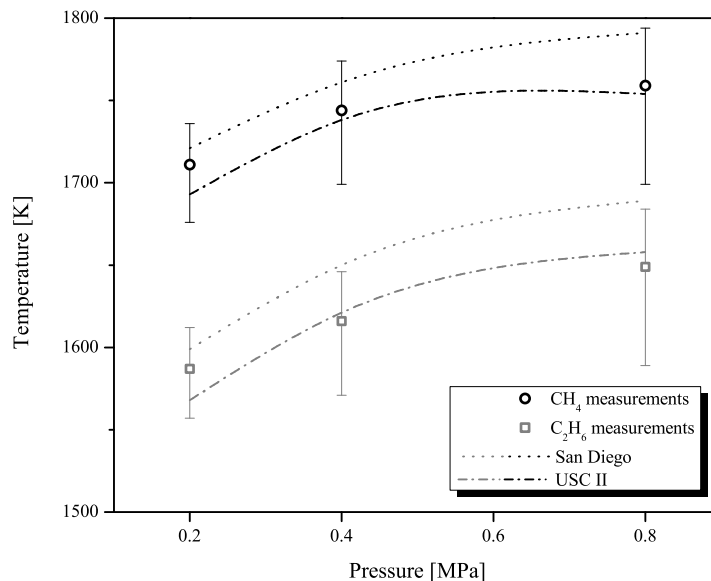
Figure 3.11: The maximum temperatures plotted as a function of pressure for 0.2, 0.4 and 0.8 MPa for both methane (upper) and ethane (lower) diffusion flames at $a_2=$ $120\,s^{-1}$. Open symbols denote extrapolated measurements, while computations are represented by a dotted [·······] curve for San Diego mechanism with mixture-averaged diffusion and a dash-dotted [–·–·–·] curve for USC-mech II.

3.2.5   Extinction Conditions

Extinction conditions of diffusion flames are much more sensitive to the description of chemistry and molecular transport than are temperature profiles. Hence, obtaining reasonable good agreement between temperature profiles and numerical simulations is not a sufficiently conclusive validation for a chemical-kinetic scheme.

This becomes apparent in Figure 3.12 , which shows the strain rate at extinction, $a_{2,\mathrm{E}}$, for diluted methane-air flames as a function of pressure, p, at fixed $Y_{\mathrm{F},1} = 0.16$. With increasing pressure, the strain rate at extinction first increases, attains a maximum value at around 0.3 MPa and then decreases. The agreement of the experimentally determined extinction strain rates with computations using the San Diego mechanism with mixture-averaged diffusion is within experimental accuracy up to about 0.7 MPa, but above this pressure the existing mechanism predicts an essentially constant extinction strain rate, contrary to experiment. Excellent agreement exists, however, between experiment and predictions of USC mechanism up to a pressure of 1.0 MPa. Experimen-
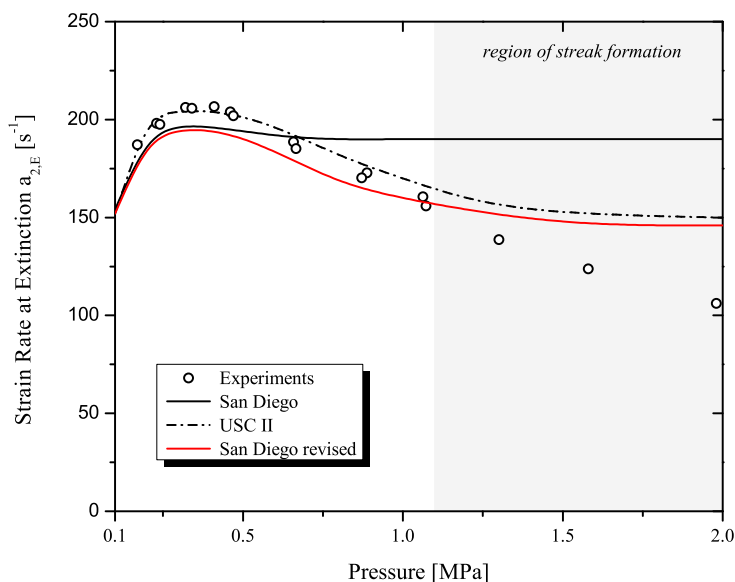
Figure 3.12: Experimentally obtained strain rates at extinction, $a_{2,\mathrm{E}}$ for methane diluted with nitrogen as a function of pressure, p, at fixed $Y_{\mathrm{F},1}= 0.16$. The oxidizer is air. Open symbols represent experimental data, while computations are represented by a solid black [——] curve for San Diego mech with mixture-averaged diffusion and dash-dotted [-·-·-·] curve for USC-mech II, and a solid red [——] curve for the revised San Diego mechanism.

tally, radial streaks were visible on the surface of the flame, as shown in Figure 3.13, in the shaded region of the plots at pressures above 1.0 MPa. The streaks appeared to tend to align with the screen pattern and may be responsible for early flame extinction For these reasons, it is unclear whether the experimental or computational results are more reliable at these higher pressures.

Because of the evident poor performance of the San Diego mechanism at the higher pressures, attention was focused on possible deficiencies in the chemical kinetics of that mechanism. Sensitivity studies and computations with revised rate parameters pointed to the importance of reactions involving HO_2 at elevated pressures. Study of more recent literature indicated deficiencies in rate parameters of two steps involving HO_2 in the current San Diego mechanism. One concerns the direct recombination step $O+OH+M\Leftrightarrow HO_2+M$ for which the original rate, based on older literature, had to be lowered [29] to avoid large discrepancies with syngas data, but the lowered value still

Figure 3.13: Photograph of an nonpremixed methane-air flame with a fuel mass fraction $Y_{F,1}= 0.14$ at $1.6\,\text{MPa}$ displaying radial streaks.

remained higher than a recent upper limit indicated by Burke et al [12], who chose to eliminate this step entirely, on the grounds that whatever the rate is (its value currently being unknown) it cannot be rapid enough to influence results of any combustion predictions. Following Burke et al [12], we therefore now eliminate this step entirely from San Diego mechanism.

The other reaction for which important new information is available is the step $HO_2+OH\Leftrightarrow H_2O+O_2$, which also removes radicals and thereby contributes to lowering the extinction strain rate at higher pressures. The rate for this step in the USC mechanism is much larger than the rate in the current San Diego mechanism and is largely responsible for the good agreement of USC mechanism in Figure 3.12. The rate in that mechanism was obtained by adding the contribution from a number of channels predicted by ab-initio computations [30, 31], but recent experiments [32] clearly show that that rate is too high. The experiments, however, do demonstrate the existence of an important high-temperature channel not contained in the current San Diego description but present (with too high a rate) in the USC mechanism. That channel therefore was added to San Diego mechanism, producing the specific reaction-rate constant.

$$k = 2.89 \times 10^{13} exp\left(250/T\right) + 4.5 \times 10^{14} exp\left(-5500/T\right), \tag{3.1}$$

the last term of which is the reported [32] high-temperature term.

Finally, although producing only a minor improvement in the agreement between predictions and experiments the prefactor 4.79×10^{13} cm^3/mol s for the step H$_2$O$_2$+H$\Leftrightarrow$ HO$_2$+H$_2$, employed in San Diego mechanism prior to 2011, but 2.1 times the current value in the mechanism, was re-introduced, there being uncertainty in this rate, with the current value the lowest in the literature. It is seen in Figure 3.12 that, with these three revisions, the predictions of San Diego mechanism are quite close to those of the USC mechanism at the higher pressures and agree with the experimental results within experimental uncertainty. In previously published extinction strain rates for hydrogen [13], predictions of the San Diego mechanism with mixture-averaged transport were found to reflect the experimental pressure dependences well but to give strain rates greater than those found experimentally; possibly because of the transport descriptions. Computations show that these revisions to the mechanism have very little influence on these predictions, because the flame temperatures were lower in the hydrogen experiments, and the changes have little effect at lower temperatures.

The aforementioned streaks seen in the flames at the higher pressures remain steady and appear to have their origin at the axis of symmetry, extending in the radial direction. Their appearance becomes increasingly pronounced with increasing pressure. The repeatability of the experimental data on critical conditions for extinction is not influenced by the formation of these streaks, but they may further decrease the measured extinction strain rates for $p > 1.0$ MPa through locally higher strain caused by the streaks, which could explain the disagreement between experiments and computations. In order to test for this, nitrogen was replaced by helium as the diluent for both fuel and oxygen at similar conditions to lower the Reynolds number and thereby decrease possible tendencies towards instability. Experimentally, these streaks were not seen with helium, and the corresponding extinction results are shown in Figure 3.14 for $X_{F,1} = 0.25$ and $X_{O_2,2} = 0.28$. Despite substantial differences in absolute values of extinction strain rates, there is good relative agreement between experiments and predictions of the USC and revised San Diego mechanisms in Figure 3.14, even to the extent of a leveling tendency at high pressure. This experimental leveling in Figure 3.14, not seen in Figure3.12, provides further evidence that the streaks may cause premature extinction. The disagreement for the absolute values of extinction strain rates can be possibly attributed to chaperone efficiencies. The USC mechanism has generally larger helium efficiencies for third-body
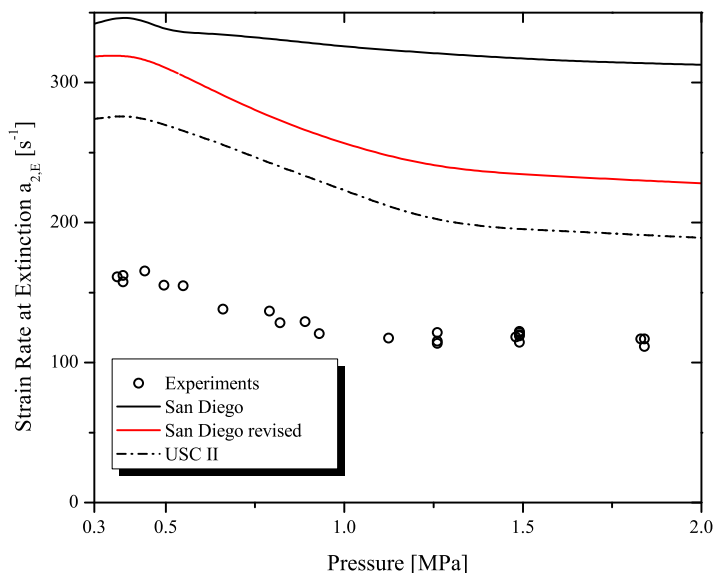
Figure 3.14: The strain rate at extinction, $a_{2,E}$ as a function of pressure, for a methane flame diluted with helium at fixed $X_{F,1} = 0.25$ and $X_{O_2,2} = 0.28$. Open symbols represent experimental data, while computations are represented by a solid [——] curve for San Diego mechanism with mixture-averaged diffusion and a dash-dotted [-·--·-·] curve for USC-mech II, and a solid red [——] curve for the revised San Diego mechanism.

reactions than the San Diego mechanism, and the San Diego predictions can be forced to agree with experiments by increasing the efficiencies for helium in the step $H+O_2+M\Leftrightarrow HO_2+M$ of that mechanism from 0.7 to 4.5, although such a large value would certainly be questionable, and it might be better to attribute the difference to the transport description.

Figure 3.15 shows critical extinction conditions for diluted ethane flames at fixed $Y_{F,1} = 0.12$. Similar to methane, experimental data show that, with increasing pressure, the strain rate at extinction first increases, attains a maximum value between 0.5 MPa and 0.6 MPa, and then decreases. Both the San Diego and USC mechanisms are in agreement with the data in Figure 3.15, within experimental error, for pressures up to 0.5 MPa. The predictions for the pressure at which the extinction strain rate pressures peak are, however, substantially higher than found experimentally, suggesting possible inaccuracies in all mechanisms or transport descriptions at the higher pressures. The differences in the predictions of different mechanisms are not very great in Figure 3.15.
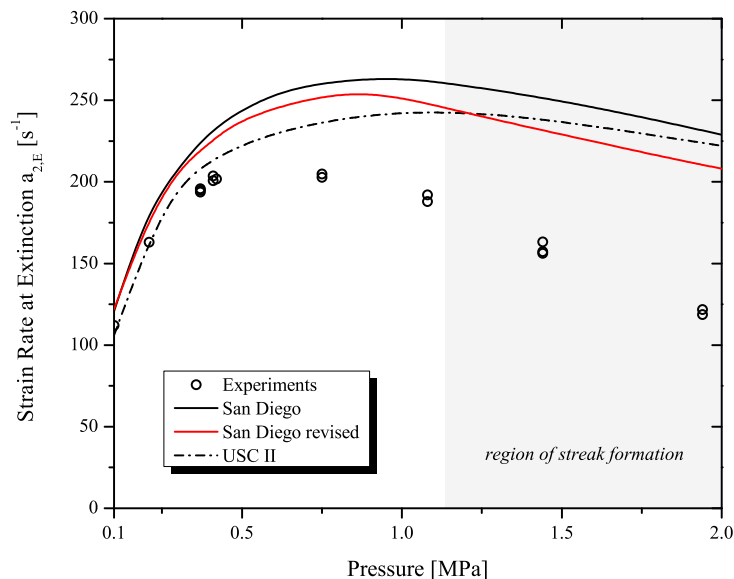
Figure 3.15: Experimentally obtained strain rates at extinction, $a_{2,\mathrm{E}}$, for ethane diluted with nitrogen as a function of pressure, p, at fixed and $Y_{\mathrm{F},1} = 0.12$. The oxidizer is air. Open symbols represent experimental data, while computations are represented by a solid [——] curve for San Diego mechanism with mixture-averaged diffusion and a dash-dotted [–·–·–·] curve for USC-mech II, and a solid red [——] curve for the revised San Diego mechanism.

Figure 3.16 shows critical conditions of extinction for diluted ethylene flames at fixed $Y_{\mathrm{F},1} = 0.09$. The qualitative behavior is similar to that of ethane, with a maximum extinction strain rate attained at $0.5\,\mathrm{MPa}$ experimentally but at higher pressures computationally. Substantial disagreement is found for higher pressures, for all mechanisms. Unlike the situation with ethane, there are substantial differences between the predictions of the San Diego and USC mechanism for ethylene, and revisions to the San Diego mechanism have comparatively minor influences on the predictions for ethane and ethylene, which have lower flame temperatures and are influenced more strongly by C_2 chemistry. It is unclear to what extent the substantial overprediction of the extinction strain rates by the San Diego mechanism for ethylene are due to the use of mixture-averaged transport. It is interesting that for both ethane and ethylene the value of the pressure at which the extinction strain rate is predicted to peak is noticeably smaller and somewhat closer to the experiments for the San Diego mechanism than for the USC
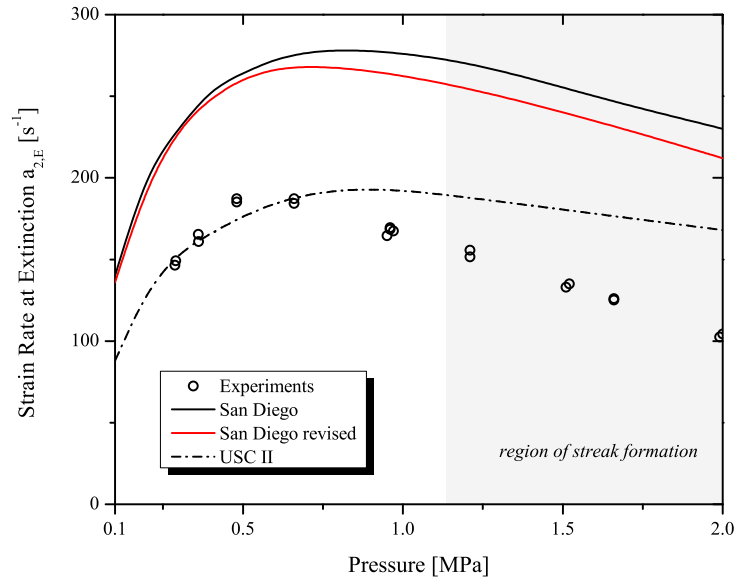
Figure 3.16: Experimentally obtained strain rates at extinction, $a_{2,\mathrm{E}}$, for ethylene diluted with nitrogen as a function of pressure, p, at fixed $Y_{\mathrm{F},1} = 0.09$. The oxidizer is air. Open symbols represent experimental data, while computations are represented by a solid [———] curve for San Diego mechanism with mixture-averaged diffusion and a dash-dotted [-·--·-·] curve for USC-mech II, and a solid red [———] curve for the revised San Diego mechanism.

mechanism.

Figure 3.17 shows the strain rate at extinction, $a_{2,\mathrm{E}}$, for methane flames as a function of the mass fraction of fuel, $Y_{\mathrm{F},1}$, at two fixed values of pressure, $p = 0.5\,\mathrm{MPa}$ and $p = 1.0\,\mathrm{MPa}$. At $p = 0.5\,\mathrm{MPa}$, extinction strain rates were investigated in the range $0.125 \leq Y_{\mathrm{F},1} \leq 0.24$, and for $p = 1.0\,\mathrm{MPa}$ in the range $0.125 \leq Y_{\mathrm{F},1} \leq 0.2$. The experimental data exhibit the expected result that at fixed p the value of $a_{2,\mathrm{E}}$ increases with increasing $Y_{\mathrm{F},1}$. The agreement between the computations with the USC mechanism and experiments is excellent, consistent with the agreement in Figure 3.12. All chemical-kinetic mechanisms used here correctly predict the slope of these curves of extinction strain rates as a function of fuel mass fractions.
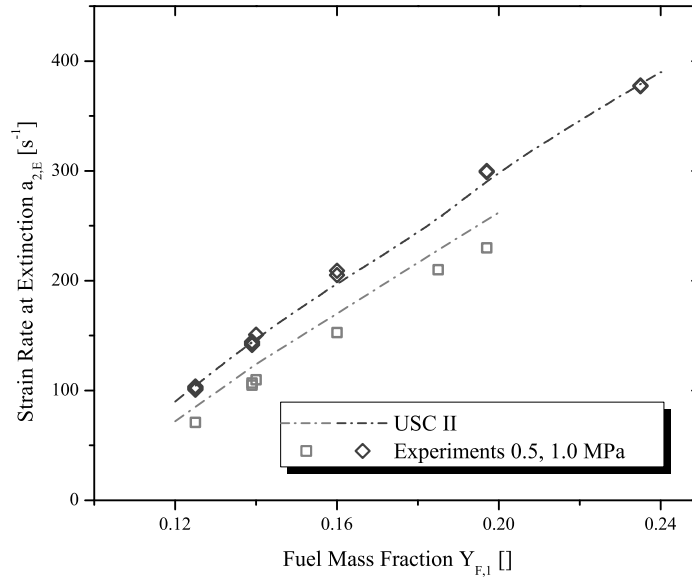
Figure 3.17: The strain rate at extinction, $a_{2,\mathrm{E}}$, for methane diluted with nitrogen as a function of the mass fraction of fuel, $Y_{\mathrm{F},1}$, at fixed values of pressure $p = 0.5\,\mathrm{MPa}$ and $p = 1.0\,\mathrm{MPa}$. Open symbols represent experimental data, while computations are represented by dash-dotted [–·–·–·] lines for USC-mech II.

3.3 Concluding Remarks

The newly designed high-pressure combustion facility was used to study the structures and extinction conditions of counterflow diffusion flames in air for nitrogen-diluted hydrogen, methane, ethane, and ethylene, from 0.1 MPa to 2.0 MPa. This experimental investigation showed that pressure has a substantial effect on critical extinction conditions for hydrogen and gaseous hydrocarbon diffusion flames. Extinction strain rates first increase in the moderately elevated pressure range until a peak value is attained, above which a decreasing trend begins. Even though past theoretical findings and present chemical-kinetic mechanisms already exhibit a high level of understanding of this subject with regards to hydrogen, this is the first experimental evidence that confirms the predicted non-monotonic pressure-dependent extinction behavior of nonpremixed hydrogen flames. For the range of pressures investigated here, it has been found that the maximum flame temperature at extinction increases with pressure, also in agreement with previous predictions. In addition, as expected, it was confirmed experimentally that the flame

thickness decreases with increasing pressure and that flames of the same composition are equally positioned independent of pressure and move towards the stagnation plane with increasing strain rate.The occurrence of streaks observed experimentally in the hydrocarbon flames warrants further investigations concerning their possible influence on flame extinction between 1.0 MPa to 2.0 MPa. The further decrease in extinction strain rates with increasing pressure in this range when streaks are visible was not observed when nitrogen was replaced by helium in the methane flame. Experimental data obtained in the pressure range between 0.1 MPa and 1.0 MPa can be considered to be accurate since it is sufficiently far away from the onset of the formation of streaks. This accuracy is also supported by the temperature profiles measured in this range, which showed good agreement with numerical predictions and scalability when account was taken of influences of flame radiation. Chemical-kinetic mechanisms were found to perform with varying success, which is not surprising since this is the first study addressing the extinction of highly diluted counterflow diffusion flames for low-molecular weight hydrocarbon fuels at elevated pressures. Minor revisions to San Diego mechanism for hydrocarbon reactions substantially improve agreement for methane flames, but further investigations of rate parameters for steps involving carbon-containing species definitely are warranted, aimed at improving the performance of the mechanism at high pressure. Future studies need to address the problem of streak formation because there is practical interest in flames with nitrogen rather than helium as a diluent. Such studies would expand the valid pressure range for high-pressure counterflow experiments.

Acknowledgement

References

[1] G. Del Alamo. *Theoretical Studies of Hydrogen Ignition and Droplet Combustion.* PhD thesis, UCSD, 2006.

[2] R. A. Strehlow and A. Cohen. Initiation of detonation. *Physics of Fluids*, 5:97–101, 1962.

[3] E.L. Petersen, D.F. Davidson, M. Rohrig, and R.K. Hanson. High-Pressure Shock Tube Measurements of Ignition Times in Stoichiometric H2/O2/Ar Mixtures. *20th Int. Symp. on Shock Waves*, pages 941–946, 1996.

[4] P. Papas, I. Glassman, and C. K. Law. Effects of pressure and dilution on the extinction of counterflow nonpremixed hydrogen-air flames. *Aerospace Engineering*, pages 1333–1339, 1994.

[5] K. Seshadri and F. A. Williams. Laminar flow between parallel plates with injection of a reactant at high Reynolds number. *International Journal of Heat and Mass Transfer*, 21(2):251–253, 1978.

[6] The San Diego Mechanism. The San Diego Mechanism. *http://combustion.ucsd.edu*, 2011.

[7] A. Cuoci, A. Frassoldati, T. Faravelli, and E. Ranzi. Soot formation in unsteady counterflow diffusion flames. *Proceedings of the Combustion Institute*, 32:1335–1342, 2008.

[8] A. Cuoci, A. Frassoldati, T. Faravelli, and E. Ranzi. Frequency response of counterflow diffusion flames to strain rate harmonic oscillations. *Combustion Science and Technology*, 180:767–784, 2008.

[9] K. Seshadri, A. Frassoldati, A. Cuoci, T. Faravelli, U. Niemann, P. Weydert, and E. Ranzi. Experimental and kinetic modeling study of combustion of JP-8, its surrogates and components in laminar premixed flows. *Combustion Theory and Modelling*, 15:569–583, 2011.

[10] C. H. Sohn and S. H. Chung. Effect of pressure on the extinction, acoustic pressure response, and NO formation in diluted hydrogenair diffusion flames. *Combustion and Flame*, 121(1-2):288–300, 2000.

[11] GRI-Mechanism 3.0. GRI-Mechanism 3.0. *http://www.me.berkeley.edu/gri_mech/*, 1999.

[12] M.P. Burke, M. Chaos, Y. Ju, F.L. Dryer, and S.J. Klippenstein. Comprehensive H2/O2 kinetic model for high-pressure combustion. *International Journal of Chemical Kinetics*, accepted for publication, 2011.

[13] U. Niemann, K. Seshadri, and F.A. Williams. Effect of pressure on structure and extinction of near-limit hydrogen counterflow diffusion flames. *Proceedings of the Combustion Institute*, 34(1):881 – 886, 2013.

[14] C. H. Sohn and S. H. Chung. Effect of pressure on the extinction, acoustic pressure response, and NO formation in diluted hydrogenair diffusion flames. *Combustion and Flame*, 121:288–300, 2000.

[15] L. Figura and A. Gomez. Laminar counterflow steady diffusion flames under high pressure. *Combustion and Flame*, 159:142–150, 2011.

[16] K. Maruta, K. Abe, S. Hasegawa, S. Maruyama, and J. Sato. Extinction characteristics of CH_4/CO_2 versus O_2/CO_2 counterflow non-premixed flames at elevated pressures up to 0.7 MPa. *Proceedings of the Combustion Institute*, 31:1223–1230, 2007.

[17] H. Böhm and F. Lacas. On extinction limits and polycyclic aromatic hydrocarbon formation in strained counterflow diffusion flames from 1 to 6 bar. *Proceedings of the Combustion Institute*, 28:2627–2634, 2000.

[18] J. Sato. Extinction of Counterflow Diffusion Flame in High Pressures. *Combustion Science and Technology*, 75:103–113, 1991.

[19] Takashi Niioka, Susumu Hasegawa, Tatsuro Tsukamoto, and Jun'ichi Sato. Diffusion-flame extinction of liquid fuel at elevated pressures. *Combustion and Flame*, 86(12):171 – 178, 1991.

[20] Tetsuo Hiraiwa, Naomichi Ono, and Takashi Niioka. High-pressure combustion characteristics of liquid fuel in the stagnation-point flow. *Symposium (International) on Combustion*, 24(1):239 – 245, 1992.

[21] ChemkinPro Release 15112, Reaction Design, Inc., San Diego, CA. 2012.

[22] H. Wang, X. You, A.V. Joshi, S.G. Davis, A. Laskin, F. Egolfopoulos, and C.K. Law. USC Mech Version II, High-Temperature Combustion Reaction Model of H2/CO/C1-C4 Compounds. *http://ignis.usc.edu/USC_Mech_II.htm*, 2007.

[23] R. M. Fristrom. *Flame Temperature Measurements*, Volume 72, pages 118–120. 1995.

[24] R.S. Barlow, A.N. Karpetis, J.H. Frank, and J.-Y. Chen. Scalar profiles and NO formation in laminar opposed-flow partially premixed methane/air flames. *Combustion and Flame*, 127(3):2102 – 2118, 2001.

[25] W.L. Grosshandler. RADCAL: A narrow-band model for radiation calculations in a combustion environment. *NIST Technical Note*, 1402:52, 1993.

[26] L Pons, N Darabiha, and S Candel. Pressure effects on nonpremixed strained flames. *Combustion and Flame*, 152(1-2):218–229, 2008.

[27] D. Bradley and A. G. Entwistle. Determination of the emissivity, for total radiation, of small diameter platinum-10% rhodium wires in the temperature range 600-1450C. *British Journal of Applied Physics*, 12(12):708, 1961.

[28] A. Liñán. The asymptotic structure of counterflow diffusion flames for large activation energies. *Acta Astronautica*, 1:1007–1039, July 1974.

[29] P. Saxena and F. A. Williams. Testing a small detailed chemical-kinetic mechanism for the combustion of hydrogen and carbon monoxide. *Combustion and Flame*, 145:316–323, 2006.

[30] R. Sivaramakrishnan, A. Comandini, R.S. Tranter, K. Brezinsky, S.G. Davis, and H. Wang. Combustion of CO/H2 mixtures at elevated pressures. *Proceedings of the Combustion Institute*, 31(1):429 – 437, 2007.

[31] Xiaoqing You, Hai Wang, Elke Goos, Chih-Jen Sung, and Stephen J. Klippenstein. Reaction kinetics of CO + HO2 - products: Ab initio transition state theory study with master equation modeling. *The Journal of Physical Chemistry A*, 111(19):4031–4042, 2007.

[32] Zekai Hong, King-Yiu Lam, Ritobrata Sur, Shengkai Wang, David F. Davidson, and Ronald K. Hanson. On the rate constants of OH+HO2 and HO2+HO2: A comprehensive study of H2O2 thermal decomposition using multi-species laser absorption. *Proceedings of the Combustion Institute*, 34:565 – 571, 2013.

Chapter 4

Flame Structure of Alcohols

4.1 Gas Chromatographic Sampling System

Concentrations of stable species are measured by removing gas samples from the reaction zone using a heated quartz microprobe, with a copper-shielded front end, and analyzing them in a gas chromatograph. The microprobe has a tip with an outer diameter of $150 \, \mu$m and an inner diameter of $300 \, \mu$m. The tip is placed at a location of $5 \, $mm off the centerline of the ducts to minimize disturbances to the flow-field. The location of the sampling probe in the flow-field is determined using a digital photo camera. The size of one pixel in the camera corresponds to a distance in the flow-field of approximately $20 \, \mu$m. The mole fractions of various species in the sample are measured using an Agilent 3000microGC gas chromatograph. This instrument is equipped with a 10 m 5A molecular sieve column, a 8 m Poraplot U column with a $10 \, \mu$m film, a 8m Poraplot Q column with a $10 \, \mu$m film, and a 8 m OV-1 column with a $2 \, \mu$m coating. The molecular sieve column uses Argon as a carrier gas and separates H_2, O_2 and, N_2, CH_4, and CO. All other columns use helium as a carrier gas. The Poraplot U column is used for separating CO_2, C_2H_4, C_2H_6, C_2H_2, and CH_20. The Poraplot Q column is used for separating H_20, C_3H_4, C_3H_6, C_3H_8, C_2H_4O, and C_4H_6. The OV-1 column is used for separating n-/iso-C_3H_8O and n-/iso-C_4H_9O.The mole fractions of various species eluding from the columns are measured using thermal-conductivity detectors (TCD). The detectors are calibrated using samples of known composition.

The work presented here uses a gas-chromatograph that is designed to measure natural gas and species of similar molecular size. To be able to quantify concentrations of
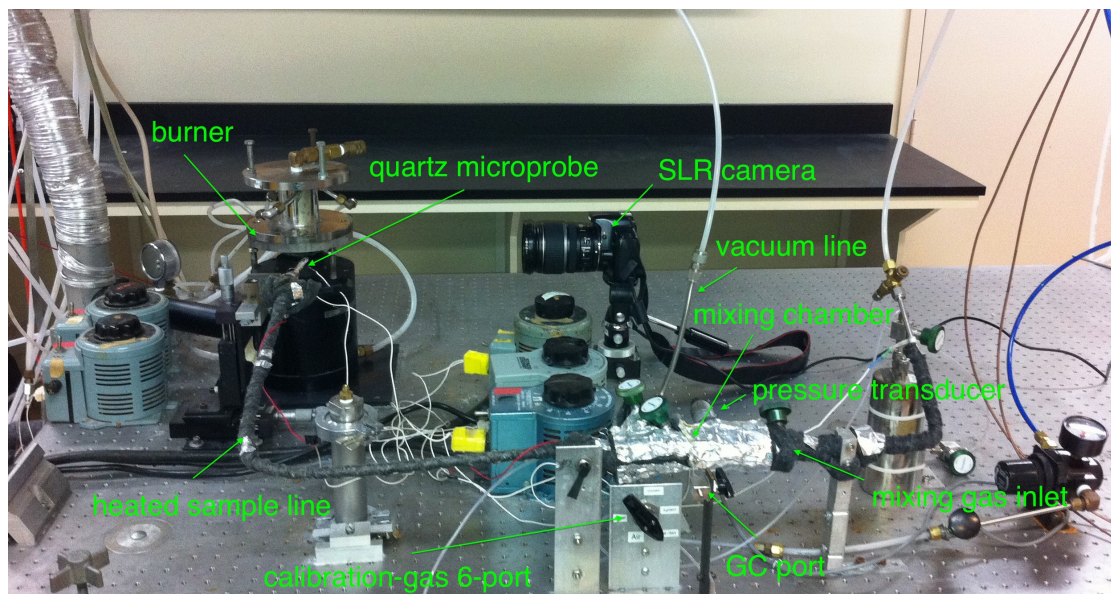
Figure 4.1: Photograph of the experimental setup including a gaschromatographic sampling system employed in the investigation of the structure propanol and butanol diffusion flames

species of much higher molecular weight, the sample underwent a conditioning process before the injection into the apparatus. The goal was to lower the amount of heavy species in the sample by dilution with nitrogen, and thus avoid overloading the columns and the detectors. Figure 4.1 is a photograph of the sampling system. The sample is removed from the flame through a quartz probe, accelerating the gas to sonic speed at the orifice and freezing all reactions during the subsequent gas expansion in the diverging part of the probe. The probe is heated to avoid condensation. From there the sample is transported through heated stainless-steel lines into the mixing chamber. The gas chromatograph employed, uses a built-in sample pump. To ensure equal sample sizes and thus comparable results across all measurements, a constant sample inlet pressure is required. Therefore stable species are sampled at a constant pressure of 60 mbar into a sample vessel and topped off with nitrogen to a total pressure of 1150 mbar. After a waiting period of 6 minutes, to allow sufficient mixing, the sample is drawn into the GC. The cylindrical stainless steel sample vessel with an inner volume of 20ml, which is placed in between the sample probe and the GC, and all lines from the sample probe to the GC are heated to $100°C$. The calibration for stable species included the injection of liquids with a syringe through a septum in the wall of a sample vessel. The sample vessel is completely evacuated when the liquid is injected. Based on the pressure

reading after complete evaporation and dilution with nitrogen the species fraction can be determined. This procedure is used for alcohols, formaldehyde and water. All other species are calibrated with calibration gas of known composition. The peaks for all species presented here show very good separation. Therefore the expected accuracy for the maximum concentrations of most species is expected to be better than $\pm 10\%$. The expected accuracy for water is assumed to be $\pm 20\%$.

4.2 Propyl Alcohols

4.2.1 Introduction

The need to limit the increase in greenhouse gas levels in the environment has motivated numerous studies on combustion of renewable fuels. Oxygen containing biofuels, in particular alcohols, show considerable promise, because they are considered to be neutral in regard to net greenhouse gas emissions to the environment. As a consequence, numerous experimental and modeling studies have been carried out to characterize combustion of methanol, ethanol, propanol (C_3H_7OH), and butanol [1–33]. Alcohols when used as additives to fossil fuels, in particular gasoline, reduce the formation of polyaromatic hydrocarbon compounds, particulates, and soot. Ethanol is widely used as biofuel additive to gasoline. Recent work suggests that use of alcohols as fuels has some deleterious effects on human health, due to high emission levels of toxic oxygenated by-products such as aldehydes [34]. Moreover, high concentrations of acetone [$(CH_3)_2CO$] were detected in the exhaust gas of a spark ignition engine upon addition of *iso*-propanol to a synthetic fuel [35]. The formation of oxygenated pollutants is a common feature of alcohol combustion that calls for detailed kinetic studies of the combustion chemistry of alcohol fuels [32]. Here, a kinetic modeling study of combustion of the propanol isomers, *n*-propanol and *iso*-propanol is carried out.

Only few kinetic studies of oxidation of *n*-propanol and *iso*-propanol are reported in the literature; they include experimental studies using batch [24–26] and flow reactors [10], shock-tubes [33], co-flow diffusion flames [1], counterflow diffusion flames [29], droplet burning [30] and low-pressure premixed flat flames [31, 32]. The combustion and pyrolysis of *n*-propanol has been also investigated in reflected shock waves with particular attention to the formation of soot and polycyclic aromatic hydrocarbons [23]. Funda-

mental investigations include studies on thermal decomposition of *iso*-propanol [27] and structures of flames over liquid pools [28]. The structure of nonpremixed *iso*-propanol flames was measured previously employing the co-flow configuration [1] and the counterflow configuration [29]. The structure of diffusion flames depend on the stoichiometric mixture fraction and the strain rate [36–38]. The previous measurements of the structure of *iso*-propanol flames were made with the oxidizer stream made up of air enriched with oxygen [29]. The experimental conditions were characterized by high values of the stoichiometric mixture fraction and low values of the strain rates. Combustion in practical systems are characterized by low values of the stoichiometric mixture fraction and both low and high values of the strain rates [39]. To complement the previous studies new experimental data on the structure of counterflow diffusion flames of *n*-propanol and *iso*-propanol are presented here. The structure was measured with air as the oxidizer. The experimental conditions are characterized by low values of stoichiometric mixture fraction and moderately high values of strain rate. The new experimental data allow comparison of the flame structures of propanol isomers. The new experimental data are helpful in a further tuning and validating kinetic models of alcohol fuels.

4.2.2 Experimental Measurements of Flame Structure

The structures of nonpremixed flames of *n*-propanol and *iso*-propanol were measured employing the counterflow configuration as described in Section A.1. Figure A.3 shows a schematic illustration of the setup and a description is provided in Section A.1.2. Steady, axisymmetric, laminar flow of two counterflowing streams toward a stagnation plane is considered. In this configuration a fuel stream made up of prevaporized fuel (*n*-propanol or *iso*-propanol) and nitrogen is injected from the fuel-duct, and an oxidizer stream of air is injected from the oxidizer-duct. Characteristics of the flowfield and boundary conditions are defined equal to the description provided in the appendix A. The distance between the fuel boundary and the oxidizer boundary is represented by $L = 10 \, \mathrm{mm}$.

The flowfield is characterized through the characteristic strain rate Equation A.1 on the oxidizer side and the stoichiometric mixture fraction Equation A.2 as defined in Section A.1.

The profiles of concentration of stable species were measured for $Y_{\mathrm{F},1} = 0.3$, $T_1 = 353 \, \mathrm{K}$, $Y_{\mathrm{O_2},2} = 0.233$, $T_2 = 298 \, \mathrm{K}$, $a_2 = 97.5 \, \mathrm{s^{-1}}$, $V_1 = 0.235 \, \mathrm{m/s}$, $V_2 = 0.25 \, \mathrm{m/s}$,
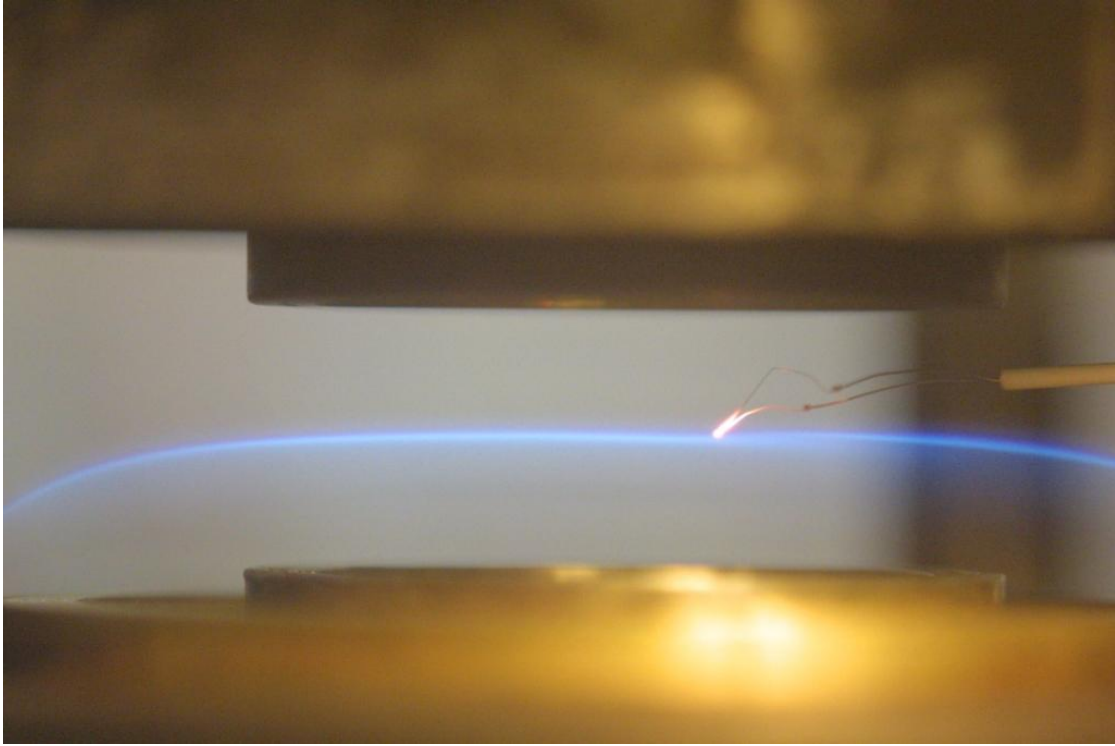
Figure 4.2: Photograph of a nonpremixed n-propanol flame stabilized in the counterflow burner for $Y_{F,1} = 0.3$, $T_1 = 353\,\text{K}$, $Y_{O_2,2} = 0.233$, $T_2 = 298\,\text{K}$, $a_2 = 97.5\,\text{s}^{-1}$, $V_1 = 0.235\,\text{m/s}$, $V_2 = 0.25\,\text{m/s}$, and $L = 10\,\text{mm}$. The figure shows the quartz microprobe.

and $L = 10\,\text{mm}$. At these conditions the stoichiometric mixture fraction $Z_{\text{st}} = 0.2449$. Concentrations of stable species were measured by removing gas samples from the reaction zone using a heated quartz microprobe, and analyzing them in a gas chromatograph. The microprobe has a tip with an inner diameter of $150\,\mu\text{m}$. To minimize disturbances to the flow-field, the tip of the microprobe was placed at a location of $5\,\text{mm}$ off the axis of symmetry and the procedure is described in detail in Section 4.1.

Temperature profiles were measured for n-propanol and iso-propanol flames, using a Platinum-Platinum $13\,\%$ Rhodium thermocouples (R-type), at conditions identical to those employed in the measurement of concentration profiles. The measurements were made along a line that is parallel to the axis of symmetry and approximately $5\,\text{mm}$ away from the axis. The exact location of the thermocouple bead was determined using a digital photo camera. Figure 4.2 shows the photograph of a n-propanol flame stabilized in the counterflow burner. The measurements were made with bare thermocouple wires (uncoated) as well as with coated thermocouple wires. The wire diameter of the bare

(uncoated) thermocouple was $25\,\mu$m and the bead diameter was $90\,\mu$m. The coated thermocouple had a layer of BeO/Y_2O_3 to avoid catalytic reactions at the surface of the thermocouple [40]. Additional information on the measurement of temperature profiles is provided in Section 4.3.2. The flame structure of n-propanol is shown in Figure 4.5 and that of iso-propanol in Figure 4.6. The comparison with predictions of the kinetic model are discussed later.

Detailed Kinetic Mechanism of n-Propanol and iso-Propanol

The pyrolysis and oxidation mechanisms of propanol isomers are very similar to those for hydrocarbon fuels. Therefore, the development of a complete set of the primary propagation reactions for these fuels requires the study and the definition of few new kinetic parameters for reactions involving bonds and H atoms near to the OH group. The elementary pyrolysis and oxidation reactions of methanol and ethanol are reasonably well-known and have been revised recently [9, 10, 13–16]. The kinetic mechanism for methanol and ethanol are a useful starting point for the extension to the kinetic schemes of n-propanol and iso-propanol. Initiation reactions are generally evaluated, by assuming a reference frequency factor with the activation energy equal to the bond energy, and microscopic reversibility based on the reverse radical recombination reaction is applied. Metathesis reactions require defining the reactivity of the H atoms in hydroxyl position and the H atoms in α position. Remaining H atoms are presumed to be unaffected by the presence of the OH group. Isomerization reactions of these radicals are of limited importance and are neglected. Unimolecular reactions, metathesis reactions, decomposition reactions of primary radicals from alcohol fuels, and four-center molecular dehydration reactions are discussed in more detail in Frassoldati et al [41].

Figure 4.3 is a schematic illustration of n-propanol and iso-propanol decomposition. The detailed sub-mechanism of n- and iso-propanol is reported in Frassoldati et al [41]. Further decomposition and/or oxidation reactions of primary intermediate products are described in a semi-detailed oxidation mechanism for hydrocarbon fuels up to C16 developed in previous studies [42, 43]. The overall kinetic scheme is based on hierarchical modularity and is made up of more than 7000 reactions among 300 species. Thermochemical data for most species was obtained from the CHEMKIN thermodynamic database [44, 45]. For those species for which thermodynamic data is not available in the
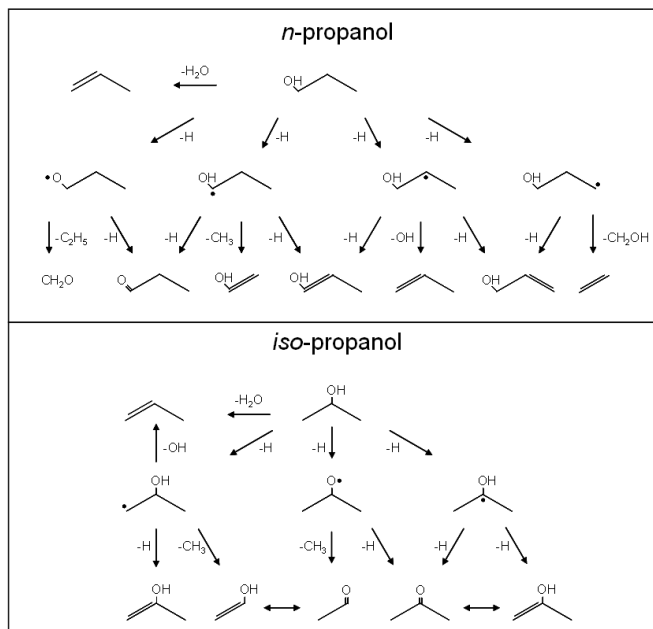
Figure 4.3: Chemical reaction pathways of *n*-propanol and *iso*-propanol decomposition.

literature, the group additive method was used to estimate these properties [46]. The complete mechanism is available online [47].

4.2.3 Nonpremixed Flames of *n*-Propanol and *iso*-Propanol

Experimental measurements on counterflow nonpremixed flames discussed in Section 4.2.2 are compared with model predictions in Figures 4.5 and 4.6. Figure 4.6 shows the structure of a nonpremixed *iso*-propanol flame while Figure 4.5 shows the structure of a nonpremixed *n*-propanol flame. These figures show the mole fraction of various species as a function of distance from the fuel boundary. The symbols in these figures represent experimental data and the lines are model prediction. The profiles in these figures were obtained at a strain rate $a_2 = 97.5\,\mathrm{s}^{-1}$, and the stoichiometric mixture fraction $Z_{\mathrm{st}} = 0.2449$. There are a number of similarities between the flame structure of these isomers. The measured profile of ethylene shows that the concentration of this compound is higher in the *n*-propanol flame in comparison to its concentration in the *iso*-propanol flame. This large difference in ethylene peaks is properly predicted. As already mentioned, ethylene is only a secondary product in *iso*-propanol decomposition. This fact is well evident in Figure 4.4, which shows the reaction flux analysis of the two
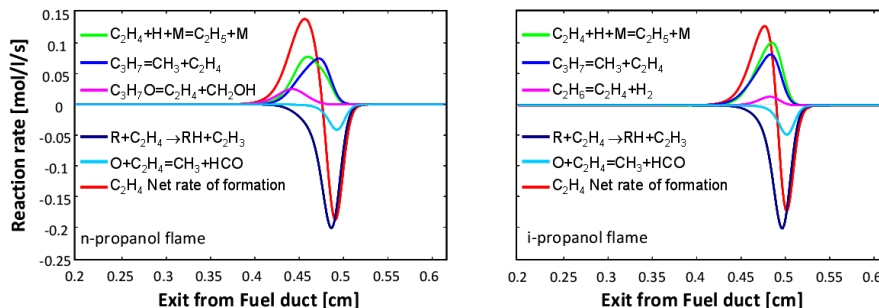
Figure 4.4: Reaction flux analysis of ethylene formation in propanol flames of Figures 4.5 and 4.6

flames. Ethylene formation from *iso*-propanol is only due to the dehydrogenation of ethyl radicals (formed via recombination of methyl radicals) and to the de-methylation of *n*-propyl radical (formed via H addition reaction on propylene). On the contrary, primary ethylene formation from *n*-propanol is also sustained by the $\beta-$decomposition reaction of the $\bullet CH_2CH_2CH_2OH$ radical (see Figure 4.3). In *iso*-propanol and *n*-propanol flames, ethylene consumption is mainly due to the H-abstraction reactions to form vinyl radical in the fuel region and to the addition reaction of O radical in the flame front:

$$O + C_2H_4 \rightleftharpoons CH_3 + HCO$$
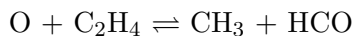
The kinetic model satisfactorily predicts the profile of acetone in *n*-propanol flame (Figure 4.5) and propanal in *iso*-propanol flame (Figure 4.6). The agreement between the predicted and measured profiles of oxygenated and C2 species is satisfactory. Figure 4.6 shows that the predicted profile of propylene agrees with experimental data. These data are useful both in order to confirm the experimental measurements and to verify the possible systematic deviations between model predictions and experiments.

The temperature profiles of counterflow flames of *n*-propanol and *iso*-propanol were measured as well, using a bare and a coated thermocouple and are shown in Figure 4.5(d) and Figure 4.6(d). The temperature measured by the bare thermocouple is higher than that recorded by the coated thermocouple. This clearly indicates that there is catalytic heating of the bare wire. Figure 4.5(d) and Figure 4.6(d) show that the predictions of the kinetic model agrees with the experimental data.

64
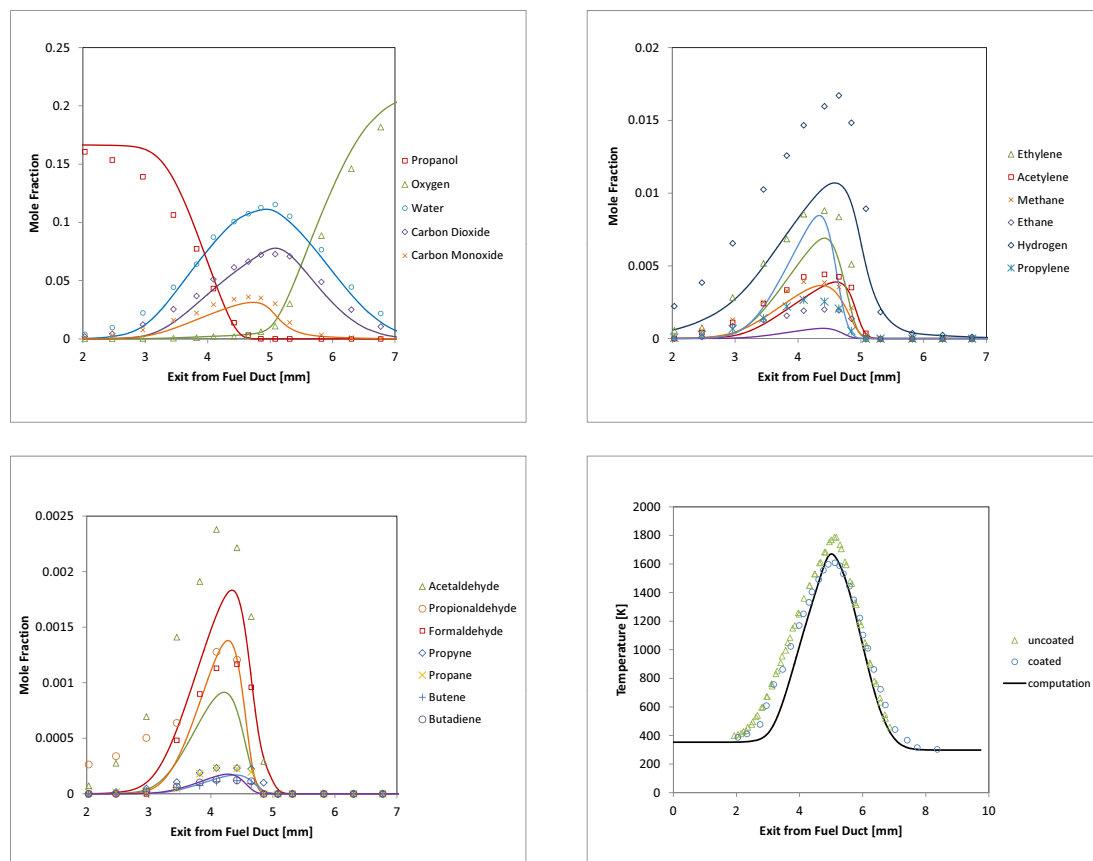
Figure 4.5: Profiles of temperature and mole fraction of various species as a function of distance from the fuel boundary for non-premixed n-propanol flames at a value of the strain rate $a_2 = 97.5\,\mathrm{s}^{-1}$, and the stoichiometric mixture fraction $Z_\mathrm{st} = 0.2449$. The symbols represent experimental data and the lines are model predictions.
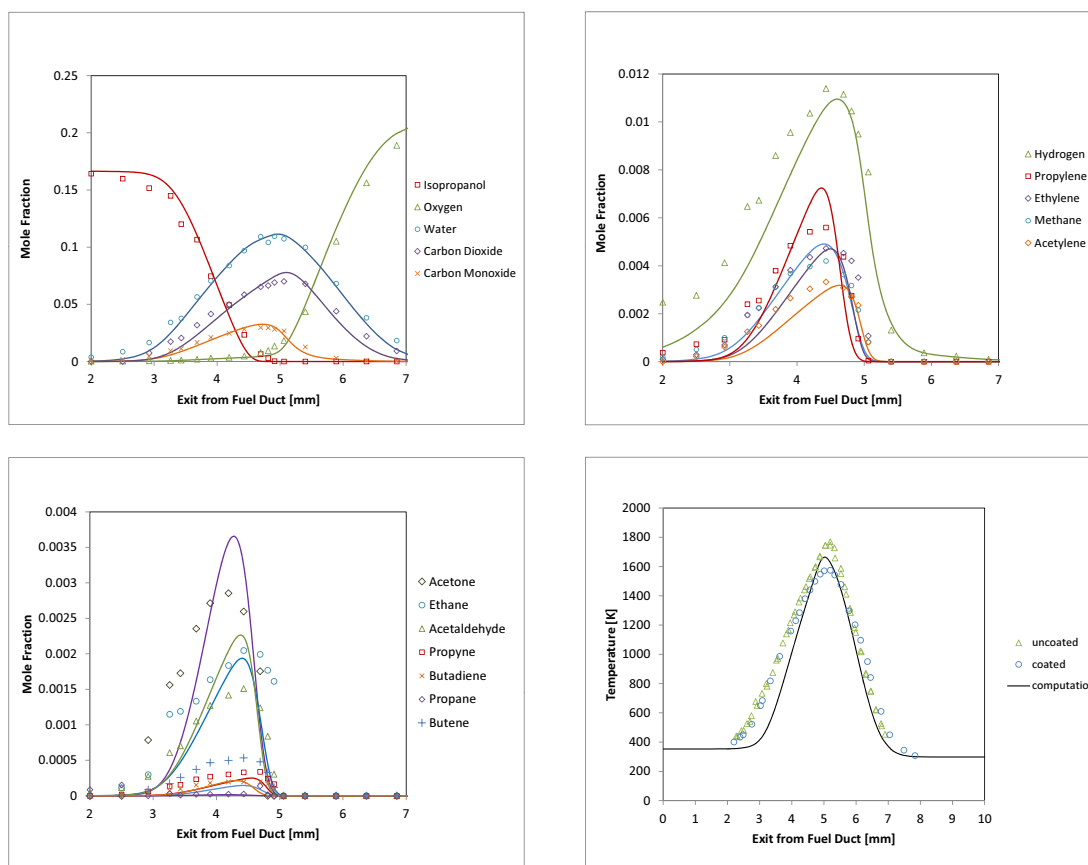
Figure 4.6: Profiles of temperature and mole fraction of various species as a function of distance from the fuel boundary for non-premixed *iso*-propanol flames at a value of the strain rate $a_2 = 97.5\,\mathrm{s}^{-1}$, and the stoichiometric mixture fraction $Z_{\mathrm{st}} = 0.2449$. The symbols represent experimental data and the lines are model predictions.

4.3 Butyl Alcohols

4.3.1 Introduction

Recent interest in promoting the use of bio-fuels arises from the need to improve energy security and reduce net greenhouse gas emissions. At the present rate of energy consumption, worldwide reserves of natural gas, oils and to a limited extent coal are rapidly diminishing. This process is being accelerated by significant increases in the rates of energy consumption in developing countries. These developments have increased the cost of fossil fuels and have an adverse impact on the national economies of the world. Thus, there is a need to decrease the use of fossil fuels for sustainable development, and allow future generations to continue the use of fossil fuels. Recent legislation in many countries require them to limit emissions of greenhouse gases. Bio-fuels are carbon neutral, thus they are considered to be more environmentally friendly and help in meeting legislative requirements by limiting emissions of greenhouse gases. Both E.U. and U.S. are committed to reducing energy consumption and to increase renewable fuel use. All these point to increasing use of bio-fuels in the near future.

Alcohols show significant potential to be an alternative to conventional gasoline. Alcohols are renewable fuels because they can be produced from biomass fermentation and are by-products of Fischer Tropsch processes. Ethanol is currently a component of reformulated gasoline. The amount of ethanol in gasoline is projected to increase in the future. There is considerable interest in promoting the use of butanol (C_4H_9OH) as an alternative to ethanol. Butanol can be derived from lignocellulosic materials. Butanol has some advantages, as transportation fuel component, when compared with ethanol. It is less corrosive, has a lower vapor pressure, higher energy density, and its octane rating is similar to that of gasoline. Thus, it can be blended with gasoline at much higher proportions than ethanol without compromising efficiency. Butanol is immiscible when mixed with water at concentrations higher than about 7-8 %. This eliminates a number of storage concerns and makes phase separation considerably easier in comparison to ethanol. Unfortunately, butanol has a foul odor that can persist for a long time. Butanol is yet to be employed as extensively as ethanol as transportation fuel, because the production of butanol is labor intensive and only low yields have been achieved. These limitations are expected to improve in the near future.

Numerous studies have addressed combustion of methanol [5, 10, 48–51], ethanol

[8–14, 52, 53] and propanol isomers [41]. These studies provide the building blocks for the kinetic modeling of combustion of butanol isomers. The isomers of butanol are n-butanol (n-C_4H_9OH), sec-butanol (sec-C_4H_9OH), iso-butanol (iso-C_4H_9OH), and $tert$-butanol ($tert$-C_4H_9OH). Dagaut and Togbé [19] developed a sub-mechanism for n-butanol, which was combined with an overall kinetic mechanism of oxidation of gasoline. Moss et al. [20] have proposed a detailed kinetic scheme for describing the high-temperature oxidation of the different butanol isomers. Recently, Black et al. [54] have tested predictions of a kinetic model of n-butanol oxidation with autoignition delay times measured in shock tubes, and data on evolution of various species measured in a jet-stirred reactor, with encouraging results. These studies [19, 20, 54] were restricted to premixed systems without flow. Studies on premixed combustion with molecular transport are available [17, 18]. McEnally and Pfefferle [17] studied pollutant emissions from methane/air flames doped with the four butanol isomers. Yang et al. [18] studied laminar premixed, low-pressure flames of the four butanol isomers, by using photoionization mass spectrometry. The structures of nonpremixed n-butanol flames in nonuniform flows were measured previously employing the counterflow configuration [22]. The structure of nonpremixed flames depend on the stoichiometric mixture fraction, Z_{st}, and the strain rate [36–38]. The previous measurements of the structure of n-butanol flames were made with the oxidizer stream made up of air enriched with oxygen [22]. The experimental conditions were characterized by high values of the stoichiometric mixture fraction and low values of the strain rates. Combustion in practical systems are characterized by low values of the stoichiometric mixture fraction and both low and high values of the strain rates [39]. To complement the previous studies, new experimental data on the structures of counterflow nonpremixed flames of n-butanol and iso-butanol are shown here. The flame structures are measured with air as the oxidizer. The experimental conditions are characterized by low values of stoichiometric mixture fraction, and moderately high values of strain rate. The new experimental data allows comparison of the flame structures of butanol isomers. The new experimental data together with previous experimental data are helpful for validating the kinetic model of alcohol fuels.

A hierarchical approach is found to be useful for developing detailed and semi-detailed mechanism for describing oxidation of various fuels. This method starts from lower molecular weight compounds of a family of species and proceeds to higher molecular weight compounds. This procedure allows extensions to other compounds using

similarity and analogy rules. Using this procedure, validated kinetic mechanisms of oxidation of ethanol [53] and propanol isomers have been developed [41]. Here, an oxidation scheme that considers the primary reactions of the butanol isomers is tested for n-butanol and iso-butanol.

4.3.2   Experimental Measurements of Flame Structure

The structures of nonpremixed flames of n-butanol and iso-butanol were measured employing the counterflow configuration as described in Section A.1. Figure A.3 shows a schematic illustration of the setup and a description is provided in Section A.1.2.

Steady, axisymmetric, laminar flow of two counterflowing streams toward a stagnation plane is considered. In this configuration, a fuel stream made up of prevaporized fuel (n-butanol or iso-butanol) and nitrogen is injected from the fuel-duct, and an oxidizer stream of air is injected from the oxidizer-duct. These jets flow into the mixing layer between the two ducts. Characteristics of the flowfield and boundary conditions are defined equal to the description provided in the Appendix A. The distance between the fuel boundary and the oxidizer boundary is represented by $L = 10\,\mathrm{mm}$.
The flowfield is characterized through the characteristic strain rate in Equation A.1 on the oxidizer side and the stoichiometric mixture fraction in Equation A.2 as defined in Section A.1. For stoichiometric combustion of butanol, $\nu = 2.5946$.

The profiles of concentration of stable species were measured for $Y_{\mathrm{F},1} = 0.3$, $T_1 = 353\,\mathrm{K}$, $Y_{\mathrm{O}_2,2} = 0.233$, $T_2 = 298\,\mathrm{K}$, $a_2 = 100\,\mathrm{s}^{-1}$, $V_1 = 0.248\,\mathrm{m/s}$, $V_2 = 0.25\,\mathrm{m/s}$, and $L = 10\,\mathrm{mm}$. At these conditions, the flame is on the oxidizer side of the stagnation plane with the stoichiometric mixture fraction $Z_{\mathrm{st}} = 0.23$. Figure 4.7 shows the photograph of a n-butanol flame stabilized in the counterflow burner. Concentrations profiles of stable species were measured by removing gas samples from the reaction zone using a heated quartz microprobe, and analyzing them in a gas chromatograph.

Temperature profiles were measured for n-butanol and iso-butanol flames, using a Platinum-Platinum 13 % Rhodium thermocouples (R-type), at conditions identical to those employed in the measurement of concentration profiles. As shown in Figure 2.1, the measurements were made along a line that is parallel to the axis of symmetry and approximately 5 mm away from the axis. The exact location of the thermocouple bead was determined using a digital photo camera. The measurements were made with bare thermocouple wires (uncoated) as well as with coated thermocouple wires. The wire
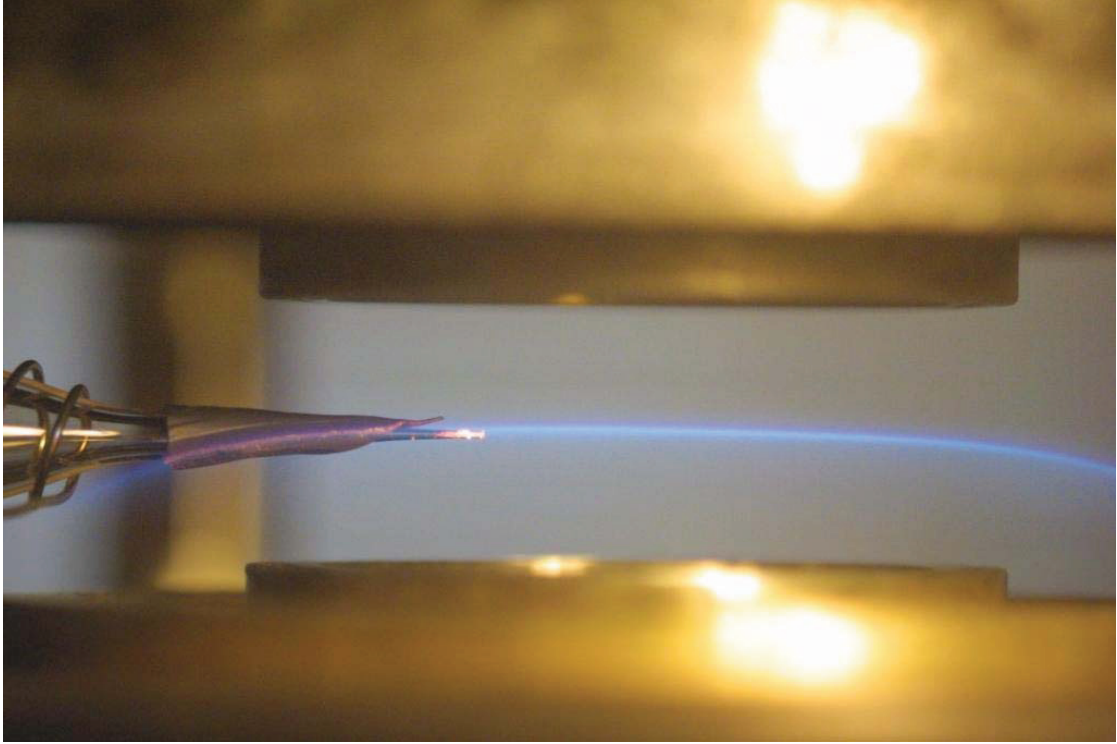
Figure 4.7: Photograph of a nonpremixed n-butanol flame stabilized in the counterflow burner for $Y_{F,1} = 0.3$, $T_1 = 353$ K, $Y_{O_2,2} = 0.233$, $T_2 = 298$ K, $a_2 = 100\,\mathrm{s}^{-1}$, $V_1 = 0.248\,\mathrm{m/s}$, $V_2 = 0.25\,\mathrm{m/s}$, and $L = 10$ mm.

diameter of the bare (uncoated) thermocouple was $25\,\mu$m and the bead diameter was $90\,\mu$m. The coated thermocouple had a layer of BeO/Y_2O_3 to avoid catalytic reactions at the surface of the thermocouple [40]. The coating was performed following the procedure recommended in Reference [40]. The wire diameter of the coated thermocouple was $35\,\mu$m and the bead diameter was $135\,\mu$m. The measured temperatures with both thermocouples were corrected by taking into consideration radiative heat losses from the surface of the thermocouple. The corrections were made employing the procedure described by Peterson and Laurendeau [55]. The convective heat transfer from the gas to the thermocouple was estimated assuming that the thermocouple is a cylinder placed in cross flow, with the Nusselt number of 0.5. The Reynolds number used for estimating the Nusselt number was evaluated using the wire diameters as the characteristic length, the characteristic velocity was V_2 and the kinematic viscosity was estimated at a temperature of 1500 K. The Reynolds number was 0.0055 for the uncoated thermocouple and 0.0075 for the coated thermocouple. The Prandtl number was 0.7. The heat losses from

the wire by radiation was estimated assuming an emissivity of 0.2 for the uncoated wire and 0.6 for the coated wire. At the peak value of the measured temperature, the radiation correction was approximately $50\,\mathrm{K}$ for bare thermocouple and $100\,\mathrm{K}$ for the coated thermocouple. The absolute accuracy of the temperature measurement is expected to be better than $\pm\,40\,\mathrm{K}$. The flame structure of n-butanol is shown in Figures 4.12(a) and 4.10 and that of *iso*-butanol in Figures 4.12(b) and 4.11. The comparison with predictions of the kinetic model are discussed later.

Kinetic mechanism and reaction classes

Figures 4.8 and 4.9 show simplified primary decomposition mechanisms for two isomers of butanol—n-butanol and *iso*-butanol. As shown in Figure 4.8, five different radicals are formed via H-abstraction reactions from n-C_4H_9OH. Subsequently, these radicals isomerise and decompose. 1-Butene (1-C_4H_8) is the result of the molecular dehydration reaction as well as the de-hydroxylation reaction of n-C_4H_9OH-β radical. Butanal (n-C_3H_7CHO) and/or butenyl alcohols are formed from dehydrogenation reactions of all the five primary radicals. Butanal, methyl-ethyl-ketone (MEK) and methyl-propanal are also formed by molecular dehydrogenation of n-butanol and *iso*-butanol, respectively. Allyl and vinyl alcohols are formed from β-decomposition reactions of n-C_4H_9OH-α and n-C_4H_9OH-β. Alpha-unsaturated alcohols are considered as directly transformed into the corresponding aldehydes, through the keto-enol tautomerism. For the sake of brevity, isomerisation reactions among the primary butanol radicals were not reported in this scheme.
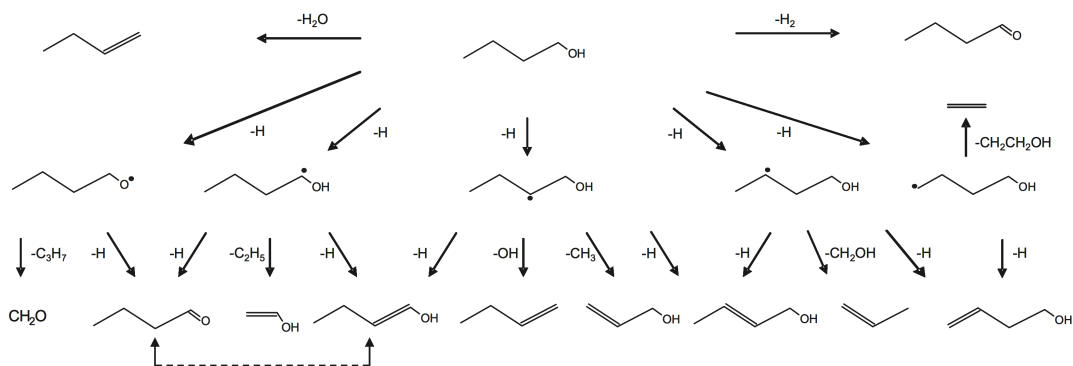
Figure 4.8: Chemical reaction pathways of primary decomposition reactions of n-butanol
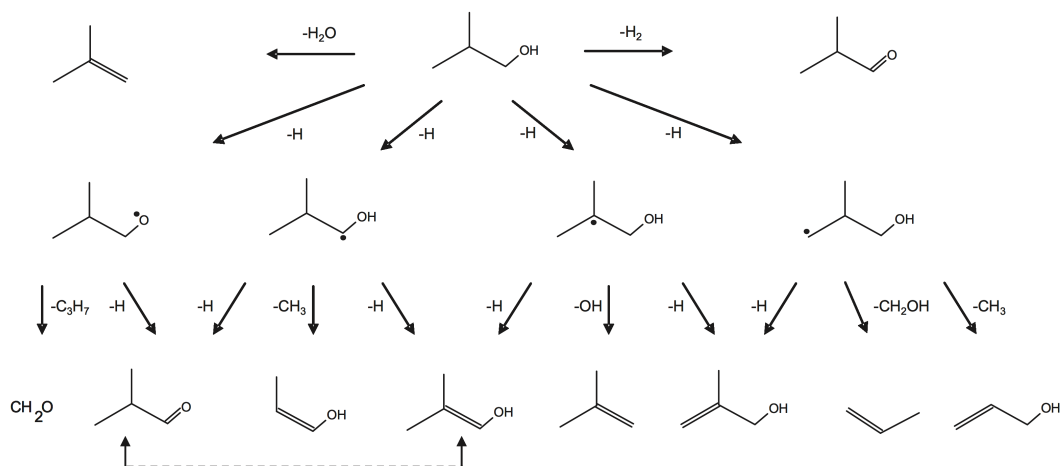
Figure 4.9: Chemical reaction pathways of primary decomposition reactions of *iso*-butanol

The pyrolysis and oxidation mechanisms of butanol isomers are similar to those for hydrocarbon fuels. The development of the complete set of the primary propagation reactions for butanol isomers proceeds from the extension of the kinetic parameters for similar reactions already studied and recently revised for ethanol, *n*-propanol and *iso*-propanol [8–14, 41, 52, 53]. The kinetic study of oxidation of *n*-propanol and *iso*-propanol is a useful starting point for the extension of the kinetic scheme to butanol isomers [41]. Initiation reactions are, in general, evaluated by assuming a reference frequency factor, A, with the activation energy, E equal to the bond energy, and microscopic reversibility based on the reverse radical recombination reaction is applied. Metathesis reactions require defining the reactivity of the H atoms in hydroxyl position and the H atoms in α position. Remaining H atoms are presumed to be unaffected by the presence of the OH group. Isomerization reactions of these radicals are significant and could enhance the role of the very reactive alkoxy radical.

A detailed description including unimolecular initiation reactions, metathesis reactions, isomerization reactions and four-center molecular dehydration reactions, and the detailed sub-mechanism of all of the four butanol isomers is available in Grana et al [56]. Further pyrolysis and/or oxidation reactions of intermediate products are described in a semi-detailed oxidation mechanism for hydrocarbon fuels up to C16 developed previously [42, 43, 57]. The overall kinetic scheme is based on hierarchical modularity and is made up of more than 7000 reactions among 300 species. Thermochemical data for

most species was obtained from the CHEMKIN thermodynamic database [44, 45]. For those species for which thermodynamic data is not available in the literature, the group additive method was used to estimate these properties [46]. The complete mechanism, with thermodynamic and transport properties, is available in CHEMKIN format [47].

4.3.3   Nonpremixed Flames of *n*-Butanol and *iso*-Butanol

Experimental measurements of the structure of counterflow nonpremixed flame of *n*-butanol, discussed in Section 4.3.2, are compared with model predictions in Figures 4.11 and 4.10. Figure 4.12 shows the temperature profiles measured using the bare (uncoated) thermocouple and the coated thermocouple. The measured values of the temperature are the same everywhere except in the vicinity of the position of maximum temperature. The maximum temperature recorded by the uncoated thermocouple is about 200 K higher than that measured using the coated thermocouple. This indicates that the chemical reactions are not in equilibrium near the location where the temperature is the highest. As a consequence, there is catalytic heating on the surface of the uncoated thermocouple. The predicted temperature profile is slightly narrow when compared with experimental data obtained using the coated thermocouple. The agreement is considered to be satisfactory. Figures 4.12(a) and 4.10 compare the predicted profiles of temperature and various species with experimental data. The predicted profiles of the reactants n-C_4H_9OH, and O_2, final products CO_2 and H_2O, and the key intermediates H_2 and CO agree well with experimental data. The predicted and measured profiles show that the peak values of CO and H_2 are located at the position where the concentration of fuel is very small. The peak values of CO_2, H_2O and temperature are observed on the right side of the position where the concentration of fuel is very small. This is consistent with the asymptotic description of flame structure where the reaction zone is separated into two layers—an inner layer and and outer layer [49–51]. In the inner-layer, butanol reacts with radicals and the final intermediates formed are CO and H_2. These intermediates are oxidized to CO_2 and H_2O in the outer-layer. The predicted profiles of CH_4, C_2H_2, C_2H_4, C_2H_6, C_3H_6, C_4H_6 and C_4H_8 agree well with the measurements. Butanal was also detected in the *n*-butanol flame. The measured concentrations were very low. Therefore, they are not shown in Figure 4.10.

Figures 4.12(b) and 4.11 compare predictions of the kinetic model of the structure of nonpremixed *iso*-butanol flame with experimental data. The *iso*-butanol flame

structure was measured at conditions identical to those shown in Figures 4.12(a) and 4.10 for n-butanol. The maximum value of the temperature recorded by the uncoated thermocouple is about 200 K higher than that measured using the coated thermocouple. The predicted temperature profile agrees well with the measurements obtained using the coated thermocouple. The predicted profiles of the n-C_4H_9OH, O_2, CO_2, H_2O, CO, H_2, C_2H_4, C_2H_2 and C_3H_6 agree well with the measurements. The asymptotic flame structure constructed from the profiles of the reactants, products and major intermediates are similar to that of n-butanol.

Temperature profiles of the n-butanol and *iso*-butanol flames shown in Figures 4.12(a) and 4.12(b) are similar, due to the same boundary conditions employed. Comparison of Figures 4.10 and 4.11 show that the mole fractions of CH_2O are similar, while the mole fraction of CH_3CHO is lower in the *iso*-butanol flame. Trace amounts of butanal was observed in the n-butanol flame but none in the *iso*-butanol flame.

4.4   Concluding Remarks

New experimental data on counterflow nonpremixed flames were obtained for validation a kinetic mechanism that describes the primary reactions of pyrolysis and combustion of n-propanol, *iso*-propanol, n-butanol, and *iso*-butanol. Flame structures were measured under similar conditions for all fuels to elucidate the similarities and differences in combustion characteristics. The profiles measured included those of formaldehyde, acetaldehyde, propanal, and acetone. The agreement between the kinetic model and experimental data was generally satisfactory, in terms of reactivity and selectivity in major products and minor species. The flame structures and overall combustion characteristics of n-propanol and *iso*-propanol were found to be similar. Modeling showed that ethylene was only a secondary product of *iso*-propanol combustion and its amount was significantly lower. Acetone was formed under all conditions in *iso*-propanol flames, while propanal was formed in n-propanol flames. The flame structures and overall combustion characteristics of the two butanol isomers were found to be similar and also similar to those of the two propanol isomers.
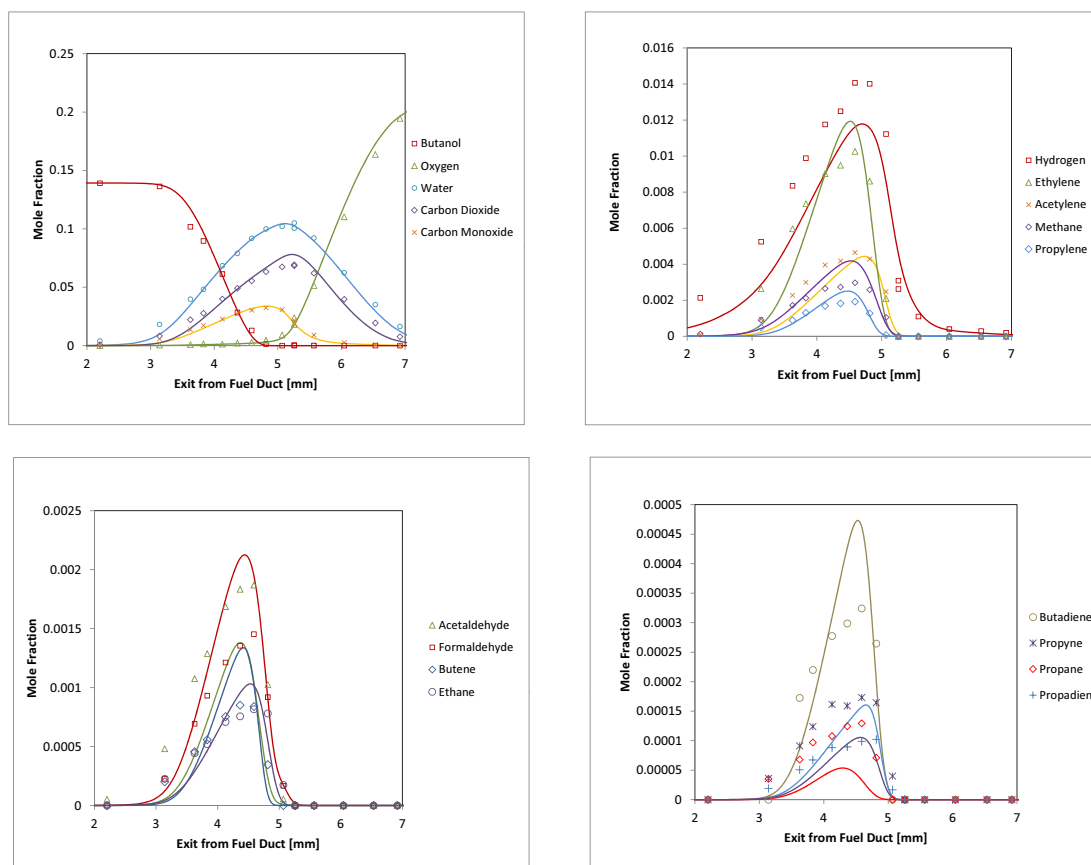
Figure 4.10: Profiles of mole fraction of various species as a function of distance from the fuel boundary for non-premixed n-butanol flames at a value of the strain rate $a_2 = 100\,\mathrm{s}^{-1}$, and the stoichiometric mixture fraction $Z_{\mathrm{st}} = 0.23$. The symbols represent experimental data and the lines are model predictions.
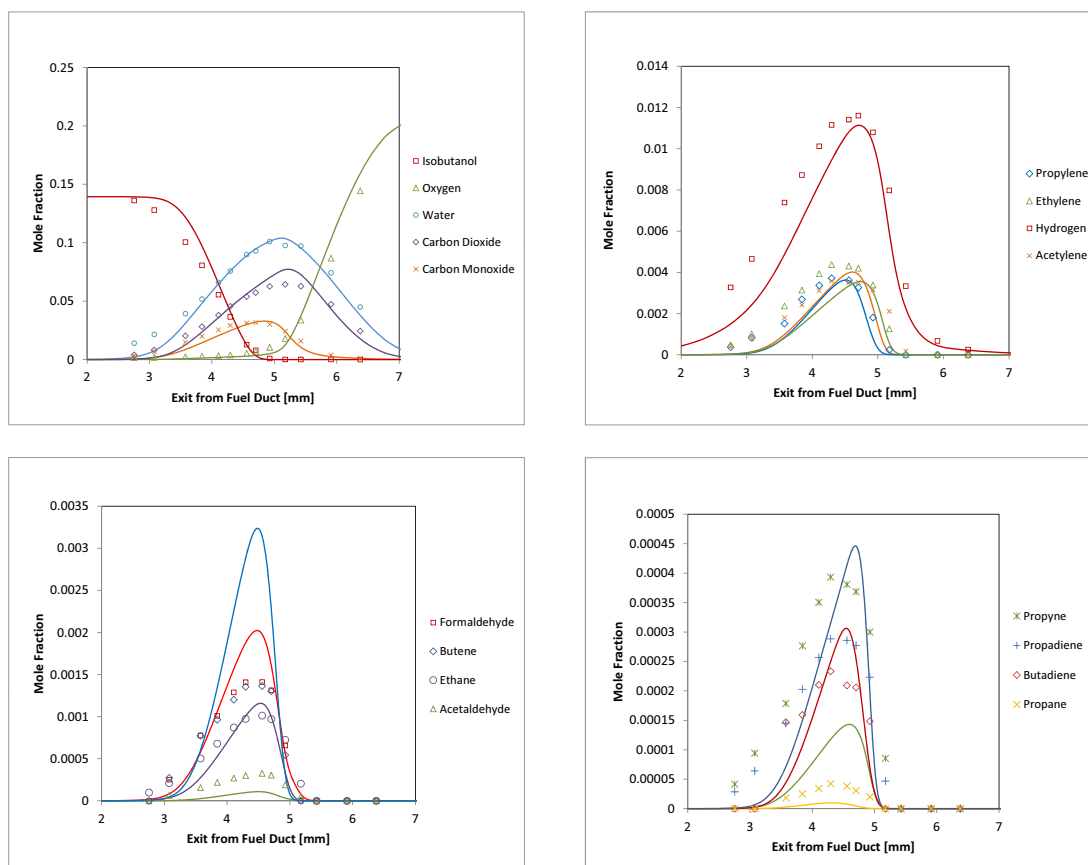
Figure 4.11: Profiles of mole fraction of various species as a function of distance from the fuel boundary for non-premixed *n*-butanol flames at a value of the strain rate $a_2 = 100\,\mathrm{s}^{-1}$, and the stoichiometric mixture fraction $Z_{\mathrm{st}} = 0.23$. The symbols represent experimental data and the lines are model predictions.

Figure 4.12: Temperature as a function of distance from the fuel boundary for non-premixed *n*-butanol and an *iso*-butanol flames at a value of the strain rate $a_2 = 100\,\mathrm{s}^{-1}$, and the stoichiometric mixture fraction $Z_{\mathrm{st}} = 0.23$. The symbols represent experimental data and the lines are model predictions.
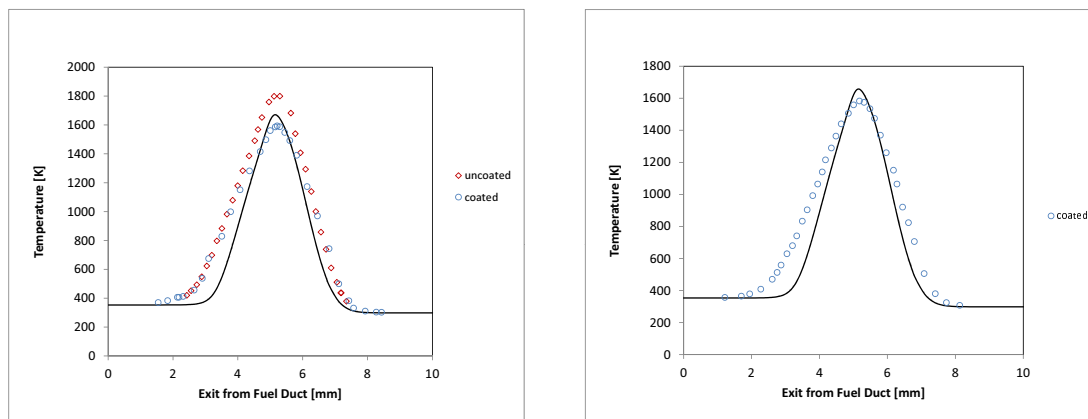
Acknowledgement

References

[1] S. R. Smith and A. S. Gordon. Studies of diffusion flames. II. diffusion flames of some simple alcohols. *Journal of Physical Chemistry*, 60 (8):1059–1062, 1956.

[2] K. Seshadri. Structure and extinction of laminar diffusion flames above condensed fuels with water and nitrogen. *Combustion and Flame*, 33:197–215, 1978.

[3] A. Hamins and K. Seshadri. The influence of alcohols on the combustion of hydrocarbon fuels in diffusion flames. *Combustion and Flame*, 64:43–54, 1986.

[4] A. Hamins and K. Seshadri. The structure of diffusion flames burning pure, binary, and ternary solutions of methanol, heptane, and toluene. *Combustion and Flame*, 68:295–307, 1987.

[5] S. C. Li and F. A. Williams. Experimental and numerical studies of two-stage methanol flames. *Proceedings of the Combustion Institute*, 26:1017–1024, 1996.

[6] T. Held and F. Dryer. A comprehensive mechanism for methanol oxidation. *International Journal of Chemical Kinetics*, 118:805–830, 1998.

[7] O. L. Gülder. Laminar burning velocities of methanol, ethanol and isooctane-air mixtures. *Proceeings of the Combustion Institute*, pages 275–281, 1982.

[8] N. Marinov. A detailed kinetic model for high temperature ethanol oxidation. *International Journal of Chemical Kinetics*, 31:183–220, 1999.

[9] R. Seiser, S. Humer, K. Seshadri, and E. Pucher. Experimental investigation of methanol and ethanol flames in nonuniform flows. *Proceedings of the Combustion Institute*, 31:1173–1180, 2007.

[10] T. S. Norton and F. L. Dryer. The flow reactor oxidation of C_1–C_4 alcohols and mtbe. *Proceedings of the Combustion Institute*, 23:179–185, 1990.

[11] F. N. Egolfopoulos, D. X. Lu, and C. K. Law. A study on ethanol oxidation kinetics in laminar premixed flames, flow reactors and shock tubes. *Proceedings of the Combustion Institute*, 24:833–841, 1992.

[12] W. Tsang. Energy transfer effects during the multichannel decomposition of ethanol. *International Journal of Chemical Kinetics*, 36 (8):456–465, 2004.

[13] P. Saxena and F. A. Williams. Numerical and experimental studies of ethanol flames. *Proceedings of the Combustion Institute*, 31:1149–1156, 2007.

[14] P. Dagaut and C. Togbé. Experimental and modeling study of the kinetics of oxidation of ethanol-gasoline surrogate mixtures (E85 surrogate) in a jet-stirred reactor. *Energy & Fuels*, 22:3499–3505, 2008.

[15] M. Abián, C. Esarte, A. Millera, R. Bilbao, and M. U. Alzueta. Oxidation of acetylene-ethanol mixtures and their interaction with NO. *Energy & Fuels*, 22:3814–3823, 2008.

[16] A. Frassoldati, A. Cuoci, T. Faravelli, and E. Ranzi. Kinetic modeling of the oxidation of ethanol and gasoline surrogate mixtures. *Mediterranean Combustion Symposium MCS06, Ajaccio France, June 7-11, 2009*, 2009.

[17] C. McEnally and L. D. Pfefferle. Fuel decomposition and hydrocarbon growth processes for oxygenated hydrocarbons: Butyl alcohols. *Proceedings of the Combustion Institute*, 30:1363–1370, 2005.

[18] B. Yang, P. Oßwald, Y. Li, J. Wang, L. Wei, Z. Tian, F. Qi, , and K. Kohe-Höinghaus. Identification of combustion intermediates in isomeric fuel-rich premixed butanol–oxygen flames at low pressure. *Combustion and Flame*, 148:198–209, 2007.

[19] P. Dagaut and C. Togbé. Oxidation kinetics of butanol-gasoline surrogate mixture in a jet-stirred reactor: Experimental and modeling study. *Fuel*, 87:3313–3321, 2008.

[20] J.T. Moss, A. M. Berkowitz, M. A. Oehlschlaeger, J. Biet, A. Warth, P. A. Glaude, and F Battin-Leclerc. An experimental and kinetic modelling study of the oxidation of four isomers of butanol. *Journal of Physical Chemistry*, 112:10843–10855, 2008.

[21] J. Moc, J. M. Simmie, and H. J. Curran. The elimination of water from a conformationally complex alcohol: A computational study of the gas phase dehydration of *n*-butanol. *Journal of Molecular Structure*, 928:149–157, 2009.

[22] S. M. Sarathy, M. J. Thomson, C. Togbé, P. Dagaut, F. Halter, and C. Mountaim-Rousselle. An experimental and kinetic modeling study of *n*-butanol combustion. *Combustion and Flame*, 156:852–864, 2009.

[23] R. Wang and P. Cadman. Soot and PAH Production from Spray Combustion of Different Hydrocarbons Behind Reflected Shock Waves. *Combustion and Flame*, 112:359–370, 1998.

[24] J.A. Barnard and H.W.D. Hughes. The pyrolysis of n-propanol. *Transactions of the Faraday Society*, 56 (1):64–71, 1960.

[25] J.A. Barnard. The pyrolysis of iso-propanol. *Transactions of the Faraday Society*, 56 (1):72–79, 1960.

[26] A. B. Trenwith. Thermal decomposition of isopropanol. *Journal of the Chemical Society, Faraday Transactions 1: Physical Chemistry in Condensed Phases*, 71:2405–2412, 1975.

[27] B. H. Bui, R. S. Zhu, and M. C. Lin. Thermal decomposition of iso-propanol: First-principles prediction of total and product-branching rate constants. *Journal of Chemical Physics*, 117 (24):11188–, 2002.

[28] J. Cai, F. Li, and W. A. Sirignano. Three–dimensional structures of flames over liquid fuel pools. *Combustion Science and Technology*, 175:2113–2139, 2003.

[29] A. Sinha and M. J. Thomson. The chemical structures of opposed flow diffusion flames of C3 oxygenated hydrocarbons (isopropanol, dimethoxymethane, and dimethyl carbonate) and their mixtures. *Combustion and Flame*, 136:548–556, 2004.

[30] B. D. Shaw and J. B. Wei. Propanol droplet flammability and combustion in air–diluent environments under normal and reduced gravity. *Combustion Science and Technology*, 179:1205–1223, 2007.

[31] Y. Li, L. Wei, Z. Tian, B. Yang, J. Wang, T. Zhang, and F. Qi. A comprehensive experimental study of low–pressure premixed C_3–oxygenated hydrocarbon flames with tunable synchrotron photoionization. *Combustion and Flame*, 152:336–359, 2008.

[32] T. Kasper, P. Oßwald, U. Struckmeier, K. Kohe-Höinghaus, C. A. Taatjes, J. Wang, T. A. Cool, M. E. Law, A. Morel, and P. R. Westmorelend. Combustion chemistry of propanol isomers—investigated by electron ionization and VUV-photoionization molecular-beam mass spectrometry. *Combustion and Flame*, 156:1181–1201, 2009.

[33] M. V. Johnson, S.S. Goldsborough, E. Larkin, G. O'Malley, Z. Serinyel, P. O'Toole, and H.J. Curran. Ignition delay measurements of n-propanol and iso-propanol in a shock tube. Proceedings of the 6th U. S. National Combustion Meeting, Paper # 22C5, The University of Michigan, Ann Arbor, Michigan, USA, May 17-20, 2009, 2009. The Combustion Institute.

[34] M. Z. Jacobson. Effects of ethanol (E85) versus gasoline vehicles on cancer and mortality in the united states. *Environmental Science and Technology*, 41 (11):4150–4157, 2007.

[35] E. Zervas, X. Montagne, and J. Lahaye. Emission of alcohols and carbonyl compounds from spark ignition engine. influence of fuel and air/fuel equivalance ratio. *Environmental Science and Technology*, 36:2414–2421, 2002.

[36] F. A. Williams. *Combustion Theory*. Addison-Wesley Publishing Company, Redwood City, CA, 2 edition, 1985.

[37] A. Liñán and F. A. Williams. *Fundamental Aspects of Combustion*, Volume 34 of *Oxford Engineering Science Series*. Oxford University Press, New York, 1993.

[38] N. Peters. Local quenching due to flame stretch and non-premixed turbulent combustion. *Combustion Science and Technology*, 30:1–17, 1983.

[39] N. Peters. *Turbulent Combustion*. Cambridge University Press, Cambridge, England, 2000.

[40] J. H. Kent. A noncatalytic coating for platinum-rhodium thermocouples. *Combustion and Flame*, 14:279–282, 1970.

[41] A. Frassoldati, A. Cuoci, T. Faravelli, U. Niemann, E. Ranzi, R. Seiser, and K. Seshadri. An experimental and kinetic modeling study of *n*-propanol and *iso*-propanol combustion. *Combustion and Flame*, 157:2–16, 2009.

[42] E. Ranzi, T. Faravelli, A. Frassoldati, and S. Granata. Wide range kinetic modeling study of pyrolysis and combustion of heavy *n*-alkanes. *Industrial and Engineering Chemistry*, 44:5170–5183, 2005.

[43] E. Ranzi, M. Dente, A. Goldaniga, G. Bozzano, and T. Faravelli. Lumping procedures in detailed kinetic modeling of gasification, pyrolysis, partial oxidation and combustion of hydrocarbon mixtures. *Progress in Energy and Combustion Science*, 27:99–139, 2001.

[44] R. J. Kee, F. Rupley, and J. A. Miller. The chemkin thermodynamic data base. Report sand86-8215b, Sandia National Laboratories, Livermore, California, 1987.

[45] R. J. Kee, F. Rupley, and J. A. Miller. The chemkin thermodynamic data base. Technical report, Sandia National Laboratories, Livermore, California, 1989.

[46] S. W. Benson. *Thermochemical Kinetics*. Wiley, New York, 2nd edition, 1996.

[47] http://www.chem.polimi.it/CRECKModeling.

[48] T. J. Held and F. L. Dryer. An experimental and computational study of methanol oxidation in the intermediate and high temperature range. In *Twenty-Fifth Symposium (International) on Combustion*, pages 901–908, Pittsburgh, Pennsylvania, 1994. The Combustion Institute.

[49] B. Yang and K. Seshadri. The asymptotic structure of methanol-air diffusion flames. *Combustion Science and Technology*, 97:193–218, 1994.

[50] K. Seshadri and F. A. Williams. Reduced chemical systems and their application in turbulent combustion. In P. A. Libby and F. A. Williams, editors, *Turbulent Reacting Flows*, pages 153–210. Academic Press, San Diego, California, 1994.

[51] K. Seshadri. Multistep asymptotic analyses of flame structures. *Proceedings of the Combustion Institute*, 26:831–846, 1996.

[52] M. Abáin, C. Esarte, A. A. Millera, R. Bilbao, and M. U. Alzueta. Oxidation of acelylene-ethanol mixtures and their interacion with NO. *Energy & Fuels*, 22:3814–3823, 2008.

[53] A. Frassoldati, A. Cuoci, T. Faravelli, and E. Ranzi. Kinetic modeling of the oxidation of ethanol and gasoline surrogate mixtures. *Combustion Science and Technology*, page in press, 2009.

[54] G. Black, H.J. Curran, S. Pichon, J.M. Simmie, and V. Zhukov. Bio-butanol: Combustion properties and detailed chemical kinetic model. *Combustion and Flame*, 157:363–373, 2010.

[55] R. C. Peterson and N. M. Laurendeau. The emittance of yttrium-beryllium oxide thermocouple coating. *Combustion and Flame*, 60:279–284, 1985.

[56] Roberto Grana, Alessio Frassoldati, Tiziano Faravelli, Ulrich Niemann, Eliseo Ranzi, Reinhard Seiser, Robert Cattolica, and Kalyanasundaram Seshadri. An experimental and kinetic modeling study of combustion of isomers of butanol. *Combustion and Flame*, 157(11):2137 – 2154, 2010.

[57] E. Ranzi. A wide-range kinetic modeling study of oxidation and combustion of transportation fuels and surrogate mixtures. *Energy and Fuels*, 20:1024–1032, 2006.

Chapter 5

Critical Conditions of Methyl Ester Combustion

5.1 Introduction

There is considerable interest in understanding the combustion of esters because they are considered as possible surrogates of biodiesel [1–12]. The components in biodiesel are generally methyl, ethyl, or higher alkyl esters. Numerous experimental and modeling studies have been carried out on combustion of methyl butanoate (n-$C_3H_7C(=O)OCH_3$) [3–8] and methyl decanoate (n-$C_9H_{19}C(=O)OCH_3$) [10–12], because kinetic models describing the combustion of these fuels are expected to be used as "building blocks" for describing combustion of biodiesel. Methyl decanoate is a high molecular weight ester. Kinetic models describing combustion of methyl butanoate [3–7] and methyl decanoate [10–12] have been developed and tested by comparison with experimental data obtained in shock tubes, rapid compression machines, flow reactors, and counterflow nonpremixed flames. These previous studies on methyl butanoate did not measure or predict critical conditions of extinction and autoignition in flow systems [3–8]. A previous experimental and kinetic modeling study was carried out on the combustion of methyl decanoate in nonpremixed, nonuniform flows [11]. Experiments were performed employing the counterflow configuration. Critical conditions of extinction and autoignition were measured.

The present, experimental study, is focused on characterizing key aspects of combustion of low molecular weight esters in nonpremixed nonuniform flows and thus pro-

viding data for kinetic modeling. Combustion processes in diesel engines closely resemble nonpremixed systems, and autoignition plays a key role. Critical conditions of autoignition and extinction are measured for nonpremixed combustion of methyl butanoate, methyl crotonate ($CH_3C=CH(C=O)OCH_3$), ethyl propionate ($C_2H_5C(=O)OC_2H_5$), n-heptane (n-C_7H_{16}), biodiesel (made from soybeans), and diesel. The volumetric composition of biodiesel employed in this study was (reported by the manufacturer) methyl palmitate (11 %), methyl sterate (4 %), methyl oleate (17 %), methyl linoleate (67 %), and methyl linolenate (1 %). The diesel was obtained from a local station. Experimental data is also obtained for a mixture of 20 % methyl butanoate and 80 % n-heptane by volume, because n-heptane was previously considered as a surrogate for diesel and studies on combustion of this mixture is expected to elucidate key aspects of combustion of mixtures of biodiesel and diesel. The knowledge obtained from studies on low molecular weight esters is expected to be building blocks for future studies on high molecular weight methyl esters. In addition, the present study provides fundamental knowledge on some key aspects of combustion of esters.

5.2   Experimental Procedures and Results

To capture the influence of the flow field on the critical conditions of autoignition and flame extinction, experiments are conducted in the counterflow configuration. Two types of configurations—the condensed fuel configuration (Section A.1.3) and the prevaporized fuel configuration (Section A.1.2), are employed. The condensed fuel configuration is particularly useful for studies on those liquid fuels that have high boiling points, for example biodiesel and diesel, where prevaporization, with negligible thermal breakdown, is difficult to achieve. In general, many liquid fuels can be tested in the condensed fuel configuration, while only those fuels with boiling points less than 600 K can be safely tested in the prevaporized fuel configuration. At higher temperatures, cracking of the fuel can take place. In the prevaporized fuel configuration, the mass fraction and mass flux of fuel in the fuel stream are independent variables under the control of the experimenter, while these quantities are dependent variables in the condensed fuel configuration and cannot be independently controlled by the experimenter. Thus the prevaporized fuel configuration allows experiments to be conducted over a wider range of parameters. Table 5.2 shows some relevant properties of the fuels tested here. It shows that the boiling point of biodiesel is between 626 K and 716 K.

Name	Chemical Symbol	Normal Boiling Point [K]	Molecular Weight [kg/mol]
Methyl Crotonate	$C_5H_8O_2$	392	0.1
Methyl Butaonate	$C_5H_{10}O_2$	375	0.102
Ethyl Propionate	$C_5H_{10}O_2$	372	0.102
Methyl Decanoate	$C_{11}H_{22}O_2$	497	0.186
n-Heptane	C_7H_{16}	372	0.1
Biodiesel	C:H:O= 19:36:2	626-716	0.294
Diesel	C:H = 16:26	448-623	0.218

Therefore, this fuel is tested in the condensed fuel configuration. The boiling point of all methyl esters tested here is less than 500 K. Therefore, these fuels can be tested in both configurations. In this work, biodiesel, diesel, and methyl butanoate are tested in the condensed fuel configuration. The other esters including methyl butanoate are tested in the prevaporized configuration. By comparing the combustion characteristics of methyl butanoate with biodiesel, and methyl butanoate with other esters it was possible to compare the combustion characteristics of all esters tested here with biodiesel.

5.2.1 Condensed Fuel Configuration

The detailed description of the counterflow burner used for carrying out experiments in the condensed fuel configuration is given elsewhere [13]. This burner has been successfully employed previously to carry out experiments on a wide variety of liquid fuels, including high boiling point fuels, jet fuels, and other multicomponent liquid fuels [13–15].

Figure A.4 shows a schematic illustration of the condensed fuel configuration and a detailed description is provided in Section A.1.3. Characteristics of the flowfield and boundary conditions are defined equal to the description provided in the Appendix A with a simplified characteristic strain rate equation Equation A.4.

Figure 5.1 shows a photograph of a methyl butanoate flame stabilized the condensed fuel configuration shown in Figure A.1(b).

The condensed fuel configuration shown in Figure A.1(b) is an open system because the fuel evaporating from the liquid-gas interface is continuously replenished from a reservoir. In experiments with fuel mixtures, where the boiling point of various components in the mixture is not the same, the concentration of the various components in the mixture on the liquid side of the liquid-gas interface will be different from that in the
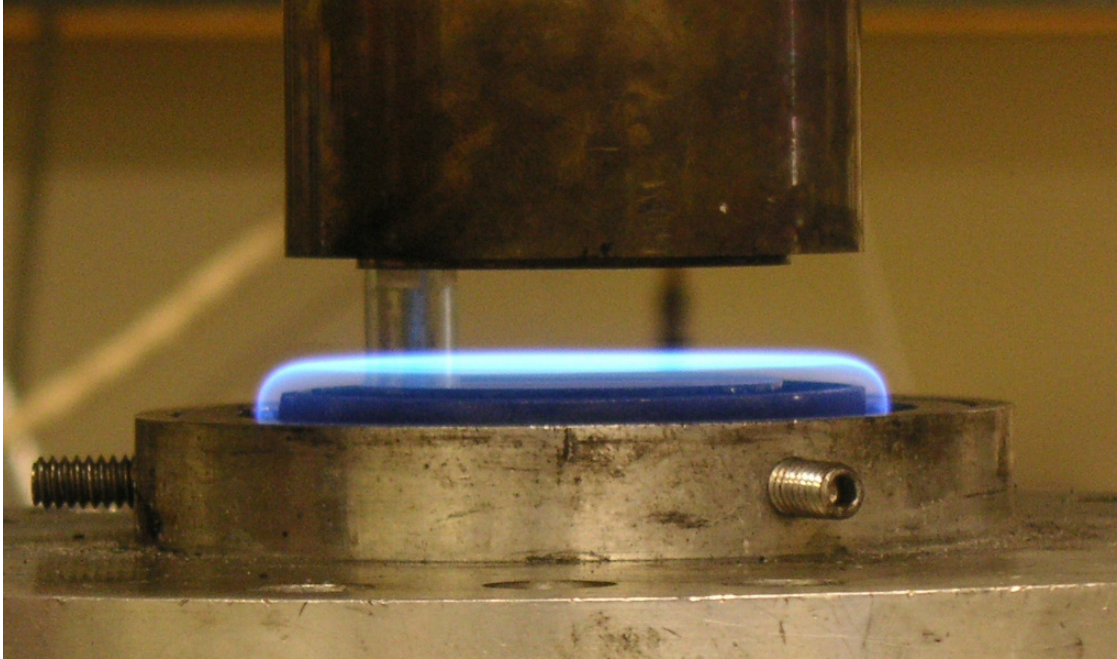
Figure 5.1: Photograph of a methyl butanoate flame stabilized in the condensed fuel configuration shown in Figure A.1(b)

reservoir. This would result in diffusion of various components of the fuel mixture in the liquid. After steady state has been achieved, the sum of the convective and diffusive flux of each component transported toward the liquid-gas interface will be proportional to its mass fraction in the reservoir. Therefore, on the gas side of the liquid-gas interface, the sum of the convective and diffusive flux of each component transported away from the interface will be also be proportional to its mass fraction in the reservoir. Accurate interpretation of experimental data obtained in the condensed fuel configuration is possible if the system attains steady state quickly. Previous studies on fuel mixtures have clearly demonstrated that extinction experiments can be performed employing the condensed fuel configuration because the system attains steady state quickly [15, 17, 18].

In the condensed fuel configuration, extinction experiments are performed with $T_2 = 298\,\mathrm{K}$, and $L = 10\,\mathrm{mm}$. At a given value of $Y_{\mathrm{O}_2,2}$, the velocity V_2 is increased until extinction takes place. The strain rate at extinction is calculated using Equation A.4. It is represented by $a_{2,\mathrm{E}}$. The experiments are repeated at different values of $Y_{\mathrm{O}_2,2}$. The accuracy of the strain rate is $\pm 10\,\%$ of recorded value and that of $Y_{\mathrm{O}_2,2}$ is $\pm 3\,\%$ of recorded value. The measurement repeatability of strain rate is $\pm 2\,\%$ that of $Y_{\mathrm{O}_2,2}$ is $\pm 2\,\%$, and temperature $\pm 1\,\%$.
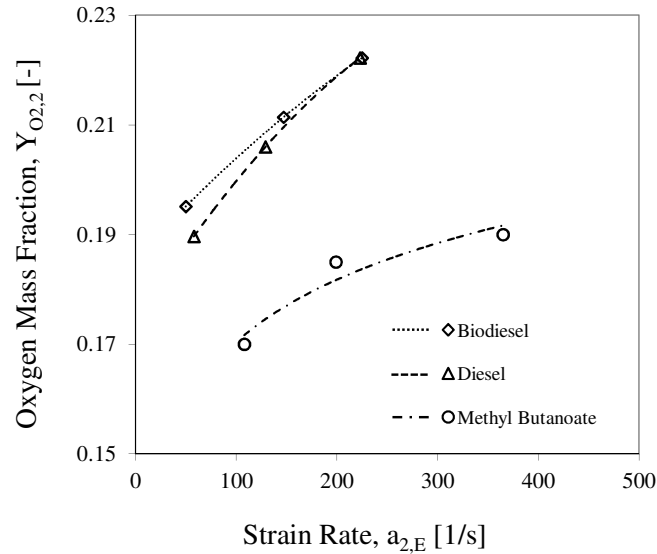
Figure 5.2: The mass fraction of oxygen in the oxidizer stream, $Y_{O_2,2}$ as a function of the strain rate at extinction, $a_{2,E}$. The symbols represent experimental data. The lines are best fit to the data. The experimental data was obtained in the condensed fuel configuration shown in Figure A.1(b)

Figure 5.2 shows $Y_{O_2,2}$ as a function of $a_{2,E}$ for biodiesel, diesel, and methyl butanoate. The symbols represent experimental data. The lines are best fit to the data. A line connecting the experimental data for any fuel represents a boundary. The region above the curve is flammable. Figure 5.2 shows that the critical conditions of extinction of biodiesel and diesel are nearly the same. At a given $Y_{O_2,2}$, the strain rate at extinction for methyl butanoate is higher than those for biodiesel and diesel. This indicates that under the conditions tested here, methyl butanoate is harder to extinguish than biodiesel and diesel.

In the autoignition experiments, the oxidizer stream is air and $L = 12\,\text{mm}$. Here, for a given value of the flow velocity of the oxidizer stream, V_2, its temperature, T_2, is increased until autoignition takes place. The value of T_2 at autoignition is represented by $T_{2,I}$. The value of the strain rate is calculated using Equation A.4. It is represented by $a_{2,I}$. The accuracy of the measurement of the temperature of air at autoignition is expected to be $\pm 30\,\text{K}$, that of the strain rate $\pm 10\,\%$. The experimental repeatability in the measurement of the temperature of air at autoignition is expected to be $\pm 6\,\text{K}$. Values of $T_{2,I}$ are measured for various a_2.

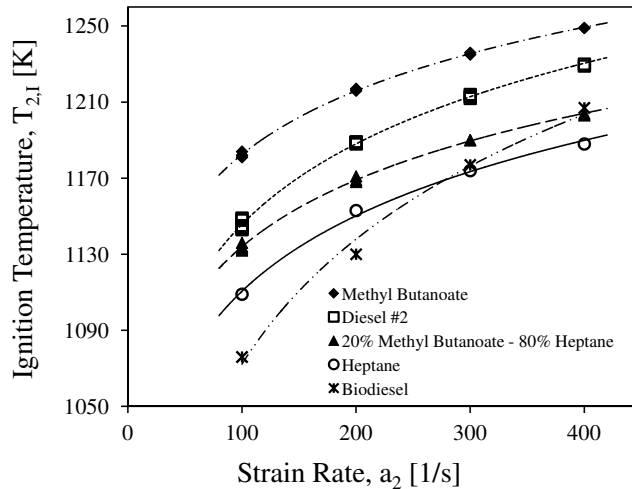Figure 5.3 shows measured critical conditions of autoignition for methyl bu-

Figure 5.3: Experimental data showing the temperature of air at autoignition, $T_{2,\mathrm{I}}$, as a function of the strain rate. The symbols represent measurements. The lines are best fits to the experimental data. The experimental data was obtained employing the condensed fuel configuration shown in Figure A.1(b).

tanoate, n-heptane, a mixture of 20 % methyl butanoate and 80 % n-heptane by volume, diesel, and biodiesel. The symbols represent measurements. For a given fuel, a curve connecting the symbols is a boundary. Autoignition does not take place in the region below this boundary. For all fuels tested, $T_{2,\mathrm{I}}$ increases with increasing a_2. For lower values of a_2, the value of $T_{2,\mathrm{I}}$ for methyl butanoate is the highest. Thus, at low values of a_2, methyl butanoate is most difficult to ignite followed by diesel, the mixture, n-heptane, and biodiesel. At higher values of the strain rate, biodiesel is more difficult to ignite than n-heptane.

5.2.2 Prevaporized Fuel Configuration

A schematic illustration of the the prevaporized fuel configuration shown in Figure A.3 and a detailed description is provided in Section A.1.2. Characteristics of the flowfield and boundary conditions are defined equal to the description provided in the Section A with a characteristic strain rate defined in Equation A.4 provided in Equation A.1.

Extinction experiments are conducted with $L = 10$mm, and $T_2 = 298$K. The temperature of the fuel stream, T_1, for methyl butanoate, methyl crotonate, and ethyl propionate are $453\,(\pm 10)$K, $448\,(\pm 10)$K, and $445\,(\pm 10)$K, respectively. The momenta
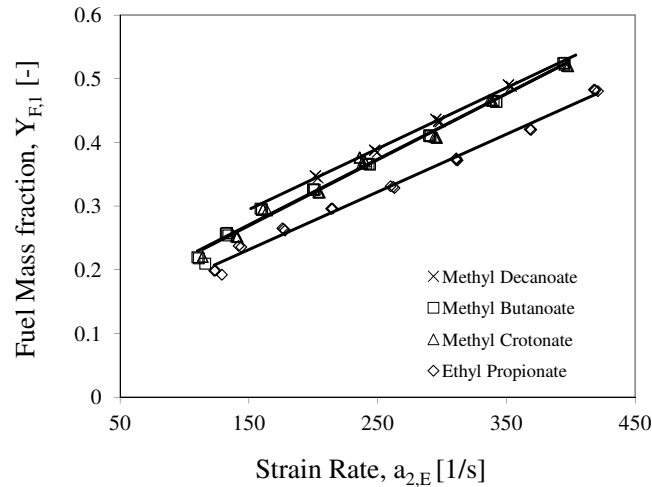
Figure 5.4: Experimental data showing the mass fraction of fuel in the fuel stream, $Y_{F,1}$, as a function of the strain rate, a_2, at extinction. The symbols represent measurements. The lines are best fits to the experimental data. The experimental data was obtained employing the prevaporized fuel configuration shown in Figure A.3. The experimental data for methyl decanoate was obtained from Reference [11].

of the counterflowing streams are balanced. Thus $\rho_1 V_1{}^2 = \rho_2 V_2{}^2$. At some selected value of $Y_{F,1}$, the flame is stabilized. The strain rate is increased by increasing V_1 and V_2 until extinction is observed. The accuracy of the measurement of the fuel mass fraction is $\pm 3\%$ of recorded value.

Figure 5.4 compares the critical conditions of extinction for various esters. It shows the mass fraction of fuel in the fuel stream, $Y_{F,1}$, as a function of the strain rate. The experimental data for methyl decanoate was obtained from Reference [11]. The critical conditions of extinction of methyl decanoate, methyl butanoate, and methyl crotonate are nearly the same. At a given value of $Y_{F,1}$ the value of a_2 at extinction for ethyl propionate is much larger than that for methyl decanoate. Therefore, ethyl propionate is much more difficult to extinguish when compared with the other esters. Comparison of the data in Figure 5.4 with those in Figure 5.2 shows that biodiesel, and diesel are less reactive than all the esters tested here.

Autoignition experiments are conducted with $L = 12$mm, and $Y_{F,1} = 0.4$. The temperature of the fuel stream, T_1, for methyl butanoate, methyl crotonate, and ethyl propionate are $433 \, (\pm 10)$K, $458 \, (\pm 10)$K, and $458 \, (\pm 10)$K, respectively. At chosen values of strain rate, the flow field is established. The temperature of air is increased until autoignition takes place. The temperature of the oxidizer stream at autoignition, $T_{2,I}$,
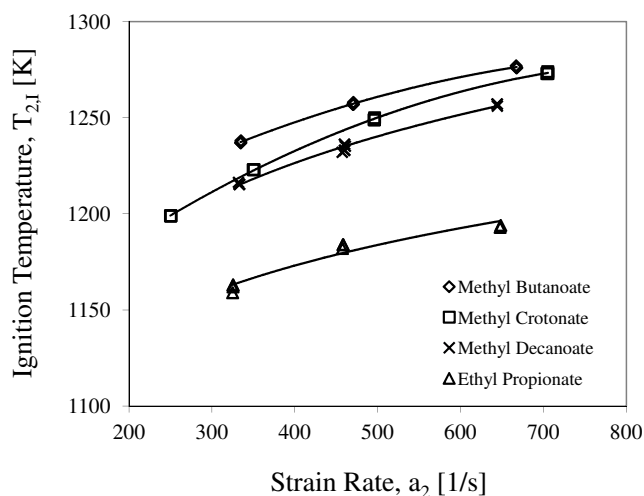
Figure 5.5: Experimental data showing the temperature of air at autoignition, $T_{2,\mathrm{I}}$, as a function of the a_2. The symbols represent measurements. The lines are best fits to the experimental data. The experimental data was obtained employing the prevaporized fuel configuration shown in Figure A.3. The experimental data for methyl decanoate was obtained from Reference [11].

is recorded as a function of the strain rate.

Figure 5.5 compares the critical conditions of autoignition for the esters. The experimental data for methyl decanoate was obtained from Reference [11]. Figure 5.5 shows that ethyl propionate is easiest to ignite followed by methyl decanoate, methyl crotonate, and methyl butanoate. Comparison of Figure 5.3 with 5.5 shows that at a given value of strain rate, methyl decanoate, methyl crotonate, and methyl decanoate are more difficult to ignite in comparison to biodiesel. Numerical calculations employing a reduced chemical-kinetic mechanism for methyl butanoate were performed, obtaining predictions for the condensed fuel and the prevaporized configuration [20]. Critical conditions of extinction and ignition were also obtained numerically for methyl decanoate in the prevaporized configuration, employing a detailed chemical-kinetic scheme. [11]

5.3   Concluding Remarks

The condensed fuel configuration is useful for experimental studies on those liquid fuels that have high boiling points. The autoignition temperature for biodiesel is very close to that for diesel. More research needs to be done to test how good surrogate fuels made up of low molecular weight hydrocarbons and esters can predict the combustion of

practical fuels such as diesel and biodiesel. For example, oxygenate compounds such as alcohols or ethers have generally lower cetane numbers than the corresponding straight chain hydrocarbons, which means they are harder to ignite in diesel engines. On the other hand, in certain nonpremixed combustion configurations, the diffusion of fuel to the reactions zone can be an important factor, and here, low molecular weight hydrocarbons and esters can cause ignition temperatures to be lower. These two offsetting factors can make low molecular weight hydrocarbon fuels and esters sometimes behave similar to larger practical fuels.

Acknowledgement

References

[1] C. Westbrook, W. Pitz, P. Westmoreland, F. Dryer, M. Chaos, P. Osswald, K. Kohse-Höinghaus, T. Cool, J. Wang, B. Yang, N. Hansen, and T. Kasper, *A detailed chemical kinetic reaction mechanism for oxidation of four small alkyl esters in laminar premixed flames*, Proceedings of the Combustion Institute 32 (2009), pp. 221–228.

[2] M.H. Hakka, P.A. Glaude, O. Herbinet, and F. Battin-Leclerc, *Experimental study of the oxidation of large surrogates for diesel and biodiesel fuels*, Combustion and Flame 156 (2009), pp. 2129–2144.

[3] C. Hayes and D. Burgess, *Exploring the oxidative decompositions of methyl esters: Methyl butanoate and methyl pentanoate as model compounds for biodiesel*, Proceedings of the Combustion Institute 32 (2009), pp. 263–270.

[4] S. Dooley, H. Curran, and J. Simmie, *Autoignition measurements and a validated kinetic model for the biodiesel surrogate, methyl butanoate*, Combustion and Flame 153 (2008), pp. 2–32.

[5] S. Gaïl, M. Thomson, S. Sarathy, S. Syed, P. Dagaut, P. Diévart, A. Marchese, and F. Dryer, *A wide-ranging kinetic modeling study of methyl butanoate combustion*, Proceedings of the Combustion Institute 31 (2007), pp. 305–311.

[6] E.M. Fisher, W.J. Pitz, H.J. Curran, and C.K. Westbrook, *Detailed Chemical Kinetic Mechanisms for Combustion of Oxygenated Fuels*, Proceedings of the Combustion Institute 28 (2000), pp. 1579–1586.

[7] S. Sarathy, S. Gaïl, S. Syed, M. Thomson, and P. Dagaut, *A comparison of saturated and unsaturated C_4 fatty acid methyl esters in an opposed flow diffusion flame and a jet stirred reactor*, Proceedings of the Combustion Institute 31 (2007), pp. 1015–1022.

[8] J.P. Szybist and A.L. Boehman, *Auto-Ignition Behavior of Methyl Decanoate*, American Chemical Society 50 (2005).

[9] P. Dagaut, S. Gaïl, and M. Sahasrabudhe, *Rapeseed oil methyl ester oxidation over extended ranges of pressure, temperature, and equivalence ratio: Experimental and modeling kinetic study*, Proceedings of the Combustion Institute 31 (2007), pp. 2955–2961.

[10] O. Herbinet, W.J. Pitz, and C.K. Westbrook, *Detailed chemical kinetic oxidation mechanism for a biodiesel surrogate*, Combustion and Flame 154 (2008), pp. 507–528.

[11] K. Seshadri, T. Lu, O. Herbinet, S. Humer, U. Niemann, W.J. Pitz, R. Seiser, and C.K. Law, *Experimental and kinetic modeling study of extinction and ignition of methyl decanoate in laminar non-premixed flows*, Proceedings of the Combustion Institute 32 (2009), pp. 1067–1074.

[12] O. Herbinet, W.J. Pitz, and C.K. Westbrook, *Detailed chemical kinetic mechanism for the oxidation of biodiesel fuels blend surrogate*, Combustion and Flame 157 (2010), pp. 893–908.

[13] K. Seshadri, S. Humer, and R. Seiser, *Activation-Energy Asymptotic Theory of Autoignition of Condensed Hydrocarbon Fuels in Non-Premixed Flows with Comparison to Experiment*, Combustion Theory and Modelling 12 (2008), pp. 831–855.

[14] A. Hamins, *The Structure and Extinction of Diffusion Flames*, University of California at San Diego, 1985.

[15] A. Hamins and K. Seshadri, *The structure of diffusion flames burning pure, binary, and ternary solutions of methanol, heptane, and toluene*, Combustion and Flame 68 (1987), pp. 295–307.

[16] K. Seshadri and F.A. Williams, *Laminar flow between parallel plates with injection of a reactant at high Reynolds number*, International Journal of Heat and Mass Transfer 21 (1978), pp. 251–253.

[17] A. Hamins and K. Seshadri, *Structure of Counterflow Diffusion Flames Burning Multicomponent Fuels*, in *Twentieth Symposium (International) on Combustion* The Combustion Institute, Pittsburgh, Pennsylvania, 1984, pp. 1905–1913.

[18] K. Seshadri, S. Humer, and R. Seiser, *Activation-Energy Asymptotic Theory of Autoignition of Condensed Hydrocarbon Fuels in Non-premixed Flows with Comparison to Experiment*, Combustion Theory and Modelling 12 (2008), pp. 831–855.

[19] R. Seiser, K. Seshadri, E. Piskernik, and A. Liñán, *Ignition in the Viscous Layer Between Counterflowing Streams: Asymptotic Theory with Comparison to Experiments*, Combustion and Flame 122 (2000), pp. 339–349.

[20] U. Niemann, R. Seiser, and K. Seshadri, *Ignition and extinction of low molecular weight esters in nonpremixed flows*, Combustion Theory and Modelling 14 (2010), pp. 875–891.

Chapter 6

Future Work

The work presented here is aimed at advancing the knowledge of combustion phenomena. New fuels, such as gases derived from biomass, are of rapidly emerging interest, and the extent to which such fuels can be used in the future as an alternative fuel will be influenced substantially by our understanding of their combustion chemistry. Mixtures of hydrogen, methane, and carbon-monoxide are also of primary interest. Experimental investigations into the auto-ignition behavior and elevated pressure investigations of natural gas, syngas, and producer gas combustion are of significant importance as more and more engines, that run on these fuels, are used for power generation. Regarding the combustion chemistry of these low molecular weight fuels at high pressure much work is left to cover the range for pressure conditions that can be found in practical applications. Of particular interest would be to investigate the range similar to the third explosion limit as found in a H_2/O_2 system. The findings from such studies could help in reducing engine knock and allow engine configurations based on the specific fuel mixture composition. As for liquid alternative transportation fuels, there is still only a limited amount of fundamental experimental work that is available and mostly focused on a small number of reactors. Counterflow studies on oxygenated fuels are rare, and for larger alcohols, studies investigating critical conditions are missing entirely. Useful future work along the lines of the present thesis would be worthwhile in reducing combustion uncertainties for these fuels. In addition, it would be of great interest to conduct investigations on the species and radical concentrations prior to auto-ignition to elucidate the decomposition of these types of fuel, since they are known for the formation of toxic pollutants.

Appendix A

Experimental Description

A.1   Counterflow Configuration

In a counterflow configuration (Figure A.1(a)), the duct exits are referred to as the fuel boundary and the oxidizer boundary. The mass fraction of fuel, the temperature, and the component of the flow velocity normal to the stagnation plane at the fuel boundary are respectively represented by $Y_{F,1}$, T_1, and V_1. The mass fraction of oxygen, the temperature, and the component of the flow velocity normal to the stagnation plane at the oxidizer boundary are respectively represented by $Y_{O_2,2}$, T_2, and V_2. The duct separation distance or distance between the fuel boundary and the oxidizer boundary is represented by L. Steady, axisymmetric, laminar flow of two opposing streams toward a stagnation plane is considered. The strain rate, defined as the normal gradient of the normal component of the flow velocity, changes from the fuel boundary to the oxidizer boundary. A characteristic strain rate on the oxidizer side of the stagnation plane a_2 is given by

$$a_2 = \left(\frac{2V_2}{L}\right)\left[1 + \frac{V_1\sqrt{\rho_1}}{V_2\sqrt{\rho_2}}\right] \tag{A.1}$$

Here, ρ_1 and ρ_2 represent the density of the mixture at the fuel boundary and at the oxidizer boundary, respectively. Equation A.1 is obtained from an asymptotic theory where the Reynolds numbers of the laminar flow at the boundaries are presumed to be large. [1]

The mixture fraction is a useful variable in combustion, often replacing spacial coordinates, in particular for diffusion flames. By changing the reactant concentrations not only the chemistry is affected, but the structure of the flame. Something easily
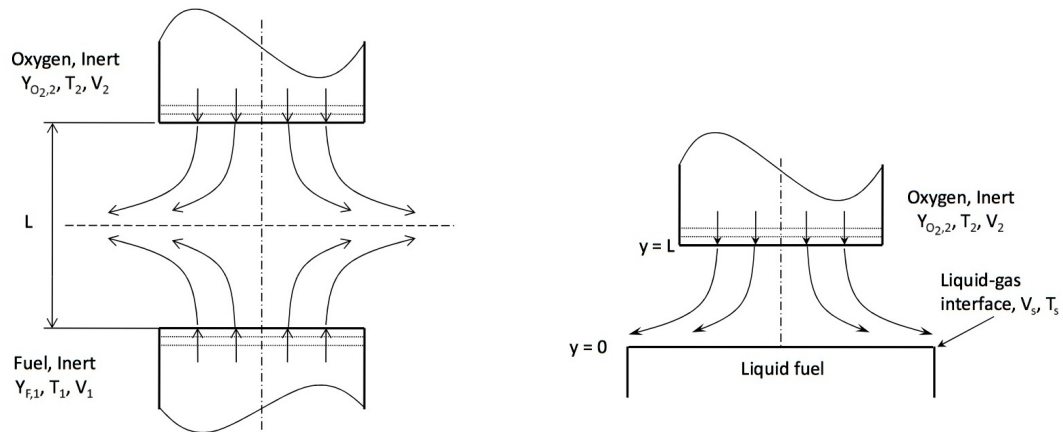
Figure A.1: Schematic illustrations of counterflow flowfields for the gaseous configuration (left) and for a gaseous oxidizer impinging on a liquid surface (right).

observed when employing the flamelet approach by Burke-Schumann, a simpified model that assumes constant c_p and where the temperature and the fuel, oxidizer, and product mass fraction are piecewise linear functions of Z. The proper interpretation of experimental measurements requires the minimization of changes in the same location. It is convenient to express the same position in terms of the mixture fraction Z, a conserved scalar quantity, which is defined as the elemental mass fraction originating from the fuel side at any location in the flow field. It follows from this defnition that Z = 1.0 in the fuel stream and Z = 0 in the oxidizer stream. The location of the flame-sheet, Z_{st}, where the flux of the fuel and the flux of oxygen are in stoichiometric proportions, is given by the stoichiometric mixture fraction, Z_{st} is [2–4]

$$Z_{st} = \left[1 + \frac{\nu Y_{F,1}}{Y_{O_2,2}} \right]^{-1} \tag{A.2}$$

where $Y_{F,1}$ and $Y_{O_2,2}$ are the mass fractions of fuel and oxygen at the exit of the ducts, W_F and W_O are their molecular weights, and ν is the stoichiometric mass ratio of oxygen to fuel.

A.1.1   Gaseous Reactant Configuration

Figure A.2 shows a schematic illustration of the counterflow burner employed for gaseous reactant experiments. Gaseous fuel is mixed with nitrogen and injected through
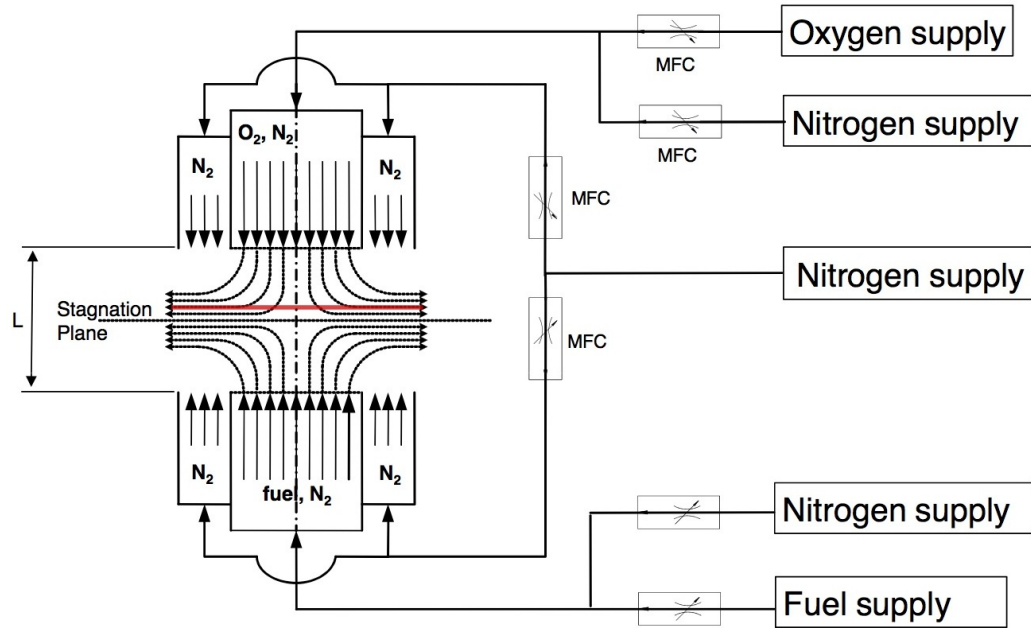
Figure A.2: Schematic drawing of the counterflow setup used in studies employing gaseous reactant streams

the lower nozzle. The oxidizer mixture is injected from the upper duct. Fine wire screens placed at the exit of the ducts, rectifying the flow are assuring steady laminar axisymmetric plug flow due to the negligibly small tangential component of the flow velocity at the boundaries. Hence the velocities of the reactants at the nozzle exits are presumed to be equal to the ratio of their volumetric flow rates to the cross-sectional area of the ducts. Conditions at the fuel boundary are represented by the subscript 1. Thus the mass fraction of fuel, temperature, and the flow velocity at the fuel boundary are $Y_{F,1}$, T_1 and V_1, respectively. Conditions at the oxidizer boundary are represented by the subscript 2. The mass fraction of oxygen, temperature, and the flow velocity at the oxidizer boundary are represented by $Y_{O,2}$, T_2 and V_2, respectively. The flow field describing parameter used in this study is the characteristic oxidizer strain rate which is defined as the gradient of the normal component of the flow velocity at the stagnation plane, on the oxidizer side. Due to the momentum balance of the opposing flows, $\rho_1 v_1^2 = \rho_2 v_2^2$, the strain rate is given by

$$a_2 = \frac{4V_2}{L} \tag{A.3}$$

where L is the distance between the fuel boundary and the oxidizer boundary, which is set to L=10 mm for all experiments. Two ducts with a diameter of 20 mm inject gaseous fuel and oxidizer in opposing directions to form a stagnation plane. Reactant flows are surrounded by an annular nitrogen curtain, improving flame stability, minimizing the influence of ambient gases on the reaction zone and improving flame quenching at the peripheral region of the reaction zone.

A.1.2   Prevaporized Fuel Configuration

Figure A.3 shows a schematic illustration of the prevaporized fuel counterflow system. Prevaporized fuel mixed with nitrogen is injected from the fuel-duct, and an oxidizer stream of air is injected from the oxidizer-duct. The distance between the fuel boundary and the oxidizer boundary is represented by L. The characteristic strain rate is defined similarily to the gaseous configuration. Critical conditions of extinction are measured with L=10 mm and autoignition with L=12 mm. The velocities of the reactants at the boundaries are presumed to be equal to the ratio of their volumetric flow rates to the cross-sectional area of the ducts. The temperature of the fuel stream and the temperature of the oxidizer stream at the boundaries are measured using thermocouples. The flow rates of gases are adjusted by computer-regulated mass flow controllers. The flow lines are heated to prevent condensation. Liquid fuels are supplied to the vaporizer with a high precision syringe pump, which allows the exact determination of liquid flow rates. The liquid fuel evaporates as it is admitted into the vaporizer through a nozzle. The vaporizer chamber is filled with hot nitrogen, which is maintained at a defined temperature and closely monitored with thermocouples. The products of combustion are evacuated into a region around the fuel-duct. Here they are cooled by water sprays. A curtain flow of nitrogen is introduced from concentric tubes placed outside the reactant ducts.

A.1.3   Liquid Pool Configuration

In a liquid pool burner, the flame is stabilized over the surface of a liquid fuel as shown in Figure A.1(b). An oxidizing stream is injected from the upper duct, impinging on the stream of evaporating fuel from the pool surface. A stagnation plane is formed slightly above the pool surface. The flame positions itself above the stagnation plane on the oxidizer side.
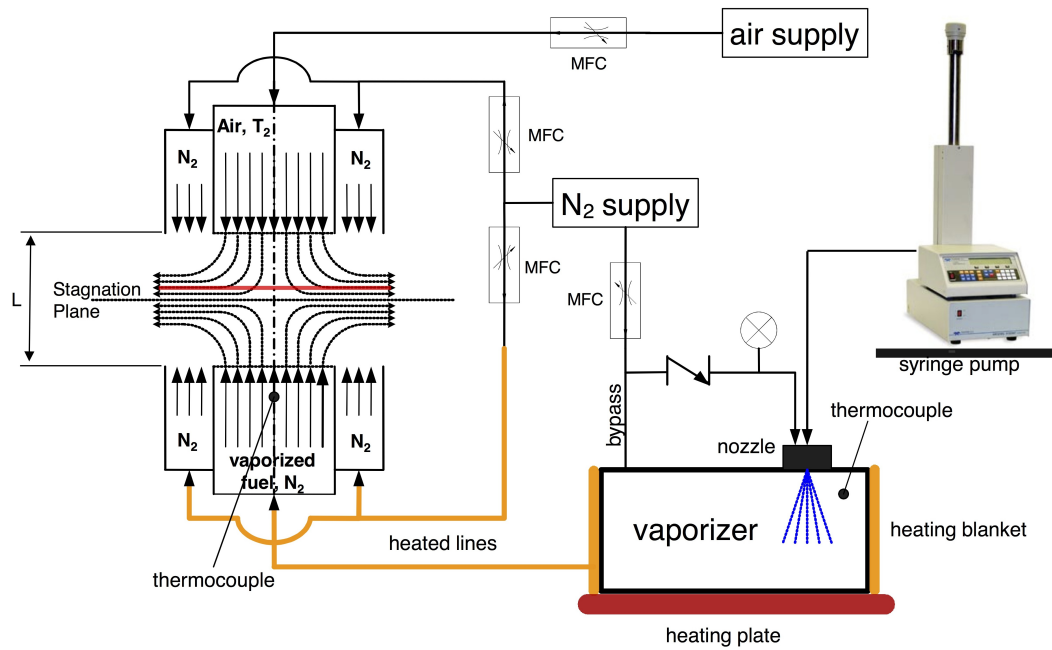
Figure A.3: Schematic drawing of the counterflow setup used in studies employing a prevaporized fuel stream. Liquid fuel is injected by a syringe pump into the vaporizer after which the gaseous fuel/nitrogen mixture is injected into the counterflow flowfield through the lower duct.

An axisymmetric stagnation-point flow of a gaseous oxidizer stream over the surface of an evaporating pool of a liquid fuel is considered. The oxidizer stream is a mixture of oxygen (O_2) and nitrogen (N_2). It is injected from the oxidizer-duct. The exit of the oxidizer-duct is the oxidizer boundary. Fine mesh wire screens are placed at the exit of the oxidizer-duct. As a consequence, the radial component of the flow velocity is zero at the oxidizer boundary. This allows the use of no-slip boundary conditions (plug flow boundary conditions). The origin is placed on the axis of symmetry at the surface of the liquid pool. The distance between the surface of the liquid pool and the oxidizer boundary is L. At the oxidizer boundary, the injection velocity is V_2, the temperature T_2, the density ρ_2, and the mass fraction of oxygen $Y_{O_2,2}$. Here, the subscript 2 represents conditions at the oxidizer boundary. The magnitude of the injection velocity, V_2, is estimated from the ratio of the measured volumetric flowrate of the oxidizer stream and the cross-sectional area of the oxidizer-duct. The temperature at the liquid-gas interface is T_s, and the mass averaged velocity on the gas side of the liquid-gas interface is V_s.

Here, subscript s represents conditions on the gas side of the liquid-gas interface. It has been shown by use of asymptotic analysis [5] that the radial velocity on the gas side of the liquid-gas interface is small and can be set equal to zero. Asymptotic analysis of the flow field in the limit of large values of the Reynolds number at the oxidizer boundary was carried out previously [1]. The analysis shows that a thin boundary layer is established at the surface of the liquid pool. The inviscid flow outside the boundary layer is rotational. The local strain rate, a_2 at the stagnation plane is given by [1, 5].
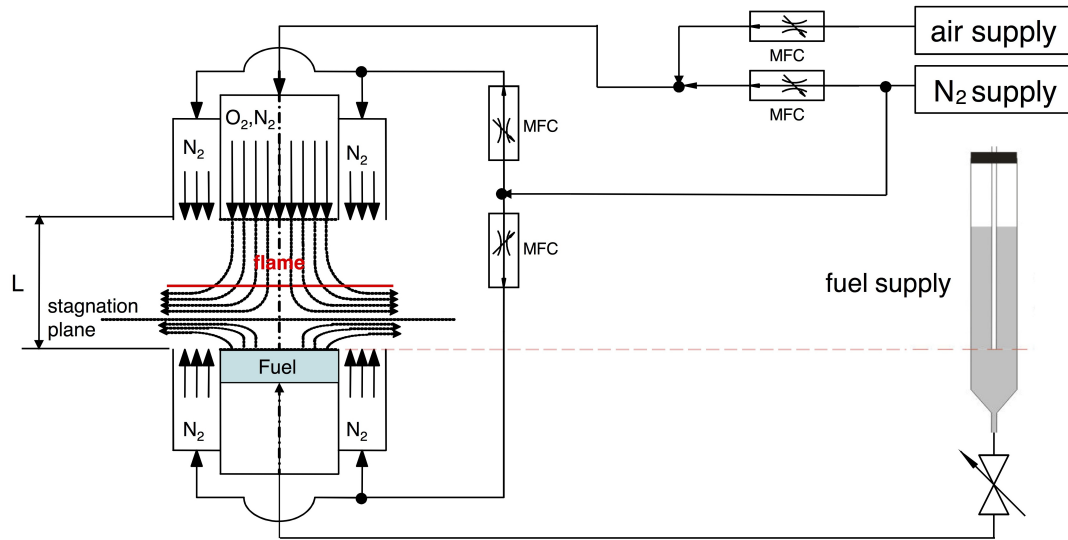
$$a_2 = 2V_2/L \qquad \qquad (A.4)$$

Figure A.4: Schematics of the liquid pool counterflow configuration employing a self-leveling fuel supply system

Figure A.4 shows a schematic illustration of a liquid pool counterflow configuration. Experimental conditions are similar to general description of the counterflow configuration, presuming laminar, axissymmetric flows with negligible tangential exit velocities. The strain rate, used to characterize the flow field, can be determined by the aforementioned formulation of Equation A.1 but simplifies to

$$a_2 = \frac{2V_2}{L}$$

due to momentum balance and the shift of the stagnation plane just short of the pool surface.

A.1.4 Autoignition Configuration

In auto-ignition experiments, the oxidizer stream is heated by a helix-shaped silicon-carbide resistance element. The oxidizer and curtain ducts consist of two concentric quartz tubes, which are fused together at the top. The inner diameter of the inner tube is 27 mm. To achieve a homogeneous plug flow with a flat exit velocity profile three screens are installed at the exit of the duct. The screens and retaining-rings are made of Inconel. The temperature of the heating element can be varied by adjusting the voltage provided by a variable transformer, reaching temperatures close to 2000 K. The heating element has to be centered precisely, to achieve an axissymmetric flow. The duct is covered with soluble refractory fiber insulation (Insulfrax) to prevent heat loss to the surrounding. A ring-shaped curtain introduces nitrogen. The exit diameter of the oxidizer with inserted rings is 24.5 mm. The oxidizer duct is aligned and centered to the fuel duct with three vertically adjustable bolts to an exact duct separation of 12 mm.

References

[1] K. Seshadri and F. A. Williams. Laminar flow between parallel plates with injection of a reactant at high Reynolds number. *International Journal of Heat and Mass Transfer*, 21(2):251–253, 1978.

[2] F. A. Williams. *Combustion Theory*. Addison-Wesley Publishing Company, Redwood City, CA, 2 edition, 1985.

[3] A. Liñán and F. A. Williams. *Fundamental Aspects of Combustion*, Volume 34 of *Oxford Engineering Science Series*. Oxford University Press, New York, 1993.

[4] N. Peters. Local quenching due to flame stretch and non-premixed turbulent combustion. *Combustion Science and Technology*, 30:1–17, 1983.

[5] K. Seshadri, S. Humer, and R. Seiser. Activation-energy asymptotic theory of autoignition of condensed hydrocarbon fuels in non-premixed flows with comparison to experiment. *Combustion Theory and Modelling*, 12(5):831–855, 2008.

Appendix B

High Pressure Combustion Facility

The objective was to construct a High Pressure Combustion Experimental Facility (HPCEF) for carrying out combustion experiments at pressures up to 25 bar. Although the facility is initially used for studies of combustion processes in non-uniform flow fields employing counterflow burners, it will be possible to house many different types of burners inside the pressure chamber. The HPCEF is therefore a versatile facility that can be employed for experimental studies on non-premixed, premixed and partially premixed combustion for gaseous, spray and liquid combustion. For the work presented here the counterflow burner placed inside the pressure chamber is optimized to facilitate experiments on gaseous non-premixed combustion. Design and procedures for the HPCEF are targeted towards measurements that include critical conditions of flame extinction and temperature profiles. A schematic drawing of the setup is provided in Figure B.2 and photographs provided in the Section B.6. Several sub-systems that make up the HPCEF, namely a pressure chamber, the burner assembly, the gas flow system, auxiliary systems and the control and data acquisition unit are described in the following sections.

The stainless steel main chamber of the HPECF measures 40 inches from top to bottom and has a diameter of 16 inches with a wall thickness of 3/8 inch. Four perpendicular view-ports employing fused silica windows allow optical access to the chamber inside. The windows measure 10 inches in diameter and one inch in thickness. They are kept in place each by a flange assembly with ten 5/8 inch machine hex bolts. During
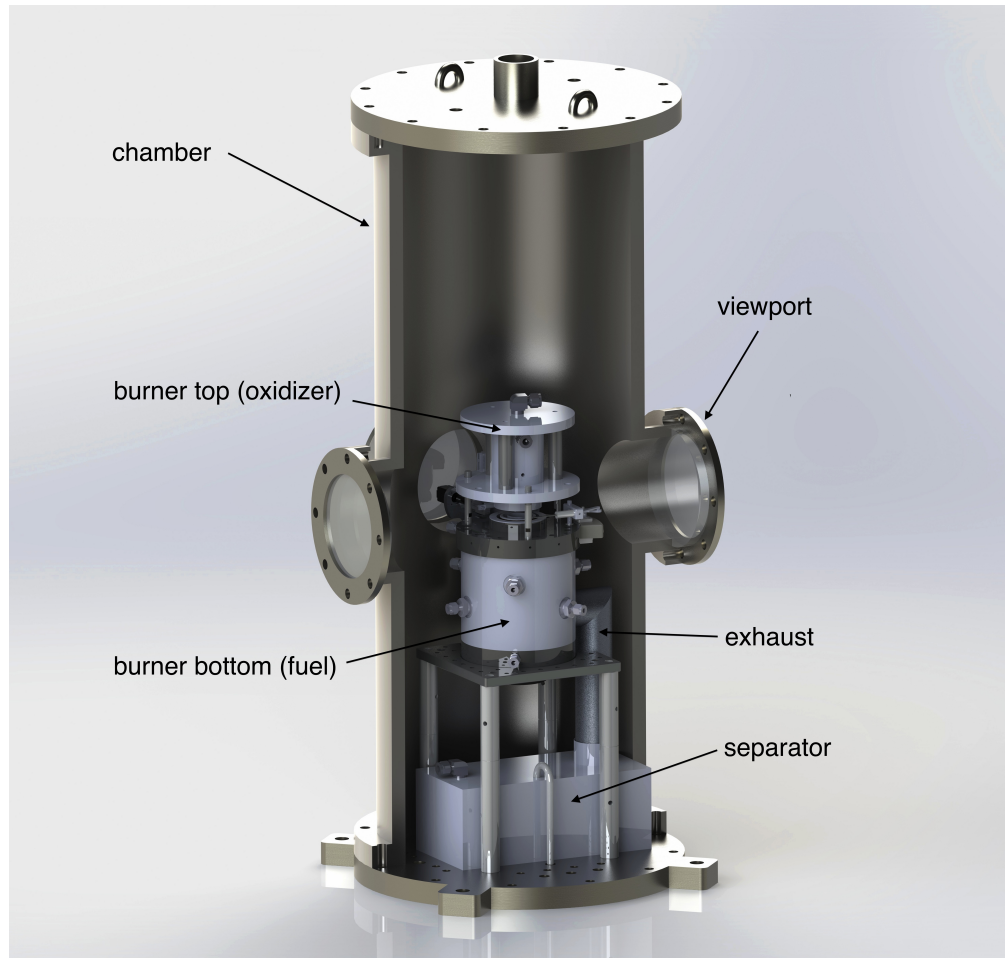
Figure B.1: CAD cross-section rendering of the HPCEF pressure chamber revealing the burner assembly inside.

the testing phase the center-point deflection of a half inch window was measured at 45 atm. It was concluded that the inner edge of the flange holding the window is a possible breaking edge. As a preventive measure a 1/8 inch thick neoprene collar is employed on the atmospheric side, covering the flange's edge. O-rings on the pressure side are sufficient to seal the window. The operating pressures reached inside the chamber require the glass windows to be strengthened through a special tempering process. However, due to the heat treatment, if the glass breaks, it will break into small pieces instead of simply cracking. Combined with pressurized gas these "projectiles" pose severe danger to human health. Hence several layers of redundant safety measures are put in place. First the gas supply regulators are limited to a pressure that is below the maximum safe operating pressure limit. If a regulator were to fail, a relief valve is installed that cracks
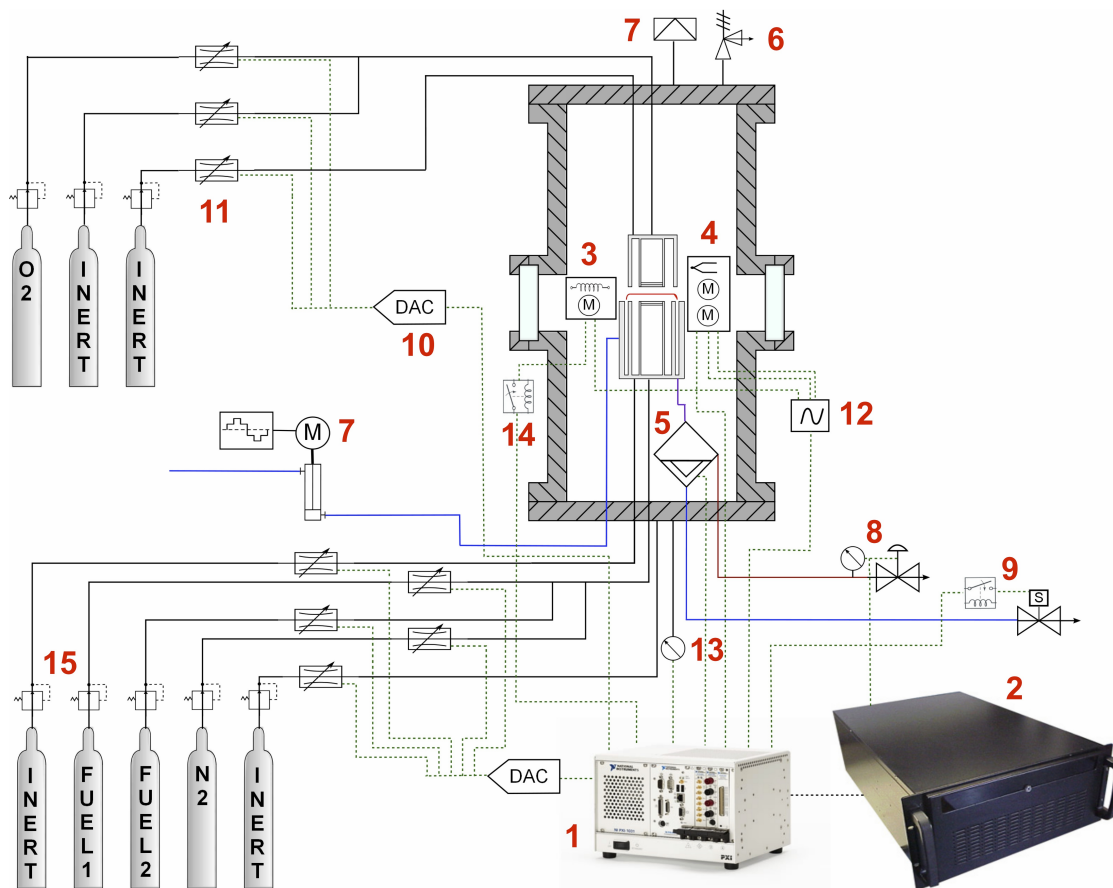
Figure B.2: Schematic drawing of the High Pressure Combustion Experimental Facility. 1-NI PXI system, 2-Computer, 3-igniter assembly, 4-thermocouple stage, 5-separator, 6-relief valve, 7-explosion vent, 8-PID backpressure regulator, 9-solenoid drain valve, 10-digital-analog-converter, 11-mass flow controller, 12-stepper drive, 13-pressure transducer, 14-solid-state relay, 15-pressure regulator

open once the pressure limit is reached, discharging excess gas. In case of a rapid rise of pressure a burst disk assembly (Oseco) with a two inch vent opening is installed at the top lid of the chamber. In addition a cubicle of high-impact poly-carbonate surrounds the chamber protecting from broken glass, while still giving optical access to the chamber. Throughputs for gas flow lines and electrical wiring are placed in the bottom of the chamber. This way the chamber can be lifted with an electrical hoist and the inside accessed without disconnecting lines. The chamber pressure is controlled by balancing the inflow of reactants and nitrogen, as a safe, inert pressurization medium, with the outflow of exhaust gases and excess nitrogen from the chamber. In experiments demanding constant pressure at high precision an electronic PID back-pressure regulator

(Tescom ER3000 mounted on an air loaded regulator) is employed. If fast response is required pressure control of the rig can be switched to a manually adjustable mechanical back-pressure valve. The chamber pressure is independently monitored and recorded with digital pressure transducers with an accuracy within 0.1 psi.

B.1   Burner

The counterflow burner placed inside the pressure chamber is a modified version of the design previously employed in atmospheric investigations described in Section A.1. This burner is optimized to facilitate experiments on gaseous non-premixed combustion. Two ducts with a diameter of 20 mm inject gaseous fuel and oxidizer in opposing directions. Reactant flows are surrounded by an annular nitrogen curtain, with an decreased cross section area to reduce gas consumption. The top (oxidizer) section as shown in Figure B.3 employs three mesh 200 stainless steel wire screens at the oxidizer duct exit and a ring shaped ceramic honeycomb at the curtain exit to rectify the respective gas streams. Optimal duct lengths and inlet fitting positioning were obtained from CFD simulations. In addition to the fuel and curtain duct an annular exhaust duct is located in the bottom section of the burner (Figure B.3), through which combustion products are removed from the reaction zone. This keeps hot gases and water vapor from accumulating inside the chamber, thus preventing a rise in chamber temperature and window fogging. Vapor content in the exhaust gas can form droplets in the expansion section of the back-pressure valve, causing pressure fluctuations and subsequently sensor problems. Condensate is therefore removed from the exhaust gas in a two-stage system. First the burner body is actively cooled as well as water is sprayed through stainless steel cone and fan pattern nozzles (Bete 1/8" PJ20, NF01120) onto the hot exhaust gas. After leaving the burner body through an aluminum duct, which allows further cooling the water gas mixture ends up in a separator unit. There the gas is evacuated continuously from the top to the back-pressure valve. The water accumulates in the bottom and is drained with a snorkel through a separate solenoid valve. The water level inside the separator is monitored with buoyant swing-arm reed switches (Omega). The water level is kept high enough so that gas does not drain through the water oulet, but low enough that water will not drain through the gas outlet. Both would cause severe pressure fluctuations inside the chamber. A boolean function VI fully automatically triggers the solenoid valve maintaining proper water levels.
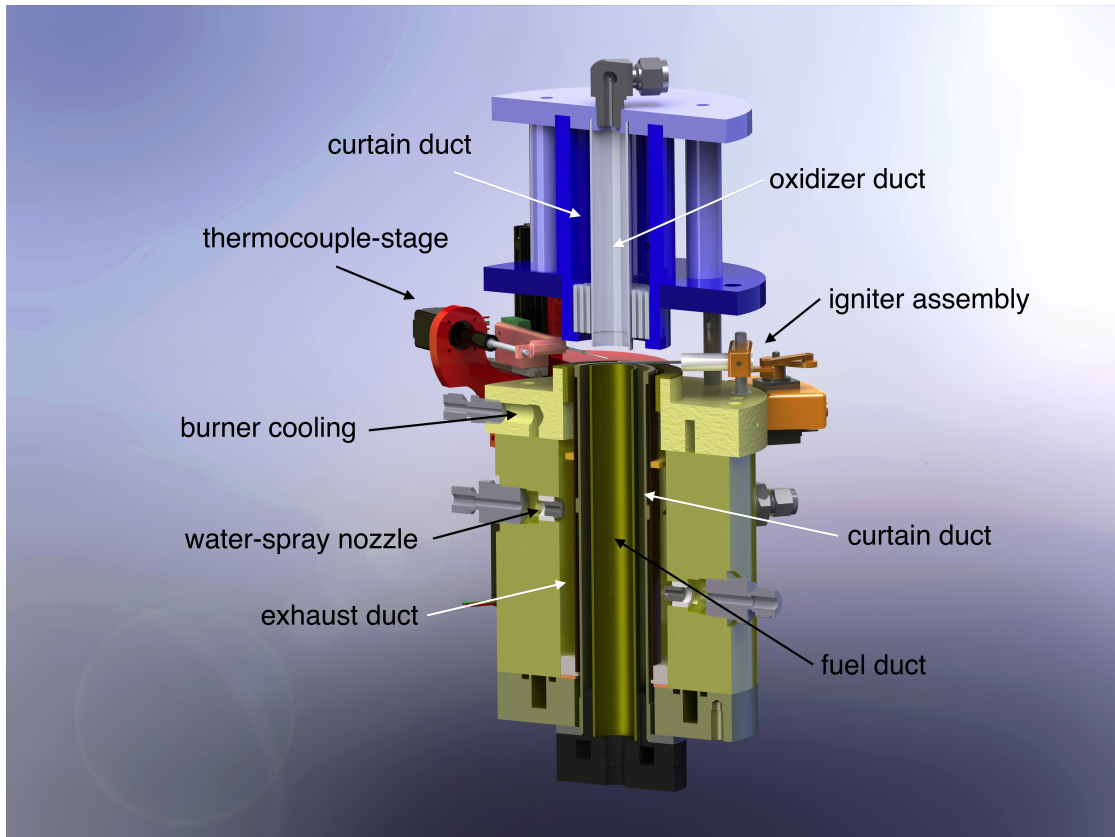
Figure B.3: CAD rendering of the entire burner assembly showing the fuel (lower) and oxidizer (upper) sections

Retractable ignition sources are indispensable in burners where experimental accuracy depends strongly on the quality of the flow field. To guarantee an unobstructed flow field after the flame is established, a remotely controlled stepper motor, which positions a 120 V silicon-carbide surface igniter, is employed. Power to the igniter is supplied via a 9 V activated solid state relay. Figure B.4 shows the igniter assembly with delrin pieces made to specification in a rapid-prototyping 3D printer.

Similarly customized mounting parts for the thermocouple XY-stage were made (Figure B.5). The vertical movement is achieved with a stepper-motorized linear slide rail, while the horizontal movement is achieved with a linear stepper actuator (both Haydon Kerk) and a custom built slide thermocouple mount. These linear rails feature wear-compensating, anti-backlash technology that insures repeatable and accurate positioning within a fraction of a micron. Stepper motors are indispensable for high pressure operation due to the simplicity of the design which only employs coils and magnets.
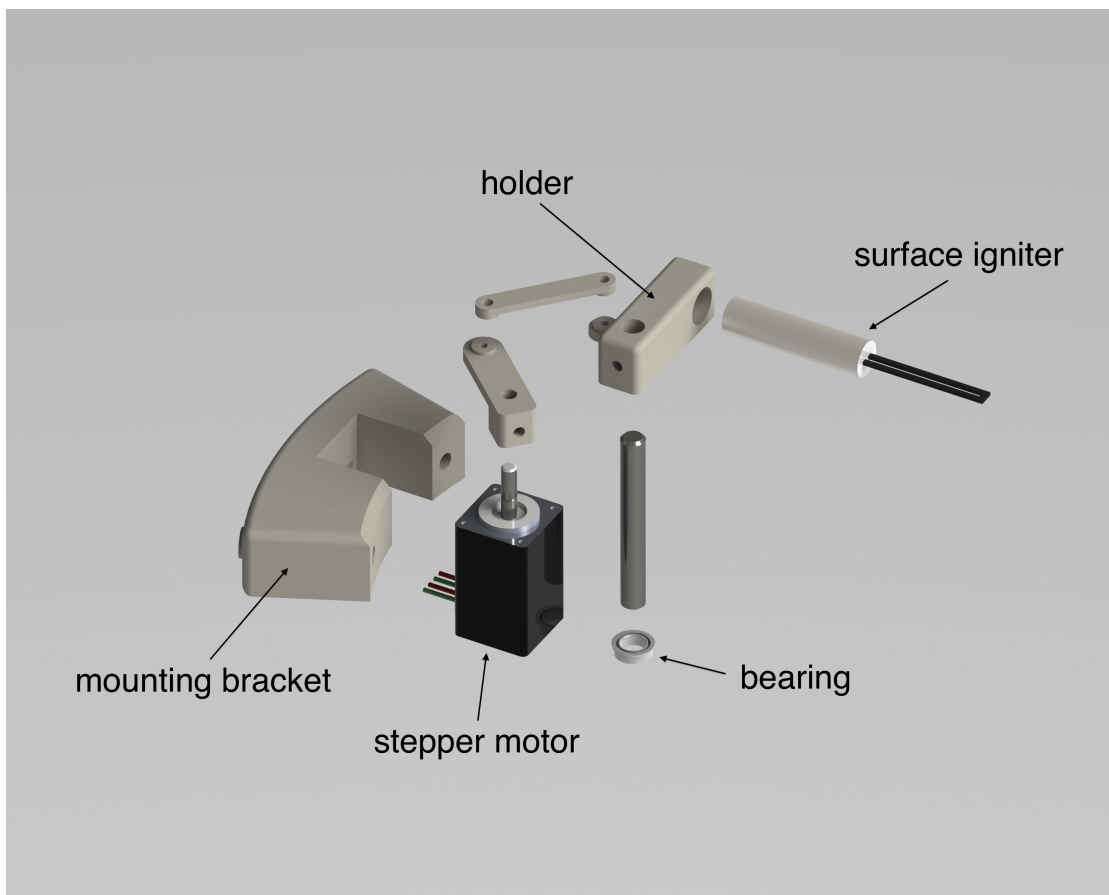
Figure B.4: Exploded-view CAD rendering of the igniter assembly used in the HPCEF to establish flames at elevated pressures.

Electronic parts like capacitors that are employed in servo motors are not able to withstand any pressure increase. Controller parts like stepper drivers and motion controller cards are kept outside the chamber and the signal is sent through shielded wires.

B.2   Gas Flow System

Gases for the HPCEF are stored in standard pressurized gas cylinders and supplied through manifolds for multiple cylinders. High pressure regulators for each gas line assure constant supply pressure of 500 psi independent of flow rate to each mass flow controller. These analog computer regulated mass flow controllers achieve precise control of flow rates to the setup independent of downstream pressure covering maximum flow rates in a range of 30 to 500 slm and pressures up to 450 psi. Each mass
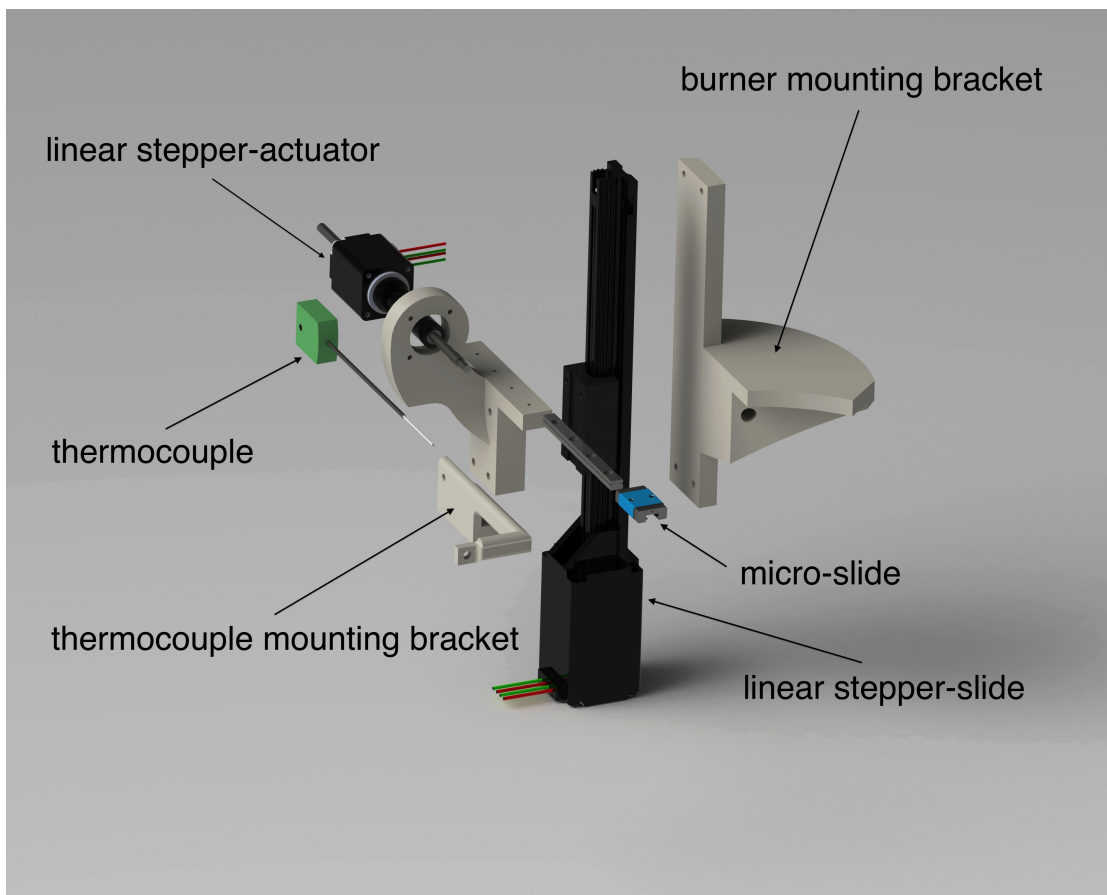
Figure B.5: Exploded-view CAD rendering of the XY-stage assembly used in the HPCEF for flame temperature measurements.

flow controller is specifically selected depending on the required experimental range and accurately calibrated using a Ritter (TG-50) pulse generating wet-test gas flow meter. Calibration for elevated pressures was achieved by back-pressuring the mass flow controller and measuring the flow volume of the gas at atmospheric conditions. Through horizontal mounting, in order to avoid natural convection inside the device due to the high gas density, pressure dependent inaccuracies of the mass flow controllers were found to be negligible. Overall, for given experimental conditions, the flow dependent accuracy of the employed mass flow controllers was within 1%.

B.3 Control and Data Acquisition Unit

A quad-core processor industrial computer equipped with a National Instruments PXI system is used as a central control and data collection unit. Several Virtual Instruments running on a Labview platform allow multiple processes to be integrated into one customized control panel. The PXI system features a multifunction digital/analog I/O data acquisition (DAQ) board, an RS-232 card, a high precision temperature logger and a four channel motion controller card connected to microstepping drivers. Mass flow controller serial communication is routed through the PXI system while only set-points are communicated through an RS-485 connection to the pressure valve PID controller. In case of a computer crash the embedded processors in the respective units are still able to perform necessary computations safely maintaining the current pressure and flow conditions. Operations performed by the computer control unit are pressure and temperature logging, water level sensing, solenoid valve and solid state relay actuation, gas flow regulation, PID communication, video/ image capture and motion control. All inputs are merged and immediately processed in a single control panel VI. (Figure B.6) Set-points are continuously updated to maintain the desired experimental conditions without additional input by the investigator.

B.4 Auxiliary System

Cooling water to cool the burner body is supplied from the in-house chilled water system. For the water sprays a special reciprocating piston pump (Hydra-cell) is mounted on a 1.5 kW three-phase electric motor. The installation of a pulsation dampener minimizes pressure waves, thus diminishing the risk of water hammer.

B.5 Procedure

Experimental conditions are established, controlled and recorded remotely through the control interface. At the beginning of the experiments, the chamber is filled with nitrogen to the desired operating pressure. When pressure conditions are reached, the flow field is established by introducing the reactants into the counterflow burner at the desired flow rates. After establishing a steady flame the strain rate is increased, while keeping momentum balance, until flame extinction takes place. Increments to increase
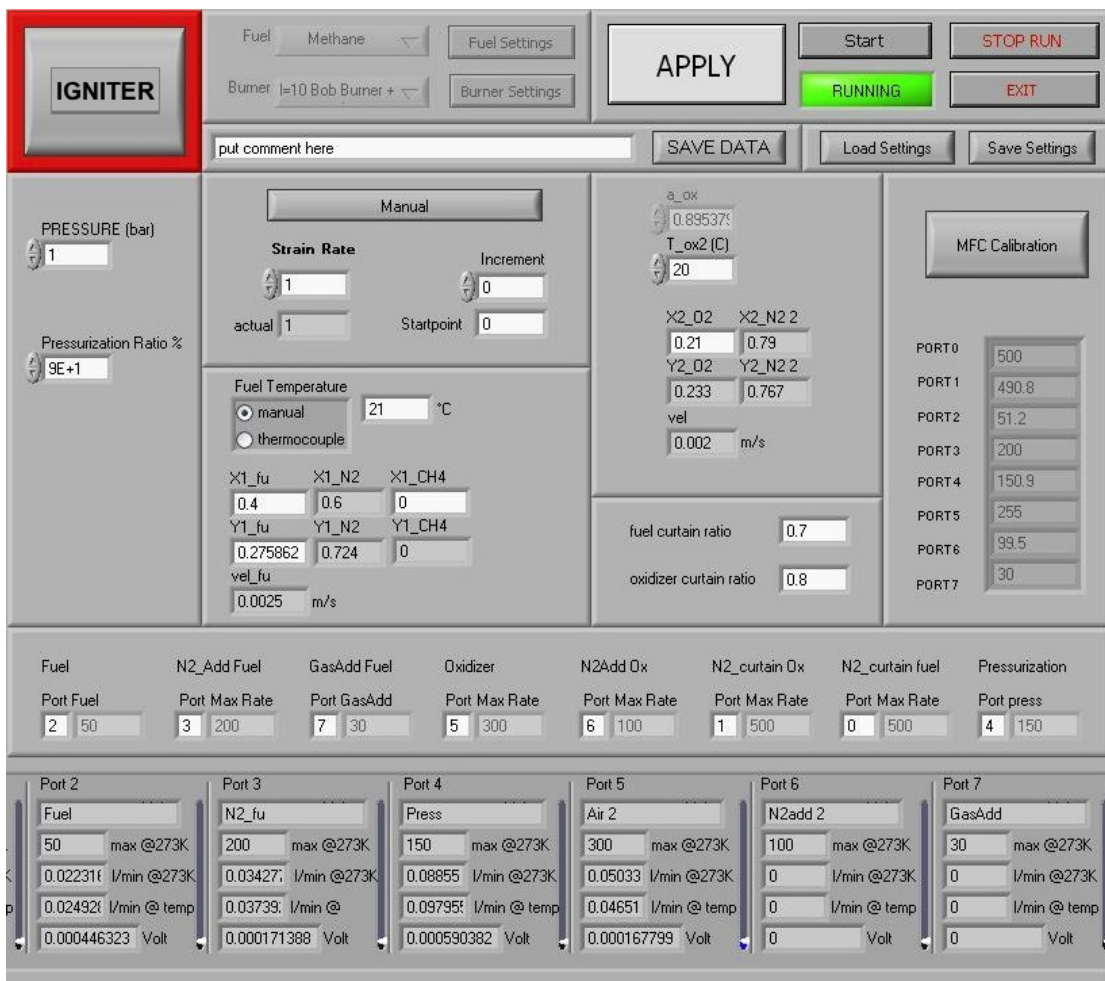
Figure B.6: Screenshot of the front panel of the Labview VI used for HPCEF control and data acquisition purposes.

the strain rate are selected to be sufficiently small and separated by enough time so that steady state is achieved after each step. Tests were performed, to ensure that stepping inflicted flow perturbation is not the cause for flame extinction. The flow rates and hence the strain rate at extinction are recorded as a function of pressure and composition of the reactants. Adiabatic flame conditions are intact throughout the experiments due to the constant location of the stagnation plane equidistant to both nozzles. Buoyancy effects can be neglected due to the high flow velocities. Thermocouples are mounted on the XY-stage. The probe is programmed to move vertically at a radial distance of 3 mm from the axis of symmetry. The flame is approached from the bottom covering a total distance of 7 mm. The probe then approaches the flame from the top in a similar

manner. This method was used to rule out previously reported effects of flame shift due to the presence of the thermocouple. The exact location of the thermocouple bead is determined in the beginning of the experiments with a digital SLR camera. Due to the precision of the employed rails subsequent positioning is achieved with the controller software.

B.6 Photographs

Figure B.7: Photograph of the HPCEF control station, showing the control and data acquisition unit (left) and the mass flow controller bench (right).
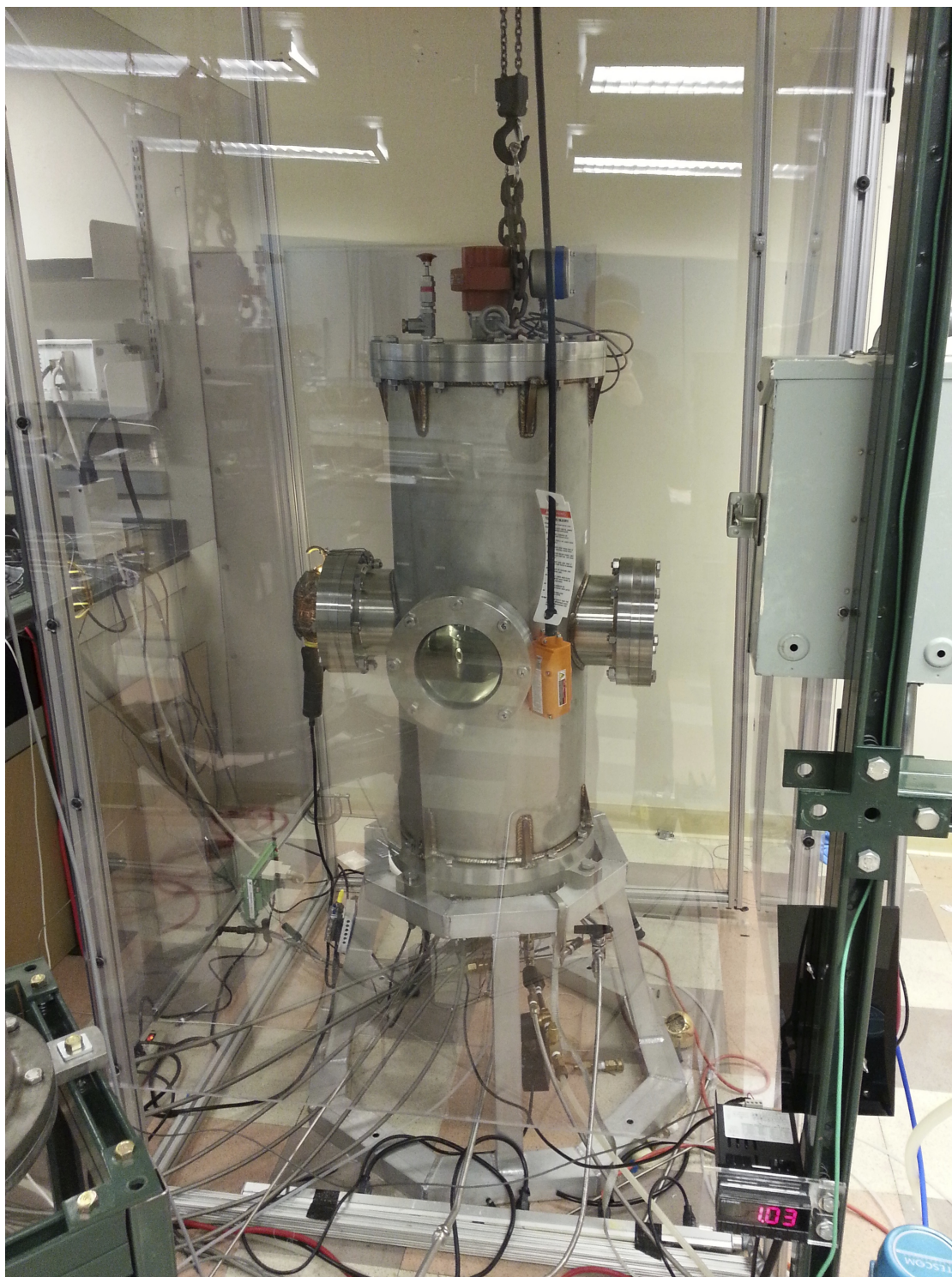
Figure B.8: Photograph showing the pressure chamber of the HPCEF with gas feed lines connected to throughputs in the bottomplate.

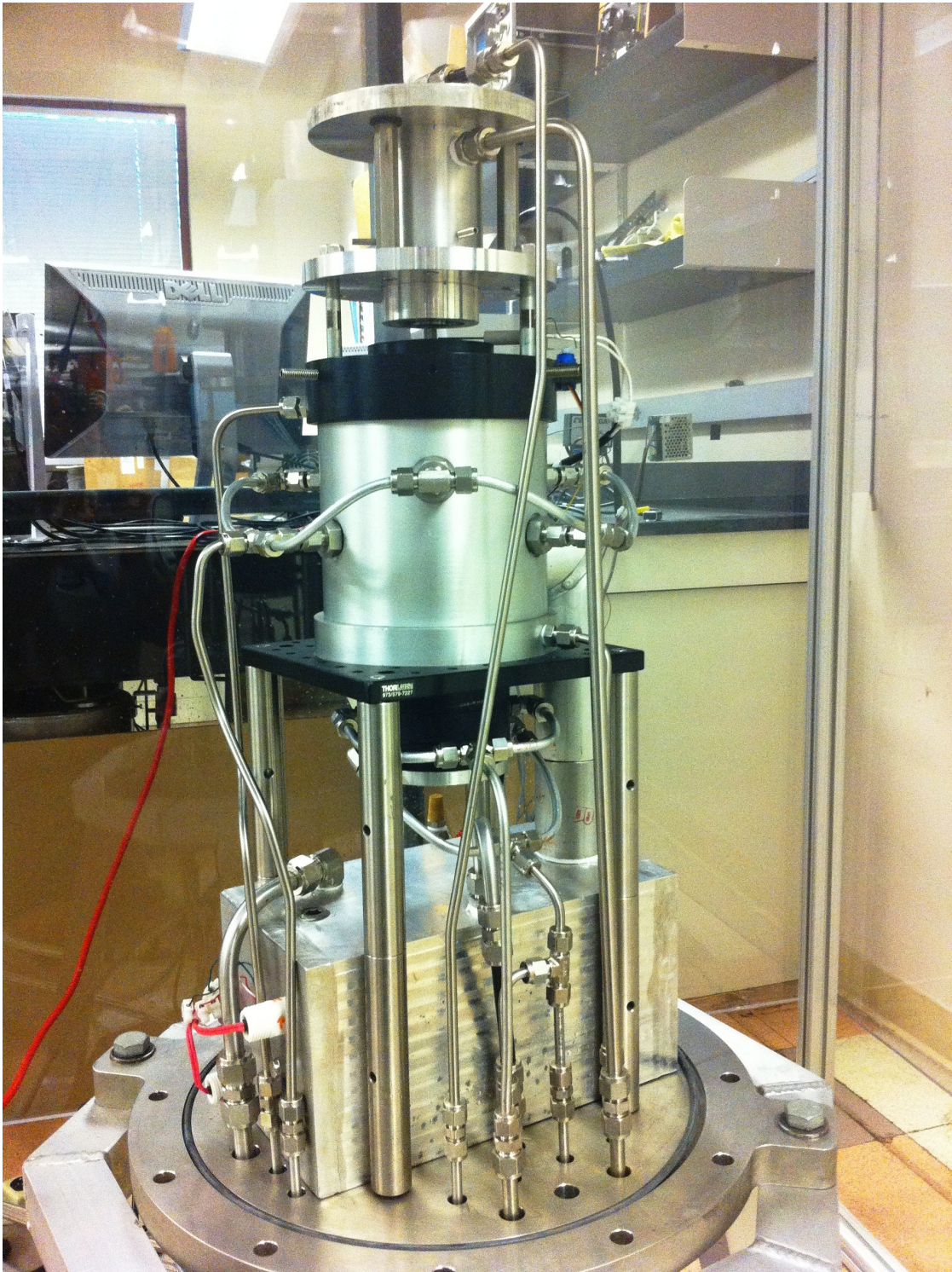**Figure B.9**: Photograph of the entire High Pressure Combustion Experimental Facility

Figure B.10: Photograph of the inside of the pressure chamber equipped with the counterflow burner configuration.
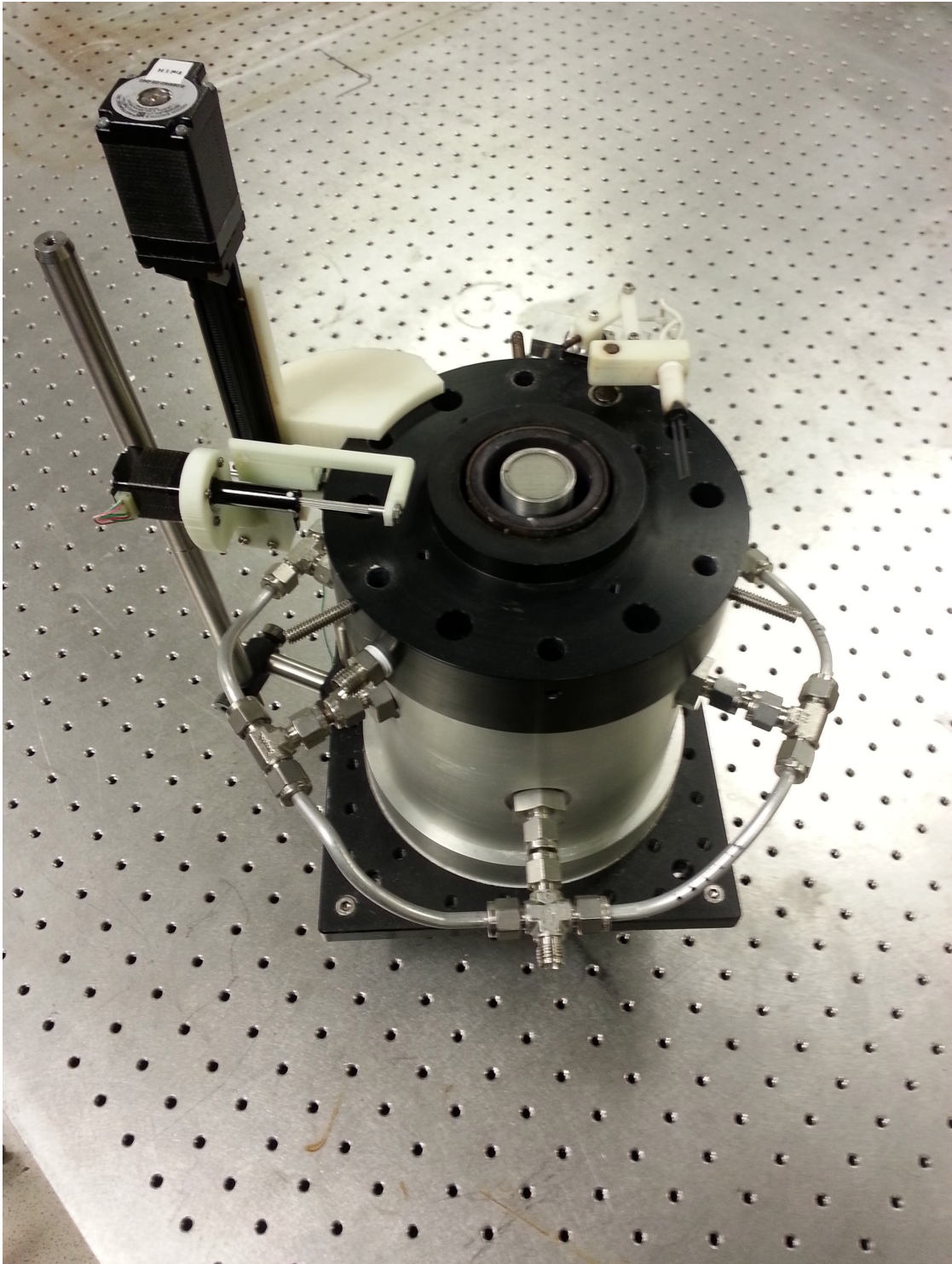
Figure B.11: Photograph of the lower part of the counterflow burner with XY-stage and igniter